CHAPTER 11: Environmental Impact of Fuel Use

This page intentionally left blank

11.1 Overview

Assessing the environmental impact of fuel use was done through a two-step process. First, regional emission scenarios were incorporated into photochemical air quality modeling simulations to estimate air quality impacts of widespread adoption of biofuels. The emission scenarios were intentionally selected to represent an aggressive implementation of biofuels: 30%, 50% and complete replacement of petroleum based gasoline and diesel fuel use by 2030. The emission characteristics of the biofuels were assumed to be well represented by data available in the literature. As will be described in the next section, these emission changes resulted in relatively small impacts on regional air quality. The extent of the impacts was put into perspective by comparing the changes to a much smaller extent of electrification of the light duty gasoline fleet of vehicles (~20% electrification of light duty gasoline vehicles).

The second part of this task used engine simulators to assess the extent to which emission characteristics of emerging biofuels might differ from current biofuels. Overall, the assessment indicates that the emission scenarios considered in the air quality modeling are reasonable, but have significant uncertainties.

11.2 Regional Air Quality Impacts of Widespread Adoption of Biofuels

11.2.1 Introduction

The analyses presented in this section assess the impacts of widespread use of biofuels as replacements for petroleum based transportation fuels. The focus in the assessments is on impacts on ozone concentrations. Ozone (O_3) is a secondary air pollutant produced by the reactions of nitrogen oxides (NO_x) and volatile organic compounds (VOCs) in the presence of sunlight at the earth's surface (Seinfeld and Pandis, 1998).

$$NO + VOCs + O_2 + Sunlight \rightarrow NO_2 + O_3$$

Ozone exposure has been associated with adverse human health effects including respiratory irritation, decreased lung function, exacerbation of asthma, and cardiovascular illness. In the United States, the primary National Ambient Air Quality Standard (NAAQS) for ozone has been established to protect human health (EPA, 2009), and the NAAQS has become increasingly stringent over time. For a region to comply with the 1997 NAAQS, the 3-year average of the fourth-highest daily maximum 8-hour average ozone concentrations measured in the region over each year must not exceed 0.08 ppm (EPA, 2009). Effective May 27, 2008, the EPA reduced the level of the NAAQS for ozone concentrations averaged over 8-hours from 0.08 ppm to 0.075 ppm. Many of the most populated counties in the United States have monitored values that exceed the level of NAAQS; based on ambient air quality data from 2004 through 2006, the number of counties in the United States with monitored violations is expected to increase from 85 under the 1997 standard to 345 under the 2008 standard (EPA, 2009).

Because of their significant contributions to NO_x and VOC emissions in urban areas, on-road mobile sources, including light and heavy-duty gasoline vehicles, light and heavy-duty diesel vehicles and motorcycles play an important role in ozone formation (Cooper and Arbrandt, 2004; Sawyer et al, 2000). For example, Niemeier et al (2005) found that the impacts of on-road traffic on ozone concentrations in remote regions were 1-5 ppb and in industrialized regions were 5-20 ppb during the summer in the Northern Hemisphere (EPA, 2006). In addition, on-road mobile emissions represent significant sources of greenhouse gas emissions. In the United States, light-duty trucks or passenger cars contribute approximately 60% of the greenhouse gas emissions from the transportation sector, and approximately 17% of the total national greenhouse gases emissions (EPA, 2009). With the significant growth in vehicle miles traveled (VMT) in many regions of the United States, emphasis has been placed on improving vehicle fuel economy, alternative fuel use, and engine and vehicle technologies as approaches for improving regional and urban air quality, as well as mitigating greenhouse gas emissions and the effects of climate change.

Analyses to be presented in this section examine the ozone impacts of widespread use of biofuels as replacements for petroleum based transportation fuels using the region around Austin, Texas as a case study. Changes in concentrations of carbon monoxide and aldehydes will also be briefly examined. To put these impacts in context, the changes in air pollutant concentrations due to widespread use of biofuels will be compared to the impacts of partial electrification of the vehicle fleet using Plug-in Hybrid Electric Vehicles (PHEVs).

The scenarios to be modeled will be based on a vision of regional population growth and urban development projected to the year 2030 in Austin. Comparisons between a 2030 base case, assuming no use of biofuels and no PHEV use, and various electrification and biofuel scenarios will be analyzed using different air quality metrics, including changes in daily maximum ozone concentrations and population exposures to ozone.

11.2.2 Methodology

11.2.2.1 Modeling Framework

The Comprehensive Air Quality Model with Extension (CAMx; www.camx.com) was used to examine the air quality impacts associated with biofuels and PHEVs. The model inputs include meteorological data, initial and boundary conditions, land use and land cover data, and emission inventories. The inventories include emissions from anthropogenic sources including stationary point sources, area sources, on-road mobile sources and non-road mobile sources, as well as emissions from biogenic sources.

Many of the inputs to the model were based on a previous study of alternative urban development patterns on future air quality (Song et al, 2008; Webb et al., 2008) in the five-county Austin-Round Rock Metropolitan Statistical (MSA). The MSA is located in Central Texas and includes the counties of Travis, Williamson, Bastrop, Hays and Caldwell as shown in Figure 11.1.

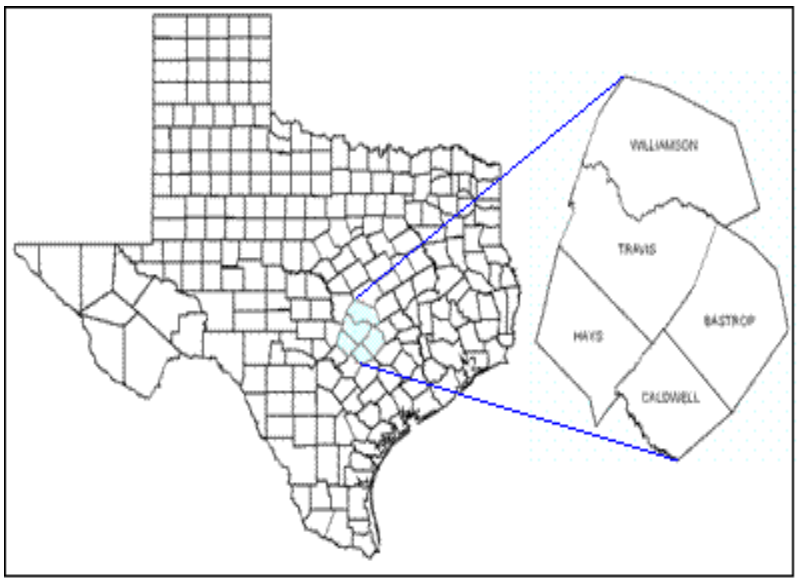

Figure 11.1. Five-county Austin-Round Rock MSA (Song et al., 2008; Webb et al., 2008).

In the work of Song et al. (2008), four urban growth scenarios, known as Envision Central Texas (ECT), were developed for the Austin area based on an assumed doubling of population in 20-40 years from 2001. For each of the 2030 ECT scenarios, changes in anthropogenic and biogenic emissions were based on future development patterns and meteorological processes. Meteorological conditions were based on a historical September 13-20, 1999 high ozone episode in the Austin area, used for the development of Austin's air quality improvement plan (an Early Action Compact, EAC, with the US EPA). In this work, partial electrification of the transportation fleet and use of biofuels was investigated over the same geographical area as in the ECT A scenario. This scenario was developed assuming extensive highway provision, and low-density and segregated-use development (Song et al., 2008). Figure 11.2 shows the urban development pattern for the ECT A scenario.

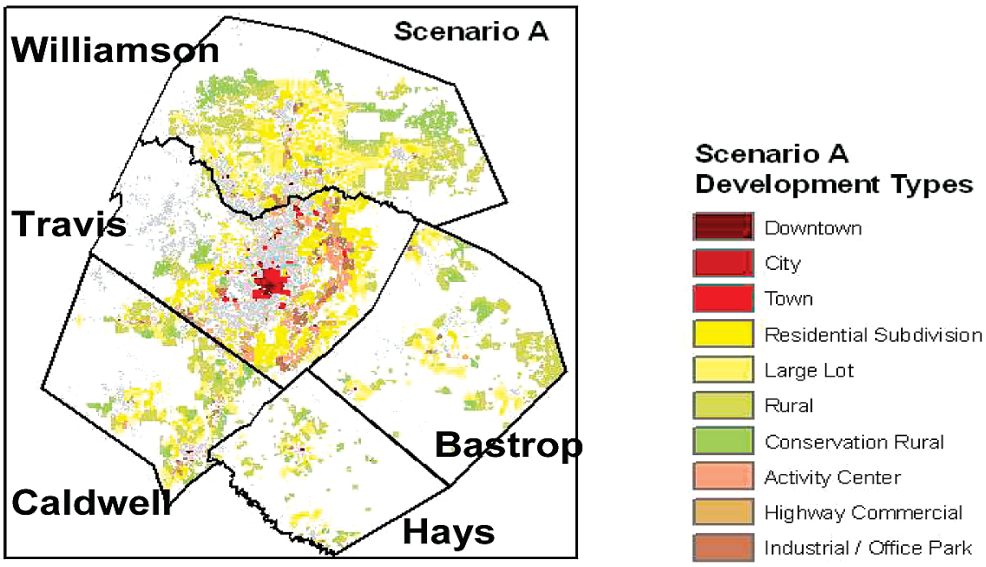

Figure 11.2. Urban development pattern for the ECT A scenario. The gray area shows the existing developed land use pattern in 2001.

The air quality modeling domain for this work is a nested regional-urban scale grid, shown in Figure 11.3. The horizontal resolution of the regional domain is 36 km, the East Texas sub-domain has a resolution of 12 km, and the Central Texas sub-domain has a resolution of 4 km. All anthropogenic and biogenic emissions used in this work were the same as those used by Song et al. (2008) for the ECT A scenario with the exception of the emissions for point sources and mobile sources, which were replaced by modified inventories for the PHEVs, E85 and B100 scenarios as described below.

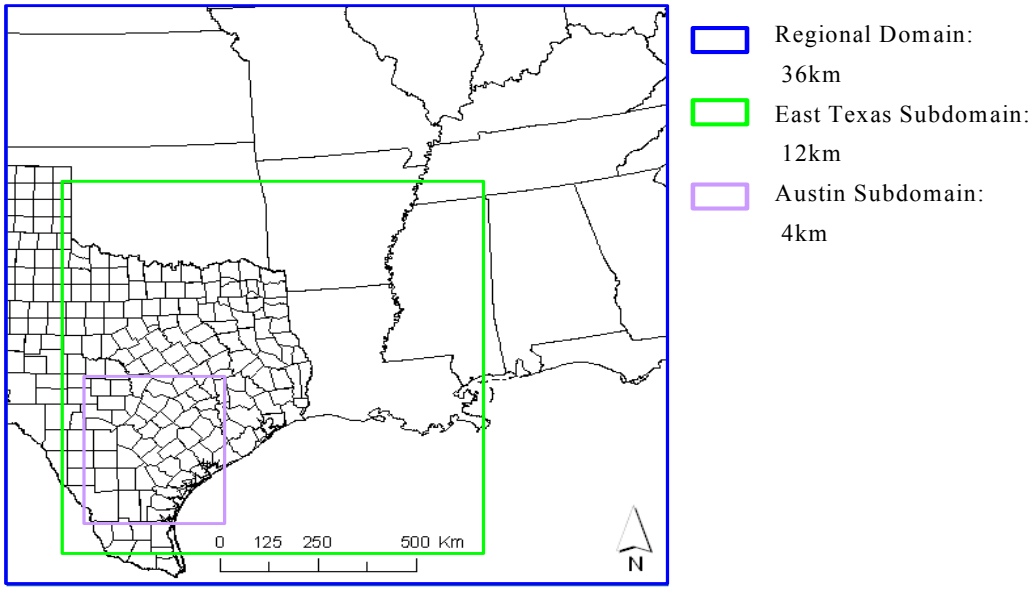

Figure 11.3: Nested 36-km/12-km/4-km photochemical modeling domain (Song et al., 2008).

A summary of emissions from point sources, on-road and non-road mobile sources, area sources, and biogenic sources for the ECT A scenario from the work of Song et al. (2008) is presented in Table 11.1 and compared to an estimate of 2007 emissions for the same region. As described by Song et al. (2008), federal motor vehicles control programs, such as the Tier 2 heavy-duty rules, will be fully implemented by 2030, which accounts for the reduction in on-road mobile emissions for ECT A compared to the 2007 base case.

Table 11.1: VOC and NOx emissions (tons per day) for the 2007 base case and the ECT A scenario (Song et al., 2008; Webb et al., 2008).

Categories	2007 estimated emissions		ECT A	
	VOC	NOx	VOC	NOx
On-road mobile	33.8	62.1	22.0	18.4
Non-road mobile	22.2	21.7	23.2	9.5
Area	110.7	10.2	214.3	20.6
Point	3	2.8	3.0	2.8
Biogenic	211.2	20.2	198.8	20.2

11.2.2.2 Emission inventories

Plug-in Hybrid Electric Vehicles (PHEVs) The electrification of the transportation fleet involves increases in electricity demand, and a variety of assumptions therefore need to be made about electrical energy generation, and the emissions associated with that generation in the Austin area.

The Austin area uses several types of fuels for electricity generation, including coal, natural gas, nuclear, purchased power, and renewable sources such as biomass, wind and solar (Austin Energy, 2008a). The maximum generation capacity in the area is more than 5,300 MW, with approximately 3,140 MW of capacity from natural gas and 1 MW from solar. Approximately 274 MW of wind generation is currently available to the City of Austin as purchased power. Furthermore, there is approximately an additional 265 MW of capacity scheduled for installation at the end of 2009, including 165 MW from wind. Thus, at the end of 2009, the total maximum generation capacity available will be more than 5500 MW in the Austin area. Austin area power plants that use natural gas and coal as fuels are shown in Table 11.2 with their capacities.

Table 11.2: Power plants capacity based on fuel type in Austin area (Austin Energy, 2008b).

Facility Name	Number of Units	Fuel Type	Capacity (MW)
Decker Creek	2	Gas	934
Sand Hill Energy Center	5	Gas	501
Sam Seymour (Fayette Power Project)	3	Coal	1641
Sim Gideon	3	Gas	620
Lost Pines	2	Gas	545
Bastrop Energy Center	2	Gas	540
Sandow	1	Coal	600

Power plants tend to use the lowest cost resources, frequently coal or nuclear energy, to produce the base load electricity needed (Austin Energy, 2008b). The electricity available from Austin area power plants varies during the daytime hours with a maximum peak load of more than 1800 MW for a typical summer day (at 3:00 PM) as shown in Figure 11.4. The hourly electricity generation profile was calculated based on hourly emissions data from the Clean Air Markets Division of the U.S. EPA for the 2008 ozone season (May - September), and the electricity generation available from each power plant in the area (EPA, 2008).

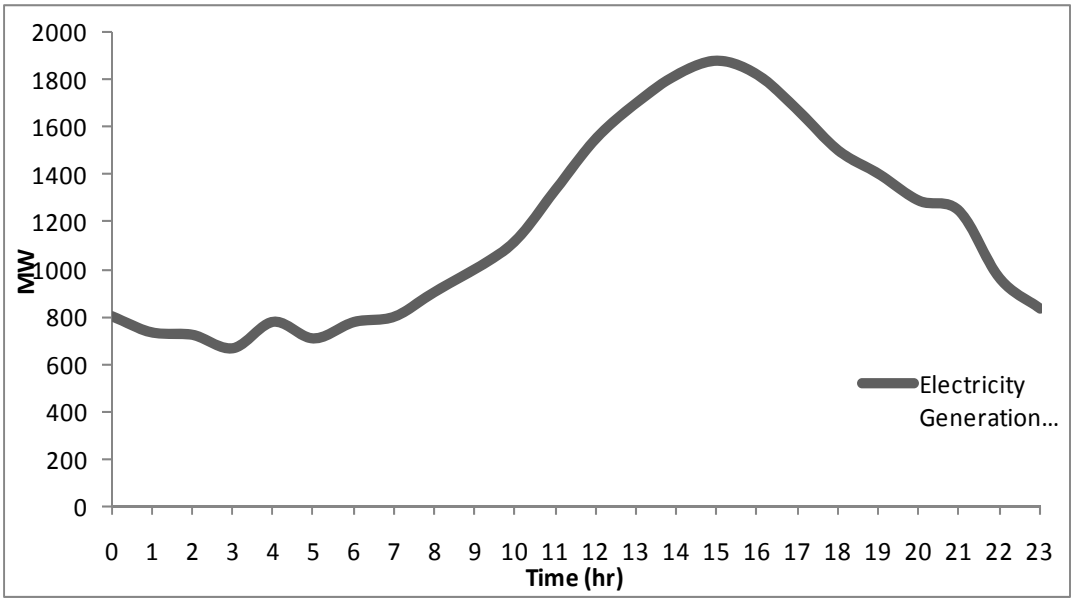

Figure 11.2: Hourly electricity consumption for the Austin area based on 2008 ozone season data (EPA, 2008).

In this work it is assumed that PHEVs use the excess capacity from electricity generation units during nighttime hours for charging, after vehicle use during the daytime. Charging of PHEVs during nighttime hours is assumed to occur between 10 PM and 10 AM. The electricity demand at this time is significantly lower than at times of peak demand and could be met without addition of generation units. Three different scenarios for charging PHEVs were considered in this work:

i. Scenario 1: Use the same electricity generation capacity, but with a different temporal profile by charging PHEVs during nighttime hours and applying a more stringent level of emissions control on EGUs during daytime hours. This would result in a flat temporal profile of emissions.

ii. Scenario 2: Same as Scenario 1, but without applying any additional controls on the emissions from electricity generation units.

iii. Scenario 3: Same as Scenario 2, plus shifting 50% of the remaining vehicles from gasoline to E85 fuel.

The method used to calculate the emissions reductions associated with the use of PHEVs is based on the average fuel economy factors or the electricity consumption for each type of vehicle. The average economy factors from the Electric Power Research Institute (EPRI) (Knipping and Duvall, 2007a, Knipping and Duvall, 2007b) were used to determine the changes in on-road mobile source emissions. The additional MW-h available during the nighttime hours was converted to total vehicle miles traveled (VMT) by distributing the VMT to three types of

light duty vehicles based on the percentage of these vehicles in the fleet, as shown in Table 11.3. The average economy factors from EPRI (Knipping and Duvall, 2007a) are greater than the estimate of 300 Wh/mile from the Pacific Northwest National Laboratory (PNL) (Kintner-Meyer, Schneider, and Pratt, 2007). Thus, the EPRI factors represented a more conservative assessment of the benefits of PHEVs and were selected for this work. Table 11.3 shows the distribution of light duty gasoline vehicles and the average economy factors from EPRI.

Table 11.3. Light duty gasoline vehicle types and associated fuel economy factors (Knipping and Duvall, 2007a).

Vehicle Type	Light duty passenger fleet (%)	Average Fuel Economy Factor (Wh/mile)	VMT (10^6)
Passenger cars	65%	318.2	10.3
Gas truck (SUV)	13.50%	394.2	1.7
Gas truck	21.50%	493.2	2.2

As shown in Table 11.3, three types of light-duty gasoline passenger vehicles were considered in the analysis: passenger cars, sport utilities vehicles (SUVs) and light-duty gasoline trucks. Federal highway statistics for 2002 (DOT, 2002) provided the percentage of vehicles in each category. Passenger cars accounted for 65% of the total light duty gasoline vehicles in service, SUV trucks accounted for 13.5%, and gasoline trucks represented 21.5%. Changes in total NOx and VOC emission rates between the ECT A scenario described by Song et al. (2008) and the three PHEV scenarios are described in more detail below.

PHEV Scenario 1 Scenario 1 was based on using the same electricity generation emissions that Austin currently has, but with a different temporal profile. It was assumed that the use of PHEVs would level the profile during the day (constant emissions), but due to emission caps, the overall amount of emissions would remain constant. This scenario is realistic if night-time charging flattens the overall generation profile by raising the nocturnal dip in generation to more closely match the daytime usage. An additional assumption associated with this scenario is that an annual or seasonal emissions cap leads to emissions that remain at today's levels, even through total generation is increased. Figure 11.5 shows the temporal profiles for electricity generation currently used in Austin (for all Austin power plants) (EPA, 2008) and for the emission rates used in PHEV Scenario 1.

In this scenario, the additional electricity that would be available during the nighttime hours for PHEV charging was 5040 MW-h. Using the average fuel economy factors and the percentage of each category of light-duty vehicles described above, the total VMT for PHEVs in the five-county Austin MSA was determined to be 14.2 million miles traveled per day as shown in Table 11.3. The VMT was distributed between the three types of vehicle based on the fleet

composition, i.e., the VMT for passenger cars, SUVs and light-duty trucks was 10.3 million, 1.7 million, and 2.2 million, respectively. The total VMT for light-duty gasoline vehicles in ECT A from Song et al. (2008) is 82.4 million. Thus, the reduction in the VMT for light-duty gasoline vehicles due to their replacement with PHEVs in Scenario 1 is 17%. This assumes several hundred thousand PHEVs in use, if each vehicle travels 50 miles each day.

The percentage reduction in light-duty gasoline vehicle VMT and the new temporal profiles for the electricity generation units were applied to the on-road mobile source and point source emissions inventories, respectively, used by Song et al. (2008). Table 11.4 shows the emissions of VOC and NOx (ton per day) for ECT A (Song et al., 2008) and PHEVs scenarios.

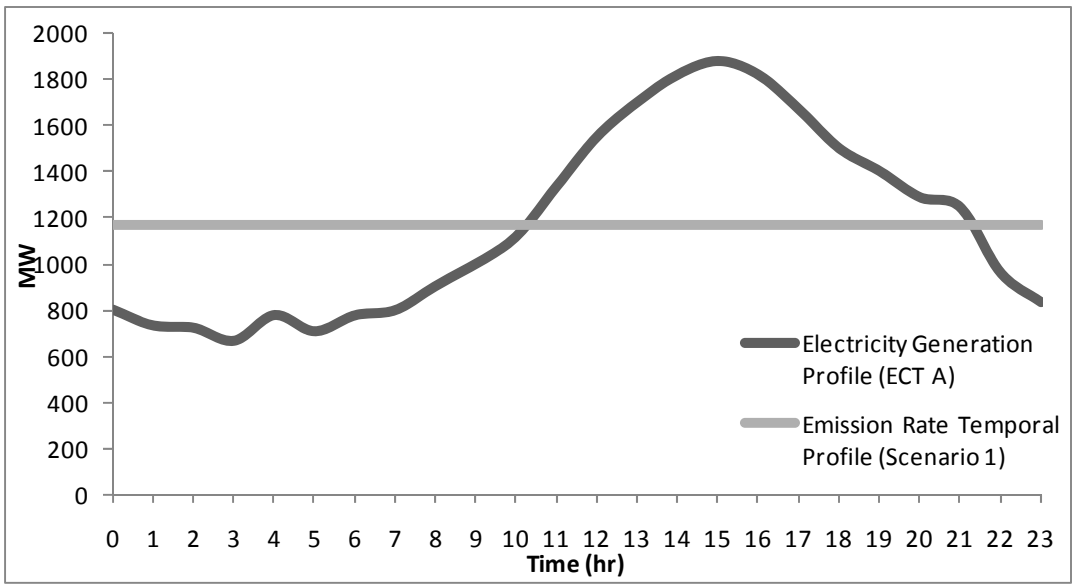

Figure 11.3: Electricity generation temporal profile (EPA, 2008) currently used in Austin and emission rate temporal profile used in PHEV Scenario 1 (for all Austin power plants).

Table 11.4: Emissions of VOC and NOx (ton per day) for ECT A (Song et al., 2008) and the PHEVs scenarios.

Categories	ECT A		Scenario 1		Scenario 2		Scenario 3	
	VOC	NOx	VOC	NOx	VOC	NOx	VOC	NOx
On-road mobile	22.0	18.4	18.3	15.3	18.3	15.3	20.0	13.0
Non-road mobile	23.2	9.5	23.2	9.5	23.2	9.5	23.2	9.5
Area	214.3	20.6	214.3	20.6	214.3	20.6	214.3	20.6
Point	3	2.8	3	2.8	3.3	3.03	3.3	3.03
Biogenic	198.8	20.2	198.8	20.2	198.8	20.2	198.8	20.2

PHEV Scenario 2 Unlike Scenario 1, Scenario 2 assumed no additional controls will be applied on electricity generation units to reduce their emission rates during daytime hours. Thus, emission rates will increase during the nighttime hours as a result of the increasing demand due to charging of the PHEVs. However, emissions rates during daytime hours will be the same as ECT A, with maximum demand during the afternoon. Figure 11.6 shows both the original electricity generation temporal profile and Scenario 2 electricity generation temporal profile.

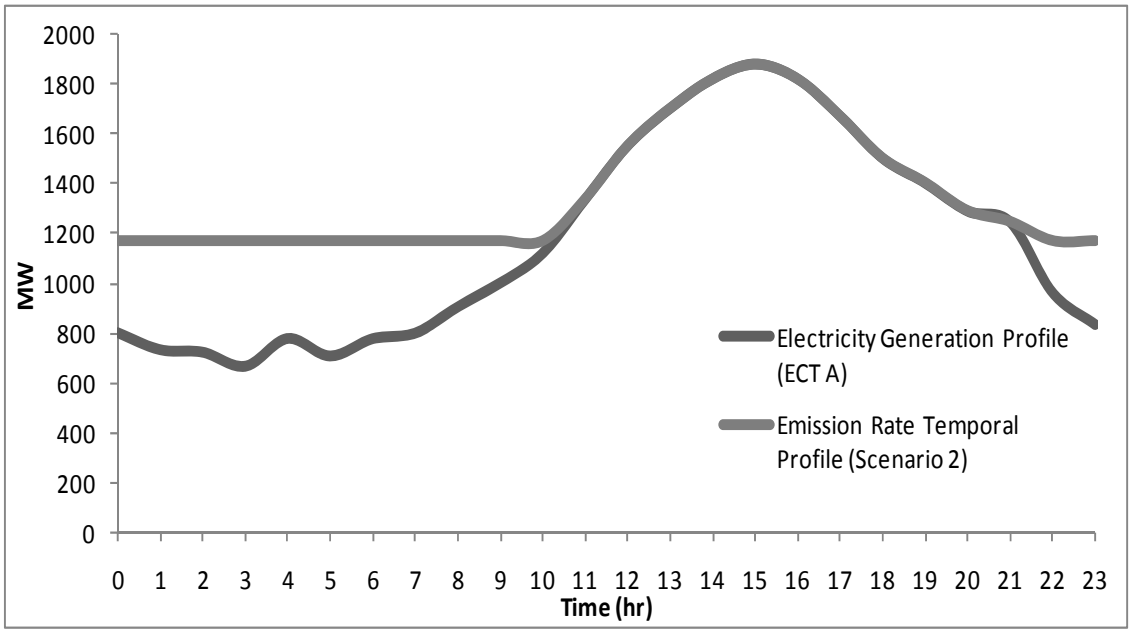

Figure 11.4: Original electricity generation profile and emission rates temporal profile in Scenario 2.

In Scenario 2, the reduction associated with the use of PHEVs in the vehicle fleet is the same as the reduction in Scenario 1. Point source emissions were modified such that the emission rates remained constant during daytime hours, but increased during the nighttime hours due to the charging of PHEVs. The changes in VOC and NOx emissions for Scenario 2 compared to ECT A and Scenario 1 are shown in Table 11.4. VOC and NOx emissions for Scenario 2 from the vehicle fleet are the same as Scenario 1. However, in Scenario 2, VOC and NOx emissions from point sources would increase relative to Scenario 1.

PHEV Scenario 3 Scenario 3 considered a combined strategy of PHEVs and biofuels by assuming that 17% of the vehicle fleet is replaced by PHEVs, as in Scenarios 1 and 2, and that half of the remaining light-duty gasoline fleet switches from petroleum-based fuel to E85. Thus, 41.5 % of the vehicle fleet uses E85 in Scenario 3. Changes in the emissions of CO, NO_x, and VOCs were based on the work of Jacobson (2007) and are described in detail in the biofuels section below. Point source emissions were modified during the nighttime hours in response to the additional electricity demand for charging PHEVs. The temporal profile for power plants emissions in Scenario 3 is the same as that of Scenario 2.

Biofuel Scenarios: Ethanol (E85) The Energy Independence and Security Act of 2007 (DOE, 2007) called for an increase in the production and use of renewable fuels. The increase in the use of alternative or renewable fuels at high levels of biofuel use is expected to be met in large part with ethanol. E85 is a blend of 85 percent denatured fuel ethanol and 15% gasoline, and can be used in flex-fuel vehicles (FFVs) (Lavigne and Powers, 2007). In this work, three different scenarios were considered in which E85 is used as a replacement for petroleum-based fuel for light-duty gasoline vehicles:

i. Scenario 1: 30% fleet use of E85.
ii. Scenario 2: 50% fleet use of E85.
iii. Scenario 3: 100% fleet use of E85.

Unlike the PHEVs scenarios, point source emissions from power plants were not altered for the E85 scenarios relative to the ECT A scenario of Song et al. (2008). Only emissions for on-road mobile sources were modified for the E85 scenarios based on the work of Jacobson (2007).

In Scenarios 1, 2, and 3, on-road mobile source emissions were modified to account for the replacement of 30%, 50%, and 100%, respectively, of the gasoline fleet with E85. NOx emissions for these vehicles decreased by 30 %, while CO and VOC emissions increased by 5% and 19.6% respectively (Jacobson, 2007). The VOC speciation profile was also adjusted in addition to the emission factors. The emissions were speciated into Carbon Bond IV (CB-IV) categories for modeling atmospheric chemistry, based on the work of Carter (2009). The gasoline exhaust and running losses VOC speciation profile was based on the exhaust composition (tailpipe exhaust emissions) in the Washburn Tunnel in Houston, Texas (McGaughey et al, 2004). Table 11.5 shows the VOC speciation profiles for gasoline (McGaughey et al, 2004), E85 (Webb et. al., 2008), diesel and B100 exhaust for the CB-IV mechanism used in CAMx.

Table 11.5: VOC speciation profiles for E85 (Webb et al., 2008), gasoline (McGaughey et al, 2004), diesel and B100 for the CB-IV mechanism used in CAMx.

Fuel	OLE %	PAR %	TOL %	XYL %	FORM %	ALD2 %	ETH %	MEOH %	ETOH %	ISOP %	NR %
Gasoline	3.23	53.2	7.92	10.6	1.9	4.0	6.11	0.22	0.23	0.34	14.93
E85	1.34	8.3	1.3	1.75	2.3	8.13	3.6	0.181	64	0.055	9.2
Diesel	2.49	47.8	6.27	34.6	1.81	2.38	4.22	0	0	0	13.84
B100	9.7	16.39	10.2	0	12.1	14.0	23.5	0	0	0.465	5.9

.

Biodiesel (B100) Biodiesel consists of long-chain methyl esters or ethyl esters of fatty acids. Biodiesel-fueled vehicles are assumed to emit more NOx, but less CO and VOCs (Sheehan, 1998; EPA, 2002; Lindhjem and Pollack, 2003; McCormick et al, 2006) than petroleum based diesel. Emissions factors used in this analysis were based on a Southwest Research Institute (SwRI) study by Sharp (1999) that investigated exhaust emissions from a diesel truck engine while fueled on biodiesel and diesel fuel. It is recognized that this is a limitation in this work as the chemical composition of biodiesel in 1999 may differ from either current or future biodiesels. This issue will be addressed later in this chapter.

Three scenarios were used to assess the air quality impacts of increased penetration B100 in the Austin fleet as an alternative to petroleum-based diesel:

i. Scenario 1: 30% of the heavy-duty fleet is converted to B100.
ii. Scenario 2: 50% of the heavy-duty fleet is converted to B100.
iii. Scenario 3: 100% of the heavy-duty fleet is converted to B100.

Only emissions from on-road mobile sources were modified in the B100 scenarios; emission inventories from all other anthropogenic sources remained the same as for the ECT A scenario of Song et al. (2008). Vehicles fueled by B100 were assumed to emit 13% more NOx, 45% less CO and 49% less VOC than conventional petroleum-based diesel according to the findings of Sharp (1999). As for the case with E85, the photochemical modeling runs were performed for 30%, 50%, and 100% replacement of traditional diesel petroleum-based fuel with B100. A modified CB-IV profile, shown in Table 11.5, was used for the chemical speciation of VOC emissions from B100. This profile was based on B100 exhaust VOC emissions from Sharp (1999) that were speciated into CB-IV structures based on the work of Carter (2009). Most VOC emisisons from B100 are represented by the following CB-IV species: ethene (23.5%), higher aldehyde (14%) and formaldehyde (12.1%). Table 11.6 shows the percentage change in emisisons of NOx, VOC and CO for both E85 and B100, based on the work of Jacobson (2007) and Sharp (1999).

Table 11.6: Changes in emissions of NOx, VOC and CO associated with E85 and B100 (Jacobson, 2007; Sharp, 1999). Decreases in emissions relative to conventional petroleum fuel are denoted by a negative value.

Fuel	NOx	VOC	CO
E85	-30%	19.60%	5%
B100	13%	-49%	-45%

Combined biodiesel and ethanol scenario This scenario assumes that a combination of biofuels (both E85 and B100) is used in all vehicles (100% fleet penetration). E85 replaces petroleum-gasoline fuel, and B100 replaces petroleum-diesel fuel. As with the other biofuels scenarios, only the emissions inventories for on-road mobile sources were modified; other anthropogenic inventories remained the same in this scenario as for the ECT A scenario of Song et al. (2008).

Summary of scenarios Summaries of VOC and NOx emissions for the ECT A and E85 scenarios, B100 scenarios and combined biofuels scenario are shown in Tables 11.7, 11.8 and 11.9, respectively.

Table 11.7: Emissions of VOC and NOx (ton per day) for ECT A (Song et al., 2008) and E85 scenarios.

Categories	**ECT A**		**Scenario 1**		**Scenario 2**		**Scenario 3**	
	VOC	**NOx**	**VOC**	**NOx**	**VOC**	**NOx**	**VOC**	**NOx**
On-road mobile	22.0	18.4	23.22	16.86	24.01	15.84	26.06	13.27
Non-road mobile	23.2	9.5	23.2	9.5	23.2	9.5	23.2	9.5
Area	214.3	20.6	214.3	20.6	214.3	20.6	214.3	20.6
Point	3	2.8	3	2.8	3	2.8	3	2.8
Biogenic	198.8	20.2	198.8	20.2	198.8	20.2	198.8	20.2

Table 11.8: Emissions of VOC and NOx (ton per day) for ECT A (Song et al., 2008) and B100 scenarios.

Categories	**ECT A**		**Scenario 1**		**Scenario 2**		**Scenario 3**	
	VOC	**NOx**	**VOC**	**NOx**	**VOC**	**NOx**	**VOC**	**NOx**
On-road mobile	22.0	18.4	21.81	18.45	21.68	18.48	21.36	18.57
Non-road mobile	23.2	9.5	23.2	9.5	23.2	9.5	23.2	9.5
Area	214.3	20.6	214.3	20.6	214.3	20.6	214.3	20.6
Point	3	2.8	3	2.8	3	2.8	3	2.8
Biogenic	198.8	20.2	198.8	20.2	198.8	20.2	198.8	20.2

Table 11.9. Emissions of VOC and NOx (ton per day) for the ECT A (Song et al., 2008) and biofuels combination scenarios.

Categories	ECT A		Biofuels Combination	
	VOC	NOx	VOC	NOx
On-road mobile	22.0	18.4	25.42	13.44
Non-road mobile	23.2	9.5	23.2	9.5
Area	214.3	20.6	214.3	20.6
Point	3	2.8	3	2.8
Biogenic	198.8	20.2	198.8	20.2

11.2.2.3 Air Quality Metrics

Four metrics were used to evaluate and compare the impacts of the PHEV and biofuels scenarios in the Austin area:

i. Maximum 1-hour average (and 8-hour average) ozone concentration.
ii. Total area above a threshold ozone concentration.
iii. Time integrated area above a threshold ozone concentration.
iv. Total daily population exposure.

Two threshold ozone concentrations of 60 ppb and 70 ppb were used in the analyses for the area of exceedance metrics. For the fourth metric, total daily population exposure, a 0 ppb threshold was used in order to provide a more comprehensive assessment of the impacts of these scenarios relative to the ECT A scenario of Song et al. (2008). The metrics are described below;

1. Maximum 1-hour ozone concentration:

$$M_{max.\ 1\text{-}hr} = \text{Max}\ \{C_{g,h}\}$$

where, $C_{g,h}$ is the 1-hour O_3 concentration in (ppb), in the grid cell (g) and at time (h). This metric was calculated by examining all ground level 1-hour ozone concentration in Austin area during each day, and choosing the maximum 1-hour averaged ozone concentration.

2. Total area above a threshold ozone concentration of 60 ppb or 70 ppb:

$$M_{Area\ tot.} = \sum_{g} A_{g} \max\{\delta_{g,h}\}$$

$$\delta_{g,h} = \begin{cases} 0, C \leq 60 \text{ (or 70)}, \\ 1, C > 60 \text{ (or 70)} \end{cases}$$

$$\delta_{g,h} = \{ \delta_{g,1}, \delta_{g,2}, \delta_{g,3} \ldots\ldots \delta_{g,24} \}$$

where A is the area of the grid cell g in (km^2). This metric was calculated by determining whether the ground level 1-hour ozone concentration exceeded a threshold concentration of 60 ppb (or 70 ppb). If ozone concentration exceeds the threshold at any time during the day in Austin area, the area is calculated and then summed over all cells.

Time integrated area above a threshold ozone concentration of 60 ppb or 70 ppb:

$$M_{\text{Time Area}} = \sum_h \sum_g A_g * \delta_{g,h}$$

$$\delta_{g,h} = \begin{cases} 0, C \leq 60 \text{ (or 70)}, \\ 1, C > 60 \text{ (or 70)} \end{cases}$$

The maximum 1-hour ozone concentration in all ground level grid cells in the Austin area was determined for each hour of each day, and compared with the threshold of 60 ppb or 70 ppb. If there was an exceedance in any grid cell, then the area of this grid cell was summed over the day.

Total daily population exposure:

$$M_{\text{Time Pop.}} = \sum_h \sum_g P_g * \delta_{g,h}$$

$$\delta_{g,h} = \begin{cases} 0, C \leq 60 \text{ (or 70)}, \\ C - 60, C > 60 \text{ (or 70)} \end{cases}$$

where P_g is the population in grid cell g. This metric was calculated by multiplying the population density by the difference between the maximum ozone concentration and the threshold ozone concentration of 60 ppb or 70 ppb, if the ozone concentration at the grid cell exceeded the threshold. The value was calculated for each grid cell in the five county areas and summed over the day. A threshold ozone concentration of 0 ppb was also considered in this work in order to gain a more comprehensive understanding of the ozone exposure level in the area of interest.

11.2.3 Results

11.2.3.1 Maximum 1-hour (and 8-hour) O_3 Concentrations

The predicted daily maximum 1-hour ozone concentrations for the future year 2030 were estimated for the ECT A and the various biofuel and PHEV scenarios (PHEVs, E85, B100 and the combination biofuels). This maximum 1-hour averaged ozone concentration is conducted for four types of days based on driving behavior. These days are: Weekdays (based on the meteorology and emissions of Sept.15th, 16th and 20th during the modeling episode), Friday (based on the meteorology and emissions of Sept.17th during the modeling episode), Saturday (based on the meteorology and emissions of Sept.18th during the modeling episode), and Sunday (based on the meteorology and emissions of Sept.19th during the modeling episode). For the ECT A case, the daily maximum 1-hour ozone concentration ranges from 84.65 ppb to 70.2 ppb. Table 11.10 lists the daily maximum 1-hour ozone concentration for the ECT A and PHEV scenarios. These values are the maximum ozone concentration during the day, regardless of time or location.

Table 11.10: Daily maximum 1-hour O_3 concentration for ECT A and PHEVs scenarios

		PHEVs Maximum 1-hr O_3 (ppb)		
Date	ECT A	Scenario 1	Scenario 2	Scenario 3
Sept. 15	75.85	74.35	75.53	75.29
Sept. 16	70.20	70.15	70.15	70.07
Sept. 17	78.95	78.96	78.96	78.96
Sept. 18	82.08	82.06	82.06	82.06
Sept. 19	84.65	83.78	83.78	83.77
Sept. 20	80.80	78.67	80.14	79.76

Table 11.11 shows the maximum 8-hour averaged ozone concentrations for both the ECT A and PHEVs scenarios. These values represent the maximum 8-hr ozone concentrations in the entire ground level grid cells in Austin area regardless the time of the day.

Table 11.11: Daily maximum 8-hr O_3 concentration for ECT A and PHEVs scenarios

		PHEVs Maximum 8-hr O_3 (ppb)		
Date	ECT A	Scenario 1	Scenario 2	Scenario 3
Sept. 15	68.004	67.37	67.89	67.72
Sept. 16	67.13	66.93	66.93	66.76
Sept. 17	73.36	73.15	73.15	73.02
Sept. 18	70.83	70.23	70.94	70.53
Sept. 19	74.66	73.56	74.18	73.82
Sept. 20	75.79	74.44	75.33	74.95

Tables 11.12 and 11.13 list the daily maximum 1-hour and 8-hour ozone concentrations for both the ECT A and the E85 scenarios. E85 Scenario 1 represents 30% replacement of traditional petroleum fuel with E85, Scenario 2 accounts for 50% replacement and 100% of on-road vehicles in Scenario 3 have E85.

Table 11.12: Daily maximum 1-hour O_3 concentration for both ECT A and E85 scenarios

		E85 1 Maximum 1-hr O_3 (ppb)		
Date	ECT A	Scenario 1	Scenario 2	Scenario 3
Sept. 15	75.85	75.68	75.57	75.28
Sept. 16	70.20	70.15	70.11	70.02
Sept. 17	78.95	78.95	78.95	78.95
Sept. 18	82.08	82.08	82.08	82.08
Sept. 19	84.65	84.21	83.91	83.58
Sept. 20	80.80	80.41	80.14	79.46

Table 11.13: Daily maximum 8-hour O_3 concentration for both ECT A and E85 scenarios

		E85 Maximum 8-hr O_3 (ppb)		
Date	ECT A	Scenario 1	Scenario 2	Scenario 3
Sept. 15	68.004	67.88	67.80	67.58
Sept. 16	67.13	67.01	66.93	66.73
Sept. 17	73.36	73.27	73.21	73.05
Sept. 18	70.83	70.51	70.30	69.76
Sept. 19	74.66	74.40	74.23	73.79
Sept. 20	75.79	75.48	75.27	74.79

Maximum 1-hour ozone concentrations in addition to the maximum 8-hour ozone concentrations for both the ECT A and the B100 scenarios are listed in Tables 11.14 and 11.15. These scenarios include 30% penetration in vehicles fleet (Scenario 1), 50% in Scenario 2 and 100% in Scenario 3.

Table 11.14: Daily maximum 1-hour O_3 concentration for both ECT A and B100 scenarios

		B100 Maximum 1-hr O_3 (ppb)		
Date	ECT A	Scenario 1	Scenario 2	Scenario 3
Sept. 15	75.85	75.85	75.86	75.86
Sept. 16	70.20	70.20	70.20	70.20
Sept. 17	78.95	78.95	78.95	78.95
Sept. 18	82.08	82.08	82.08	82.08
Sept. 19	84.65	84.66	84.66	84.67
Sept. 20	80.80	80.82	80.83	80.86

Table 11.15: Daily maximum 8-hour O_3 concentration for both ECT A and B100 scenarios

		B100 Maximum 8-hr O_3 (ppb)		
Date	ECT A	Scenario 1	Scenario 2	Scenario 3
Sept. 15	68.004	68.01	68.01	68.02
Sept. 16	67.13	67.13	67.14	67.14
Sept. 17	73.36	73.36	73.36	73.36
Sept. 18	70.83	70.83	70.84	70.85
Sept. 19	74.66	74.66	74.66	74.67
Sept. 20	75.79	75.80	75.81	75.83

In the combined biofuels case, both diesel and gasoline were assumed to be replaced with biofuels (both E85 and B100). The penetration percentage in the on-road vehicle fleet is assumed to be 100%. Tables 11.16 and 11.17 list the maximum 1-hour and 8-hour average ozone concentrations for the ECT A and the test case, which accounts for replacement of 100% of gasoline with E85 and 100% of diesel with B100.

Table 11.16: Daily maximum 1-hour O_3 concentration (E85 + B100)

Date	ECT A (ppb)	(E85+B100) Maximum 1-hr O_3 (ppb)
Sept. 15	75.85	75.30
Sept. 16	70.20	70.03
Sept. 17	78.95	78.95
Sept. 18	82.08	82.08
Sept. 19	84.65	83.58
Sept. 20	80.80	79.52

Table 11.17: Daily maximum 8-hour O_3 concentration (E85 + B100)

Date	ECT A (ppb)	(E85+B100) Maximum 8-hr O_3 (ppb)
Sept. 15	68.004	67.60
Sept. 16	67.13	66.74
Sept. 17	73.36	73.06
Sept. 18	70.83	69.77
Sept. 19	74.66	73.80
Sept. 20	75.79	74.83

The Tables simply list changes in maximum ozone concentrations, however, the scenarios produce complex spatial distributions of concentration changes. Figure 11.5 shows the maximum reduction and increase ($O_{3\ testcase} - O_{3\ basecase}$) in hourly O_3 concentrations for PHEVs Scenario 1, third E85 Scenario 3 and the combined biofuels case. The Figure is created by finding the maximum difference in ozone concentration for the day, in each grid cell. These values for each grid cell are combined into a single Figure, even if the maximum differences occur at different times of day in different grid cells. So, these values are the maximum difference in ozone concentration on Sept. 20th , regardless of time of day, in the Austin area.

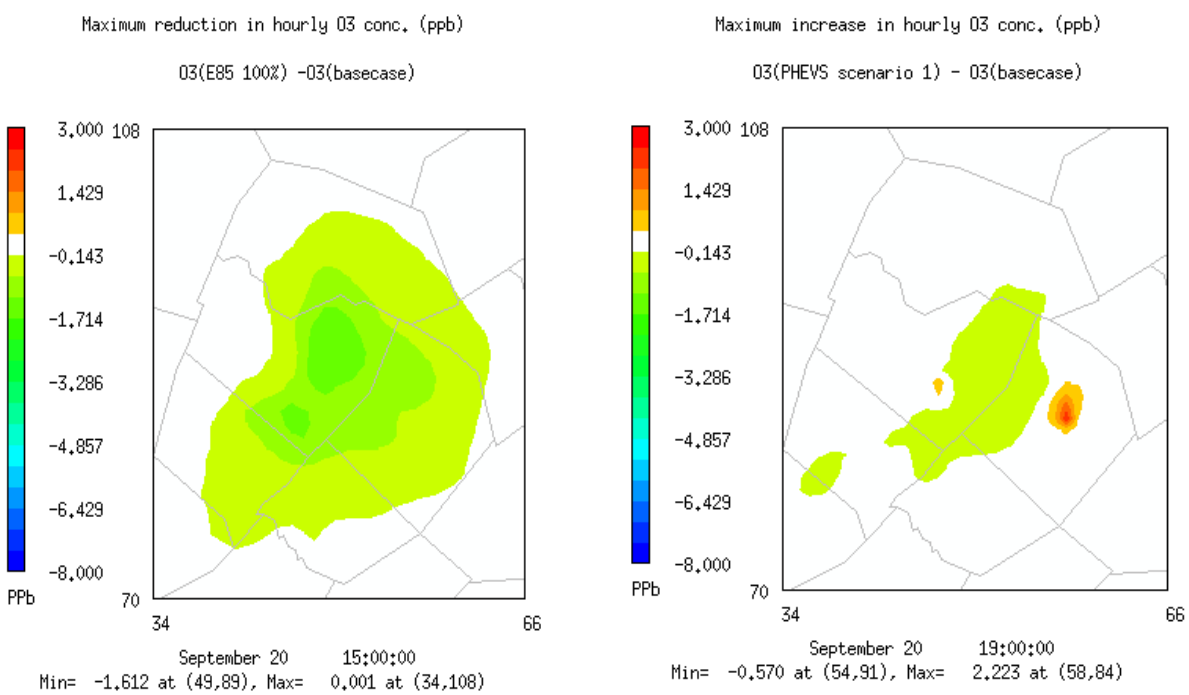

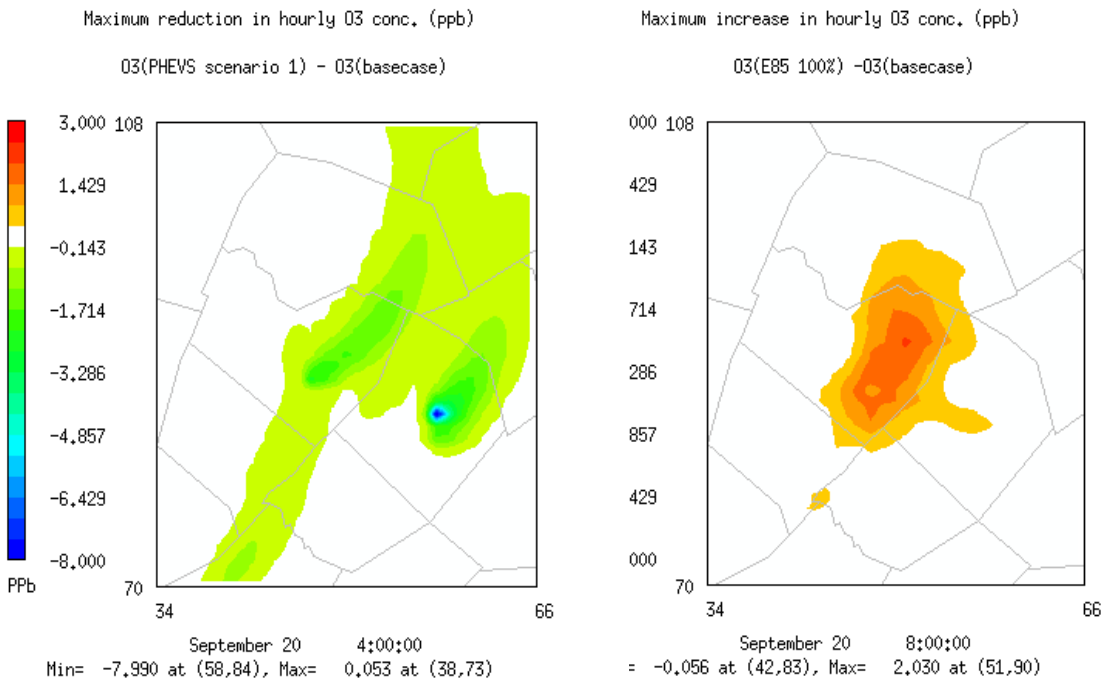

Figure 11.5: Maximum changes (reductions and increases) for PHEVs, E85 and the combination case relative to the ECT A.

11.2.3.2 Area above a threshold 1-hour average O_3 Concentration

The metric for the total area above a threshold ozone concentration is the summation of the areas of all grid cells in the model that have ground level ozone concentrations more than the threshold of 60 ppb (or 70 ppb). Thus, if the 1-hour ozone concentration exceeds the threshold at any time during the day in Austin area, the area is included and the summation is done over all the cells. Table 11.18 lists the reduction (as %) in total area exceeding a threshold of 60 ppb for the PHEVs scenarios relative to the ECT A case. The maximum reduction is 3.9%, and is achieved when applying scenario 1. However, there is an increase in total area above a threshold of 60 ppb in both scenarios 2 and 3, and this increase happens on the same day.

Table 11.18: Reduction in total area exceeding threshold of 60 ppb, PHEVs scenarios

	PHEVs 60 ppb		
Date	Scenario 1	Scenario 2	Scenario 3
Sept. 15	3.90	0.37	0.74
Sept. 16	0.72	-0.48	-0.24
Sept. 17	0	0	0
Sept. 18	0.13	0	0.13
Sept. 19	0	0	0
Sept. 20	0.77	0.77	1.35

The reduction in total area above a threshold of 70 ppb is shown in Table 11.19. The percentage reduction in total area exceeding a threshold of 70 ppb is more than the reduction when the threshold equal 60 ppb, with maximum of 66.67% in Scenario 3. There is also an increase (-0.37%), in total area above a threshold of 70 ppb in Scenario 2.

Table 11.19: Reduction in total area exceeding threshold of 70 ppb, PHEVs scenarios

	PHEVs 70 ppb		
Date	Scenario 1	Scenario 2	Scenario 3
Sept. 15	12.61	7.21	10.81
Sept. 16	33.33	33.33	66.67
Sept. 17	3.96	1.85	3.17
Sept. 18	7.58	2.84	5.21
Sept. 19	0.92	-0.37	0.18
Sept. 20	3.79	1.42	5.21

Tables 11.20 and 11.21 present the reduction (as %) in total area exceeding a threshold of 60 and 70 ppb for E85 scenarios compared to ECT A. The maximum reduction in the total area at the first threshold is 1.16% in Scenario 3, while the minimum reduction is 0 on the first day of the ozone episode days in scenario 1. For a threshold of 70 ppb, the maximum reduction in the E85 scenarios is 66.67%, and achieved in scenario 3.

Table 11.20: Reduction in total area exceeding threshold of 60 ppb, E85 scenarios

	E85 60 ppb		
Date	Scenario 1	Scenario 2	Scenario 3
Sept. 15	0	0.19	0.56
Sept. 16	0.24	0.24	0.48
Sept. 17	0	0	0
Sept. 18	0.13	0.13	0.13
Sept. 19	0	0	0
Sept. 20	0.58	0.77	1.16

Table 11.21: Reduction in total area exceeding threshold of 70 ppb, E85 scenarios

	E85 70 ppb		
Date	Scenario 1	Scenario 2	Scenario 3
Sept. 15	2.7	6.30	10.81
Sept. 16	33.33	33.33	66.67
Sept. 17	0.79	1.32	3.17
Sept. 18	4.27	4.74	9.00
Sept. 19	0.74	1.11	2.21
Sept. 20	2.84	3.79	9.00

For the B100 scenarios, the reduction in total area exceeding a threshold of 60 ppb is negligible compared to the ECT A case, as shown in Table 11.224. A small increase is found in Scenario 3. Similar results were observed for all B100 scenarios when the threshold is set to 70 ppb, as shown in Table 11.23.

Table 11.22: Reduction in total area exceeding threshold of 60 ppb, B100 scenarios

	B100 60 ppb		
Date	Scenario 1	Scenario 2	Scenario 3
Sept. 15	0	0	0
Sept. 16	0	0	0
Sept. 17	0	0	0
Sept. 18	0	0	0
Sept. 19	0	0	0
Sept. 20	0	0	-0.19

Table 11.23: Reduction in total area exceeding threshold of 70 ppb, B100 scenarios

	B100 70 ppb		
Date	Scenario 1	Scenario 2	Scenario 3
Sept. 15	0	0	0
Sept. 16	0	0	0
Sept. 17	0	0	0
Sept. 18	0	0	0
Sept. 19	0	0	0
Sept. 20	0	-0.47	-4.74

Table 11.24 lists the percentage reduction in area exceeding thresholds of 60 and 70 ppb for the combined biofuel case (100% of E85 and 100% B100). When the threshold is equal 60 ppb, the maximum reduction achieved is 1.16% and the minimum is 0. However, when the threshold is set as 70 ppb, the maximum reduction is 66.67%, while the minimum is 2.21%.

Table 11.24: Reduction in total area exceeding threshold of 60 ppb (and 70 ppb), (E85 + B100) scenario

Date	(E85+B100) 60 ppb	(E85+B100) 70 ppb
Sept. 15	0.56	9.91
Sept. 16	0.48	66.67
Sept. 17	0	3.17
Sept. 18	0.13	8.53
Sept. 19	0	2.21
Sept. 20	1.16	9.00

11.2.3.3 Time integrated area above a threshold 1-hour average O_3 Concentration

The time integrated area exceeding a threshold is the summation of the area of grid cells exceeding a threshold ozone concentration in a given hour, summed over all hours in the day of interest. Results for the PHEV scenarios are shown in Tables 11.25 and 11.26. For the 60 ppb threshold, the maximum reduction achieved is 3.28 (in Scenario 1). However, small increases relative to the ECT A, in time integrated area, are observed in Scenarios 1 and 2 (0.03% and 0.034%). For the 70 ppb threshold, Table 11.26 lists the reduction in time integrated area when the threshold is 70 ppb. The maximum reduction achieved is 66.67% in scenario 3, and the minimum reduction is 1.66% in scenario 2.

Table 11.25: Reduction (%) in Time Integrated Area above 60 ppb, PHEVs

	PHEVs 60 ppb		
Date	Scenario 1	Scenario 2	Scenario 3
Sept. 15	3.28	1.40	2.57
Sept. 16	1.90	0.14	0.99
Sept. 17	-0.03	-0.034	0.19
Sept. 18	0.94	0.55	1.33
Sept. 19	1.02	0.66	0.88
Sept. 20	0.70	0.48	1.28

Table 11.26: Reduction (%) in Time Integrated Area above 70 ppb, PHEVs

	PHEVs 70 ppb		
Date	Scenario 1	Scenario 2	Scenario 3
Sept. 15	22.49	8.88	14.20
Sept. 16	33.33	33.33	66.67
Sept. 17	6.51	3.26	6.77
Sept. 18	8.82	2.70	8.09
Sept. 19	3.391	1.66	3.39
Sept. 20	5.76	3.55	8.65

In the E85 scenarios, the maximum reduction when the threshold is set as 60 ppb is 3.56% (Scenario 3), as shown in Table 11.27. For the 70 ppb threshold, Table 11.28 shows that the maximum reduction relative to ECT A (66.67%) is observed in Scenario 2, and the minimum reduction is 1.37% in Scenario 1.

Table 11.27: (%) Reduction in Time Integrated Area above 60 ppb, E85

	E85 60 ppb		
Date	Scenario 1	Scenario 2	Scenario 3
Sept. 15	1.12	1.82	3.56
Sept. 16	0.68	1.26	2.53
Sept. 17	0.08	0.22	0.59
Sept. 18	0.72	1.13	2.27
Sept. 19	0.17	0.36	0.63
Sept. 20	0.26	0.60	1.42

Table 11.28: Reduction (%) in Time Integrated Area above 70 ppb, E85

	E85 70 ppb		
Date	Scenario 1	Scenario 2	Scenario 3
Sept. 15	3.55	7.69	14.20
Sept. 16	33.33	33.33	66.67
Sept. 17	1.37	3.60	7.54
Sept. 18	4.90	6.37	13.97
Sept. 19	1.54	2.59	4.74
Sept. 20	4.99	6.76	13.97

The time integrated area above a threshold of 60 ppb increases in all B100 scenarios compared to the ECT A, as shown in Table 11.29; no reduction is observed. The maximum increase is 0.19 % in Scenario 3. When the threshold is set as 70 ppb, the same pattern is observed, as shown in Table 11.30.

Table 11.29: Reduction (%) in Time Integrated Area above 60 ppb, B100

	B100 60 ppb		
Date	Scenario 1	Scenario 2	Scenario 3
Sept. 15	-0.09	-0.09	-0.19
Sept. 16	-0.05	-0.05	-0.09
Sept. 17	-0.02	-0.02	-0.02
Sept. 18	0	0	-0.03
Sept. 19	-0.02	-0.02	-0.02
Sept. 20	0	-0.02	-0.05

Table 11.30: Reduction (%) in Time Integrated Area above 70 ppb, B100

	B100 70 ppb		
Date	Scenario 1	Scenario 2	Scenario 3
Sept. 15	0	0	0
Sept. 16	0	0	0
Sept. 17	0	0	-2.57
Sept. 18	0	0	-2.45
Sept. 19	0	0	0
Sept. 20	0	-0.22	-5.54

For the combined biofuels case the reduction in time integrated area is still less than E85 100% scenario. For a threshold of 60 ppb, the maximum reduction is 3.37%, and when the threshold is set as 70 ppb, the maximum reduction achieved is 66.67% as shown in Table 11.31.

Table 11.31: Reduction (%) in Time Integrated Area above (60 and 70) ppb, (biofuels combination)

Date	(E85+B100)	(E85+B100)
	60 ppb	70 ppb
Sept. 15	3.37	13.61
Sept. 16	2.39	66.67
Sept. 17	0.56	7.198
Sept. 18	2.16	13.73
Sept. 19	0.61	4.74
Sept. 20	1.35	13.30

11.2.3.4 Time integrated, concentration weighted population above a threshold

Time integrated, concentration weighted population above a threshold is the product of population in the grid cells that have a ground level ozone concentration higher than the threshold, multiplied by the difference between the predicted concentration and the threshold for

each hour. The value is calculated for each grid cell and is summed for each in each day. The thresholds are set as 0, 60 and 70 ppb. This metric will be referred to as an exposure metric.

It is valuable to use threshold of 0 to compare the exposure level between the ECT A and the test cases. Table 11.32 shows the reduction (as %) in total daily population exposure exceeding a threshold of 0 ppb for PHEVs case. There is reduction in total daily population exposure in all scenarios. The changes in total daily population exposure to a threshold of 0 ppb for the E85 scenarios are shown in Table 11.33. Unlike PHEVs scenarios, E85 has an increase in total daily population exposure in all days except for the last day in the episode. Table 11.34 lists the changes in the B100 scenarios. A reduction is achieved in all the episode days except for the last day (an increase is observed in that day).

Table 11.32: Total population exposure (%) above 0 ppb, PHEVs

	PHEVs 0 ppb		
Date	Scenario 1	Scenario 2	Scenario 3
Sept. 15	0.189	0.157	0.168
Sept. 16	0.202	0.195	0.118
Sept. 17	0.309	0.255	0.219
Sept. 18	0.373	0.308	0.301
Sept. 19	0.406	0.313	0.347
Sept. 20	0.478	0.384	0.510

Table 11.33: Total population exposure (%) above 0 ppb, E85

	E85 0 ppb		
Date	Scenario 1	Scenario 2	Scenario 3
Sept. 15	-0.007	-0.011	-0.02
Sept. 16	-0.052	-0.087	-0.171
Sept. 17	-0.057	-0.095	-0.184
Sept. 18	-0.013	-0.02	-0.032
Sept. 19	-0.009	-0.013	-0.0204
Sept. 20	0.049	0.083	0.176

Table 11.34: Total population exposure (%) above 0 ppb, B100

B100 0 ppb			
Date	Scenario 1	Scenario 2	Scenario 3
Sept. 15	0	0	0.002
Sept. 16	0.002	0.004	0.007
Sept. 17	0.001	0.002	0.004
Sept. 18	0	0	0
Sept. 19	0	0	0
Sept. 20	-0.002	-0.004	-0.007

When the threshold is set as 60 ppb, the maximum reduction achieved in the exposure metric for the PHEV cases is 9.81% (in Scenario 3), as shown in Table 11.35. In all the E85 scenarios, a reduction in total daily population exposure is achieved with maximum reduction of 9.88% in Scenario 3, as shown in Table 11.36. Table 11.37 presents the results for B100 scenarios. All B100 scenarios have an increase in the exposure metric.

Table 11.35: Total population exposure (%) above 60 ppb, PHEVs

PHEVs 60 ppb			
Date	Scenario 1	Scenario 2	Scenario 3
Sept. 15	5.17	2.09	4.49
Sept. 16	5.26	1.02	3.05
Sept. 17	4.36	2.28	3.80
Sept. 18	4.75	1.69	4.95
Sept. 19	4.78	2.56	4.49
Sept. 20	8.60	5.71	9.81

Table 11.36: Total population exposure above 60 ppb (%), E85

E85 60 ppb			
Date	Scenario 1	Scenario 2	Scenario 3
Sept. 15	1.685	2.81	5.71
Sept. 16	1.41	2.38	4.88
Sept. 17	1.06	1.79	3.71
Sept. 18	2.43	4.08	8.31
Sept. 19	1.38	2.32	4.73
Sept. 20	2.89	4.86	9.88

Table 11.37: Total population exposure above 60 ppb (%), B100

B100 60 ppb			
Date	Scenario 1	Scenario 2	Scenario 3
Sept. 15	-0.05	-0.086	-0.17
Sept. 16	-0.04	-0.062	-0.12
Sept. 17	-0.02	-0.037	-0.074
Sept. 18	-0.04	-0.06	-0.13
Sept. 19	-0.016	-0.03	-0.052
Sept. 20	-0.117	-0.20	-0.39

The results for the 70 ppb threshold cases for scenarios show the same trends, but with higher maximum reductions (Table 11.38, 11.39, and 11.40).

Table 11.38: Total population exposure above 70 ppb (%), PHEVs

PHEVs 70 ppb			
Date	Scenario 1	Scenario 2	Scenario 3
Sept. 15	38.75	11.13	19.12
Sept. 16	44.76	44.75	78.77
Sept. 17	13.49	8.16	14.32
Sept. 18	15.14	-0.49	8.86
Sept. 19	12.53	6.30	11.61
Sept. 20	27.06	12.82	22.25

Table 11.39: Total population exposure above 70 ppb (%), E85

E85 70 ppb			
Date	Scenario 1	Scenario 2	Scenario 3
Sept. 15	6.37	10.37	19.94
Sept. 16	45.37	65.91	93.83
Sept. 17	4.92	8.12	15.82
Sept. 18	7.11	11.79	22.67
Sept. 19	3.86	6.46	13.05
Sept. 20	7.23	11.97	23.57

Table 11.40: Total population exposure above 70 ppb (%), B100

	B100 70 ppb		
Date	Scenario 1	Scenario 2	Scenario 3
Sept. 15	-2.04	-0.34	-6.80
Sept. 16	-14.13	-2.36	-47.33
Sept. 17	-1.16	-0.19	-3.86
Sept. 18	-1.28	-0.21	-4.27
Sept. 19	-0.46	-0.08	-1.52
Sept. 20	-3.35	-0.56	-11.25

The changes in the exposure metric for thresholds of 0, 60 and 70 ppb for the combined biofuels case is shown in Table 11.41. If the threshold is set as 60 (or 70 ppb), then the changes are predicted to reduce exposure. However, when the threshold is 0 ppb, exposure is predicted to increase.

Table 11.41: Total population exposure above 0, 60 and 70 ppb (%), (E85+B100)

Date	(E85+B100)	(E85+B100)	(E85+B100)
	0 ppb	60 ppb	70 ppb
Sept. 15	-0.018	5.53	19.36
Sept. 16	-0.164	4.74	92.68
Sept. 17	-0.18	3.62	15.46
Sept. 18	-0.033	8.17	22.32
Sept. 19	-0.021	4.67	12.89
Sept. 20	0.167	9.46	22.53

11.2.3.5 CO Concentrations

While ozone is a secondary air pollutant and its formation requires reactions to occur in the atmosphere, CO is a primary air pollutant, emitted directly by both vehicles, and to a lesser extent, power plants. Based on the emission factors adapted from Jacobson (2007), E85 CO emissions are increased by 5% relative to a gasoline base case. However, B100 emission rates are decreased by 45% relative to a diesel base case (Sharp 1990). Table 11.42 shows the changes in PHEVs CO concentrations compared to the ECT A scenario.

Table 11.42: Maximum CO concentrations (ppb), PHEVs

	PHEVs CO concentration (ppb)			
Date	ECT A	Scenario 1	Scenario 2	Scenario 3
Sept. 15	601.	561.	561.	566.
Sept. 16	963.	883.	883.	893.
Sept. 17	1453.	1337.	1337.	1352.
Sept. 18	1922.	1779.	1779.	1797.
Sept. 19	1907.	1754.	1754.	1773.
Sept. 20	1707.	1603.	1603.	1616.

Table 11.42 shows a benefit in CO reduction for all PHEVs scenarios; the reduction in CO concentration in E85 scenarios is lower than the reduction in PHEVs scenarios. Table 43 shows CO concentrations for both the ECT A and E85 scenarios. Also, as the replacement of gasoline based fuel with ethanol fuel increases, the emission rates of CO also increase. In contrast, B100 scenarios resulted in essentially no changes in CO concentrations (Table Tsk 3.44). The combined biofuels case (100% of E85 and 100% of B100) shows similar results as the third scenario in E85 case, which accounts for 100% replacement of gasoline based fuel with E85 (Table Tsk 3.45).

Table 11.43: Maximum CO concentrations (ppb), E85

E85 CO concentration (ppb)				
Date	ECT A	Scenario 1	Scenario 2	Scenario 3
Sept. 15	601.	605.	607.	613.
Sept. 16	963.	970.	975.	987.
Sept. 17	1453.	1464.	1471.	1488.
Sept. 18	1922.	1935.	1944.	1965.
Sept. 19	1907.	1920.	1929.	1952.
Sept. 20	1707.	1716.	1722.	1738.

Table 11.44: CO concentrations (ppb), B100

B100 CO concentration (ppb)				
Date	ECT A	Scenario 1	Scenario 2	Scenario 3
Sept. 15	601.	601.	601.	601.
Sept. 16	963.	963.	963.	963.
Sept. 17	1453.	1453.	1453.	1453.
Sept. 18	1922.	1922.	1922.	1922.
Sept. 19	1907.	1907.	1907.	1907.
Sept. 20	1707.	1707.	1707.	1707.

Table 11.45: CO concentrations (ppb), (E85 + B100)

Date	ECT A	(E85+B100)
		CO (ppb)
Sept. 15	601.	613.
Sept. 16	963.	987.
Sept. 17	1453.	1487.
Sept. 18	1922.	1965.
Sept. 19	1907.	1952.
Sept. 20	1707.	1737.

Spatial distribution for CO concentrations for the first scenario in PHEVs case, third scenario in E85 case and the combination biofuels case are shown in Figure 11.6. These values represent maximum CO concentration in (ppb) for Austin five-county area for the future year 2030 regardless the time or the location.

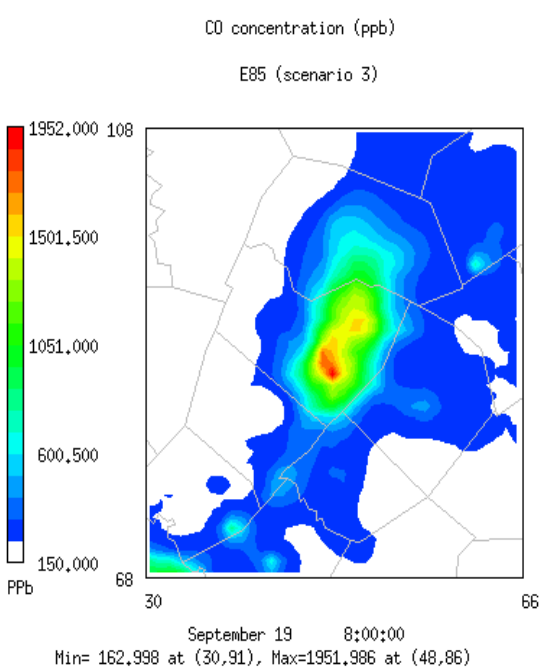

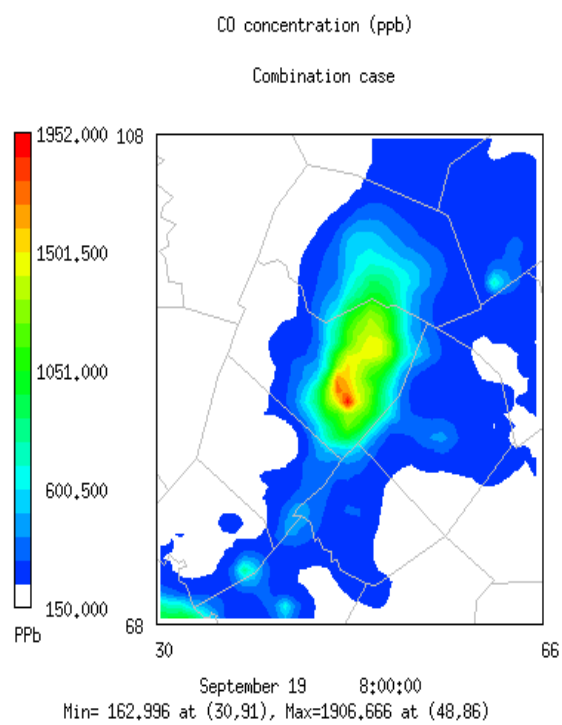

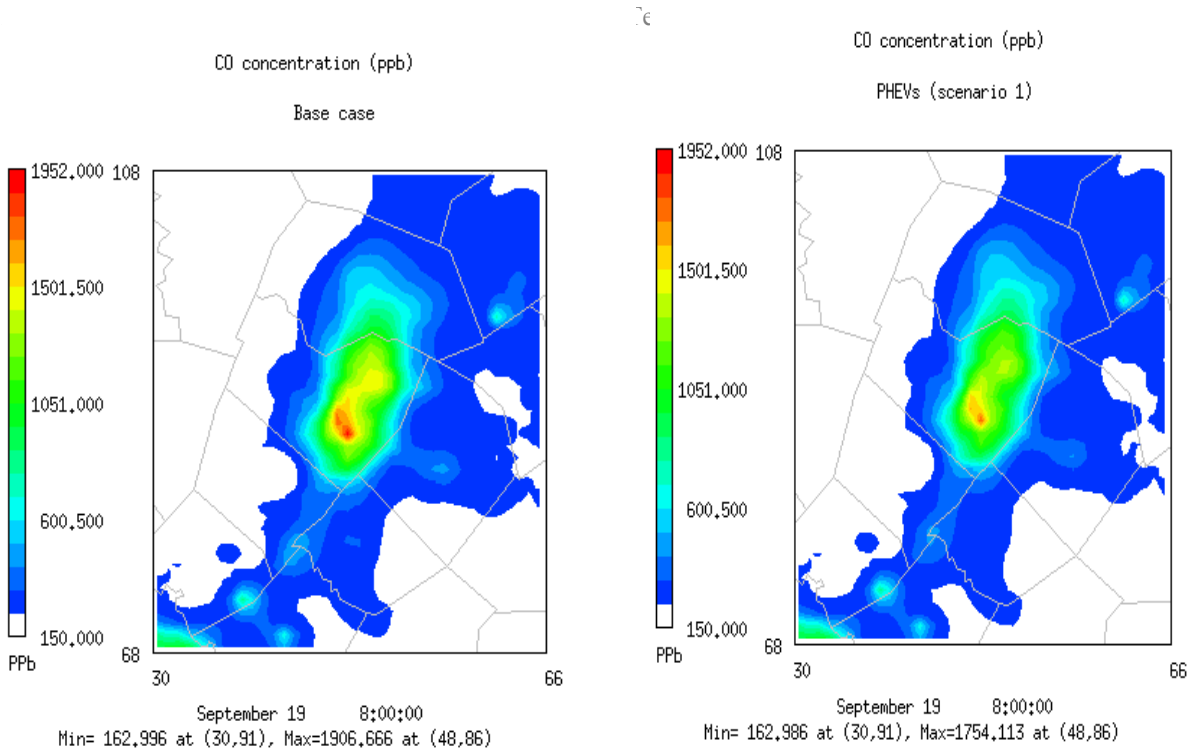

Figure 11.6: CO concentration (ppb) for the ECT A, PHEVs scenario one, E85 scenario three and the combination case.

11.2.3.6 Aldehyde concentrations

Table 11.46 shows aldehyde concentrations for the three scenarios in PHEV cases, compared to the ECT A for the future year 2030. Aldehyde concentrations are decreased for both scenario 1 and 2; however, Scenario 3 shows a slight increase in aldehyde concentrations.

Table 11.46: Ald. concentrations (ppb), PHEVs

PHEVs ALD. concentration (ppb)				
Date	ECT A	Scenario 1	Scenario 2	Scenario 3
Sept. 15	10.1	10.0	10.0	10.2
Sept. 16	12.8	12.6	12.6	13.0
Sept. 17	14.5	14.2	14.2	14.9
Sept. 18	16.5	16.1	16.1	17.0
Sept. 19	12.4	11.9	11.9	12.9
Sept. 20	12.9	12.7	12.7	13.3

In all E85 scenarios (Table 11.47), aldehyde concentrations are higher than in PHEVs scenarios and are higher than the ECT A, largely due to increased emissions of reactive VOCs in these scenarios. B100 scenarios show a small increase in aldehyde cncentrations, despite a reduction in VOC emissions, however (Table 11.48), indicating that the aldehyde concentrations have a complex dependence on the overall reactivity and composition of the emissions. Table 11.49 shows that the combined biofuels scenario is comparable to E85 scenario 3.

Table 11.47: Ald. concentrations (ppb), E85

E85 ALD. concentration (ppb)				
Date	ECT A	Scenario 1	Scenario 2	Scenario 3
Sept. 15	10.1	10.2	10.3	10.6
Sept. 16	12.8	13.1	13.2	13.7
Sept. 17	14.5	15.0	15.4	16.2
Sept. 18	16.5	17.2	17.6	18.8
Sept. 19	12.4	13.1	13.7	15.0
Sept. 20	12.9	13.4	13.7	14.4

Table 11.48: Ald. concentrations (ppb), B100

B100 ALD. concentration (ppb)				
Date	ECT A	Scenario 1	Scenario 2	Scenario 3
Sept. 15	10.1	10.1	10.1	10.1
Sept. 16	12.8	12.8	12.9	12.9
Sept. 17	14.5	14.6	14.6	14.7
Sept. 18	16.5	16.5	16.6	16.6
Sept. 19	12.4	12.4	12.4	12.4
Sept. 20	12.9	13.0	13.0	13.1

Table 11.49: Ald. concentrations (ppb), (E85 + B100)

Date	ECT A	(E85+B100) ALD. (ppb)
Sept. 15	10.1	10.6
Sept. 16	12.8	13.8
Sept. 17	14.5	16.4
Sept. 18	16.5	18.9
Sept. 19	12.4	15.0
Sept. 20	12.9	14.6

Spatial distribution for aldehyde concentrations for the first scenario in the PHEVs cases, third scenario in E85 cases and the combination case are shown in Figure 11.7.

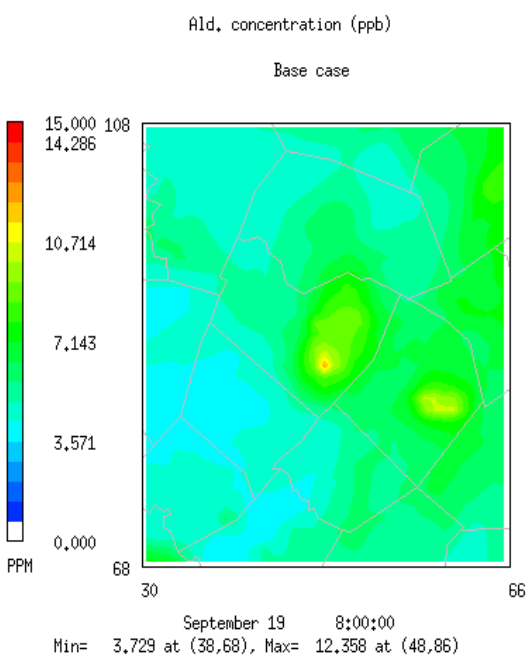

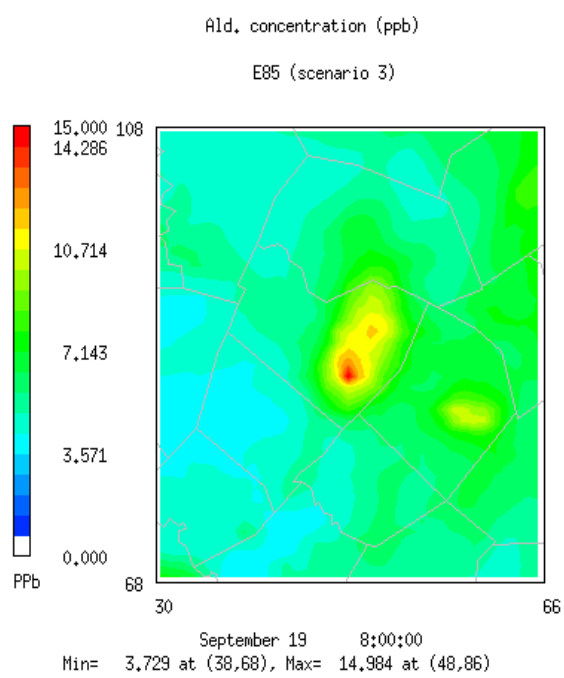

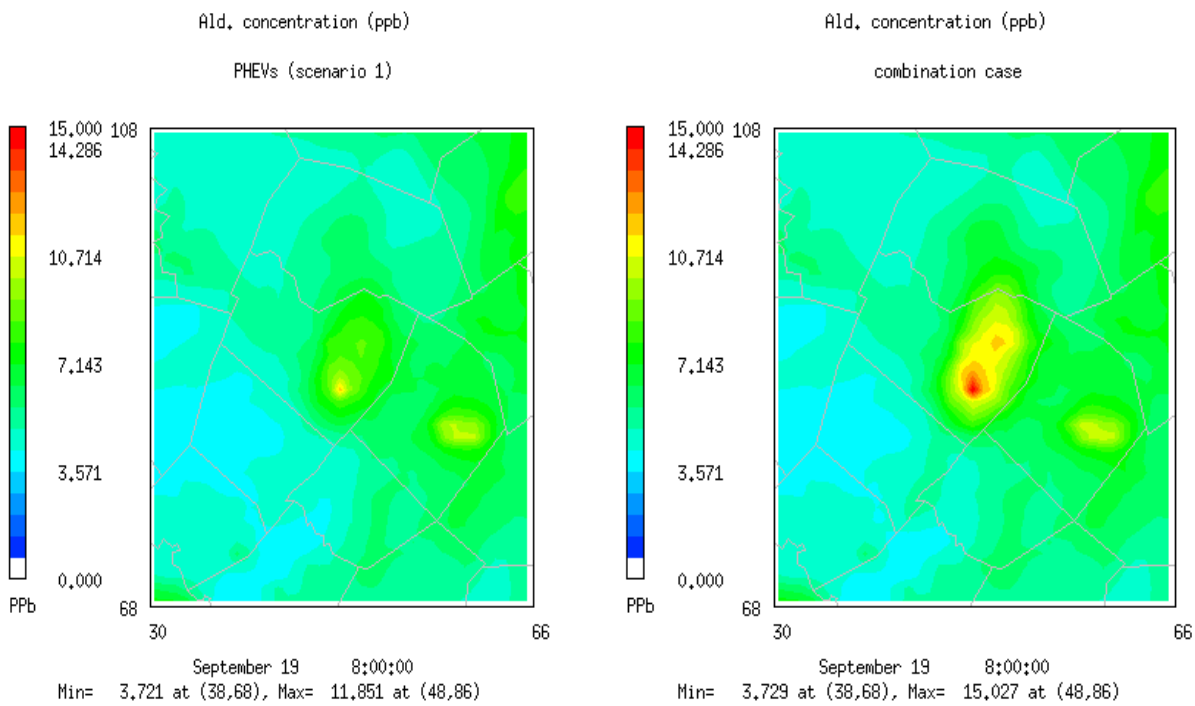

Figure 11.7: Ald. concentration (ppb) for the ECT A, PHEVs scenario one, E85 scenario three and the combination case.

11.2.4 Conclusion

This task report has described the air quality impacts of E85 and biodiesel at a variety of market penetrations. Since the changes in a wide variety of air quality metrics for biofuels is relatively small, compared to simulations assuming petroleum derived fuels, the summaries provided here focus on full market penetration of both E85 and B100 (the combined biofuels case). These were compared to a market penetration of 17% for PHEVs (the market penetration that can be achieved using only excess night-time capacity currently available in the Austin area) and assuming emission rates per unit of power generated remain constant (PHEV Scenario 2).

Table 11.50 compares maximum ozone concentrations for the scenarios. Tables 11.51 to 11.53 compare three different metrics related to ozone exposures for the scenarios.

Table 11.50: Maximum 1-hr O_3 concentration.

	maximum daily 1-hr O_3 (ppb)
Base case (ECT A)	84.65
PHEVs scenario 2	83.78
Combination scenario	83.58

Table 11.51: Reduction (%) in total population exposure to O_3 above 70 ppb.

Date	PHEVs scenario 2	(B100 + E85)
Sept. 15	11.13	19.36
Sept. 16	44.75	92.68
Sept. 17	8.16	15.46
Sept. 18	-0.49	22.32
Sept. 19	6.30	12.89
Sept. 20	12.82	22.53

Table 11.52: Reduction in total population exposure (%) to O3 above 60 ppb.

Date	PHEVs scenario 2	(B100 + E85)
Sept. 15	2.09	5.53
Sept. 16	1.02	4.74
Sept. 17	2.28	3.62
Sept. 18	1.69	8.17
Sept. 19	2.56	4.67
Sept. 20	5.71	9.46

Table 11.53: Changes in total population exposure (%) to O_3 above 0 ppb.

Date	PHEVs scenario 2	(B100 + E85)
Sept. 15	0.157	-0.018
Sept. 16	0.195	-0.164
Sept. 17	0.255	-0.18
Sept. 18	0.308	-0.033
Sept. 19	0.313	-0.021
Sept. 20	0.384	0.167

Although the behaviors are complex, and the results depend on the nature of the air quality improvement metric that is employed, an electrification of roughly 20% of the fleet results in comparable air quality changes to a complete substitution with biofuels.

11.3 Engine modeling

11.3.1 Introduction

The previous section examined the potential impacts of biofuel adoption on regional air quality, and based on emission characteristics of biofuels available in the literature, found that changes in regional air quality would be smaller than those anticipated for electrification of the vehicle fleet. The purpose of this section is to examine alternative emission scenarios for biofuels, specifically biodiesel, due to differences in fuel composition. The composition of ethanol fuels will not be affected by the source of the feedstock, so it was appropriate to use literature derived values without additional analyses. For the biodiesels, however, fuel properties may vary depending on the type of feedstock used, and therefore estimates of emissions were made for the feedstocks considered in this work. As will be described in this section, emission estimates were made based on a combined experimental and computational approach, and the resulting estimated emissions were generally consistent with the estimates used in the previous section.

11.3.2 Computational and Experimental Methods

Multiple engine and emission simulation software tools are available for estimating emissions from internal combustion engines, however, many of the engine and exhaust simulators require engine maps that relate engine speed and torque to emissions. These engine maps can only be obtained through physical testing, which is impossible in the case of the biodiesels to be considered in this work, since most exist only in very small quantities. Based on a review of the state of the science on engine simulators (DOE, 2006), the approach that was employed in this work was to use a simulator that bases emissions on fuel properties, Gamma Technologies "GTPower". This engine simulation approach utilizes a combined computational and experimental approach. Specifically, the software developers recommend measuring in-cylinder pressure traces and fuel injection pressure profiles for model input and model calibration, and the model predictions should be calibrated with engine test data. Even with calibration and engine data, emission estimates are still subject to uncertainties. Nevertheless, these estimates provide a reasonable method to assess the extent to which alternative biodiesel formulations might impact emission characteristics.

For this work, emission estimation involved the following tasks:

1. Utilizing a standard single cylinder diesel engine, correlate simulation emissions estimates to recorded emissions obtained through physical testing using conventional No. 2 diesel fuel.
2. Utilizing the same procedures and standard single cylinder diesel engine as in Step 1, test neat soy-biodiesel fuel.
3. Once the baseline was established, extend the simulation model to biofuels via estimates of fuel properties.

Engine testing was done in the University of Texas Mechanical Engineering Department with a four-stroke single cylinder YANMAR diesel engine (model L100AE-DE). The specifications for the YANMAR engine, required by the GTPower software, are listed in Table 5-54.

Engine Type	Single-Cylinder, 4-Cycle, Air-Cooled Diesel
Combustion System	Direct Injection System
Bore	86 mm
Stroke	70 mm
Displacement Volume	406 cm^3
Continuous Output	6.6 kW
Rated Speed	3600 RPM
Compression Ratio	19.3
Fuel Injection Pressure	196 bar

Table 11.54. Specifications of YANMAR diesel engine (model L100AE-DE)

In addition, the software requires valve lift data, which were measured in the UT engine laboratory, and are shown in Figure 11.8. The zero-degree and 180-degree crank angles are the top dead center and bottom dead center, respectively.

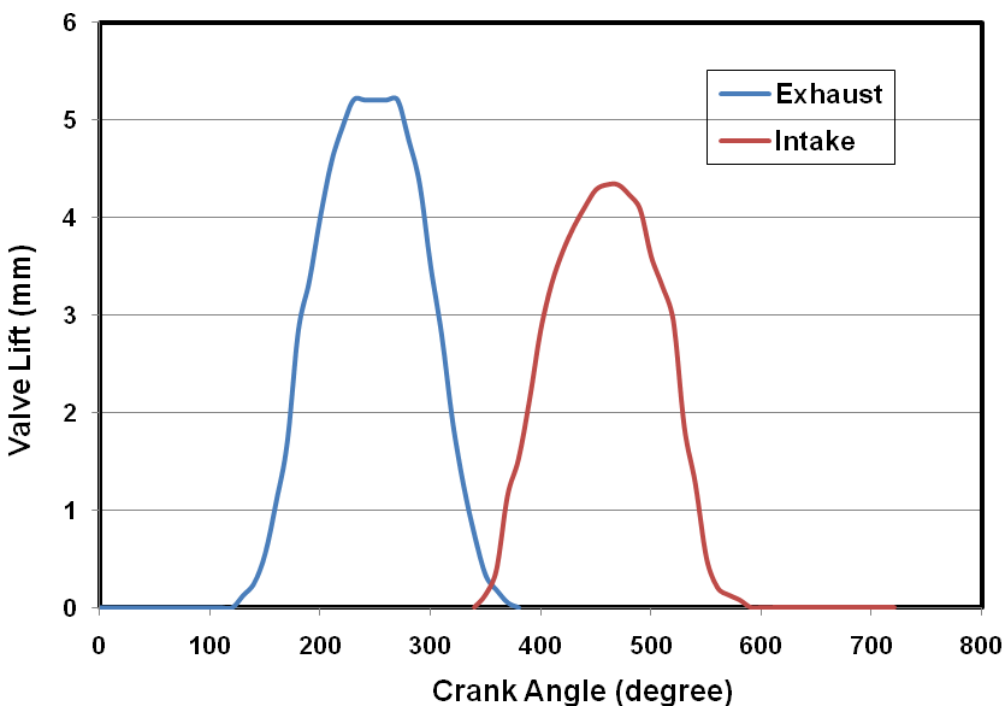

Figure 11.8. Measured valve lift curves of single cylinder YANMAR diesel engine

The predictive tool for estimating emissions in GT-Power is referred to as Direct Injection Jet (DIJet). The total injected fuel mass is divided into five radial zones and multiple axial zones. At each time step during the fuel injection period, an axial slice with five radial zones is injected into the engine cylinder. The DIJet model only analyzes the fuel plume from one nozzle hole. The fuel mass in each axial slice is determined by the fuel injection pressure at that time step and

the elapsed time since the last zones were injected. The injected fuel mass in each time step is divided equally among the five radial zones.

Each zone contains subzones for liquid fuel, unburned vapor fuel and entrained air, and burned gases. As the liquid fuel is injected into the cylinder, the fuel entrains air and begins to evaporate, thus forming the unburned subzone. The outer zones entrain air more quickly than the inner zones, thus decreasing their velocity more quickly due to momentum conservation and resulting in less penetration distance, as shown in Figure 11.9.

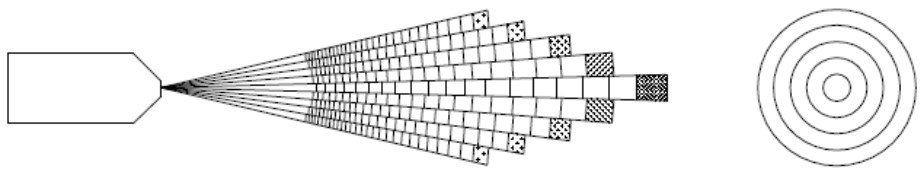

Figure 11.9. Fuel jet breakup into radial and axial zones in a DIJet model (Gamma Technologies, 2006)

The zonal temperature is calculated based on the injected fuel temperature, entrained air temperature, and the effect of fuel evaporation. The zonal fuel-to-air ratio is determined by the vapor fuel mass and entrained air mass in each unburned subzone. When the combination of cylinder pressure, zonal temperature, and fuel-to-air ratio becomes combustible, the fuel in the unburned subzone ignites and results in a change of temperature and composition. All combustion products are then moved to the burned subzone.

The DIJet model predicts the combustion burn rate by predicting the evaporation rate of droplets that have broken from the injected stream of fuel and the entrainment of air by the fuel jet. To accurately predict the fuel jet velocity as a function of time, the DIJet model requires an accurate input of fuel injection pressure as a function of crank angle. The burn rate predicted by the DIJet model is extremely sensitive to the fuel injection profile and timing. To determine these parameters, the engine test system shown in Figure 11.10 was used.

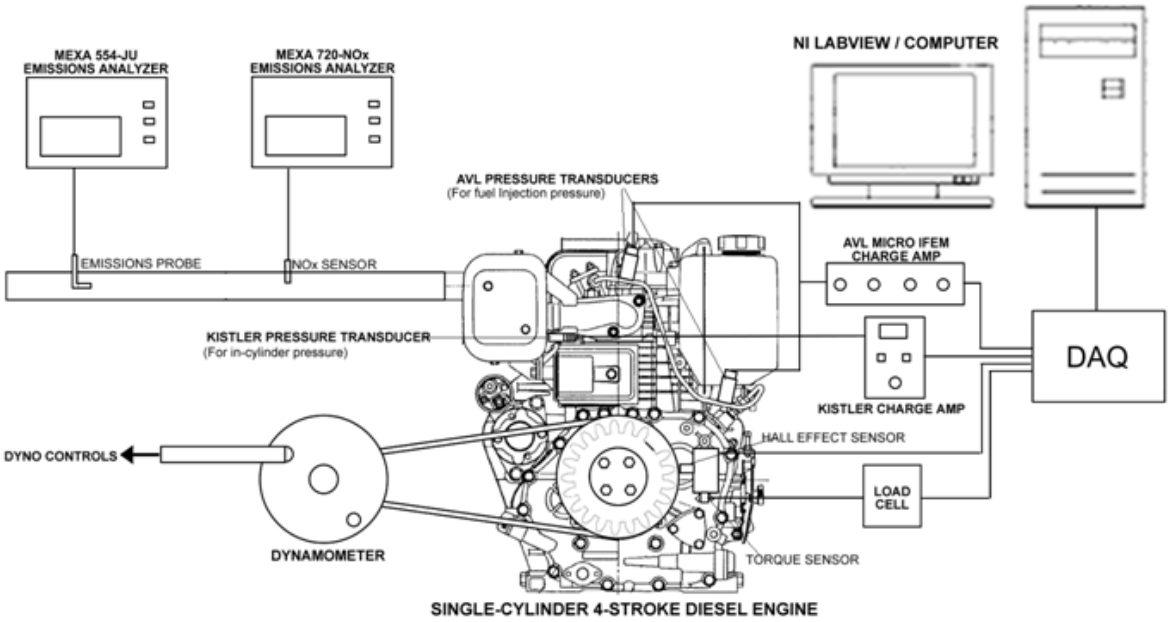

Figure 11.10: Schematic diagram of experimental setup

The hardware and software used in physical testing setup included:

1. Yanmar single-cylinder, vertical-4 cycle air-cooled diesel engine
2. AVL Equipment
   - Two AVL high-pressure transducers (SL31D-2000) with a measuring range of 0 to 2000 bar.
   - A microIFEM Combi Module 4C3x charge amplifier
   - A serial interface cable, 5m
   - A power supply cable, 10m
   - Two BNC connecting cables E109 – 1.5
   - Two clamp-on ferrites
3. A National Instruments DAQ system
4. A Hall Effect sensor.
5. Dynamometer and controls
6. AVL Software
   - IndiSignal v 2.9
   - Concerto v 4.1
7. National Instruments Labview v 8.6

A Kistler pressure sensor was used to measure pressure variation in the cylinder and the Hall Effect sensor is used to determine crank angle, engine speed, and the position of the piston with respect to the top dead center (TDC) and bottom dead center (BDC).

The Kistler pressure sensor was installed by drilling a threaded port hole (4.95 mm in diameter and 10.2 mm in length) in the YANMAR cylinder head. From that depth, a counter bore of 1 mm diameter was drilled further into the cylinder head, and another bore of the same diameter as the counter bore was drilled from the combustion chamber surface of the head to meet the counter bore at a right angle. This formed a direct passage into the cylinder volume, enabling the

pressure sensor to detect pressure in the cylinder as the piston moved up and down. This was done with as much precision as possible so as not to affect the volume of the cylinder, and thus the cylinder pressure while the engine was running. The Kistler pressure sensor was connected using a BNC connector to the charge amp, which was in turn wired to an analog channel on the CompactRio device.

The Hall Effect sensor senses the teeth on the crank wheel connected to the crankshaft. The wheel has 36 teeth and each tooth denotes 10 degree of crank rotation. The sensor is supplied with 12V from a DC power supply and its output signal (in volts) is fed into the CompactRio for scaling/ manipulation.

The fuel injection pressure profile (pressure versus crank angle) required by the GT-Power DIJet model is the pressure profile in the injector sac, which is a small volume inside the injector between the plunger and the spray nozzles. Figure 11.11 shows a typical fuel injection nozzle of a diesel engine.

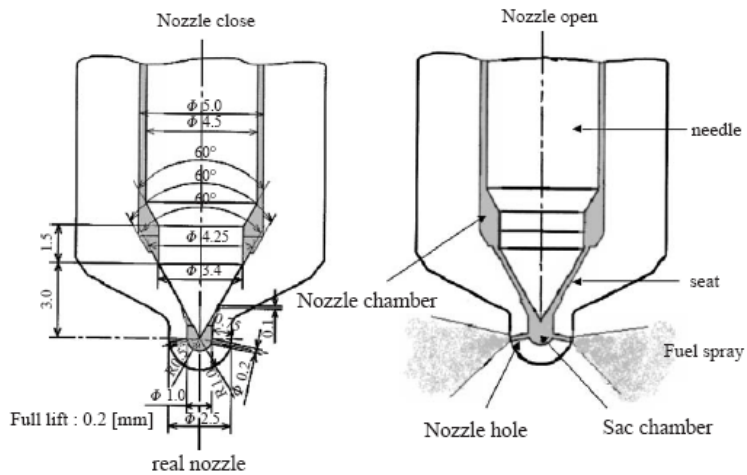

Figure 11.11. Illustration of a fuel injection nozzle of a diesel engine (Takenaka et al, 2005).

The fuel injection pressure sensors available on the market are typically used to measure the injection line pressure, and not the sac pressure due to difficult accessibility, very high pressure, and high frequency response required. A third-party vendor, AVL, provided a solution capable of approximating the fuel injection sac pressure utilizing a pair of fast response absolute pressure transducers installed on the fuel injection line at two different points (fuel pump end and nozzle holder end). Given these pressure readings, the pressure and velocity in the injector sac area can then be computationally determined. The schematic illustration is shown in Figure 11.12.

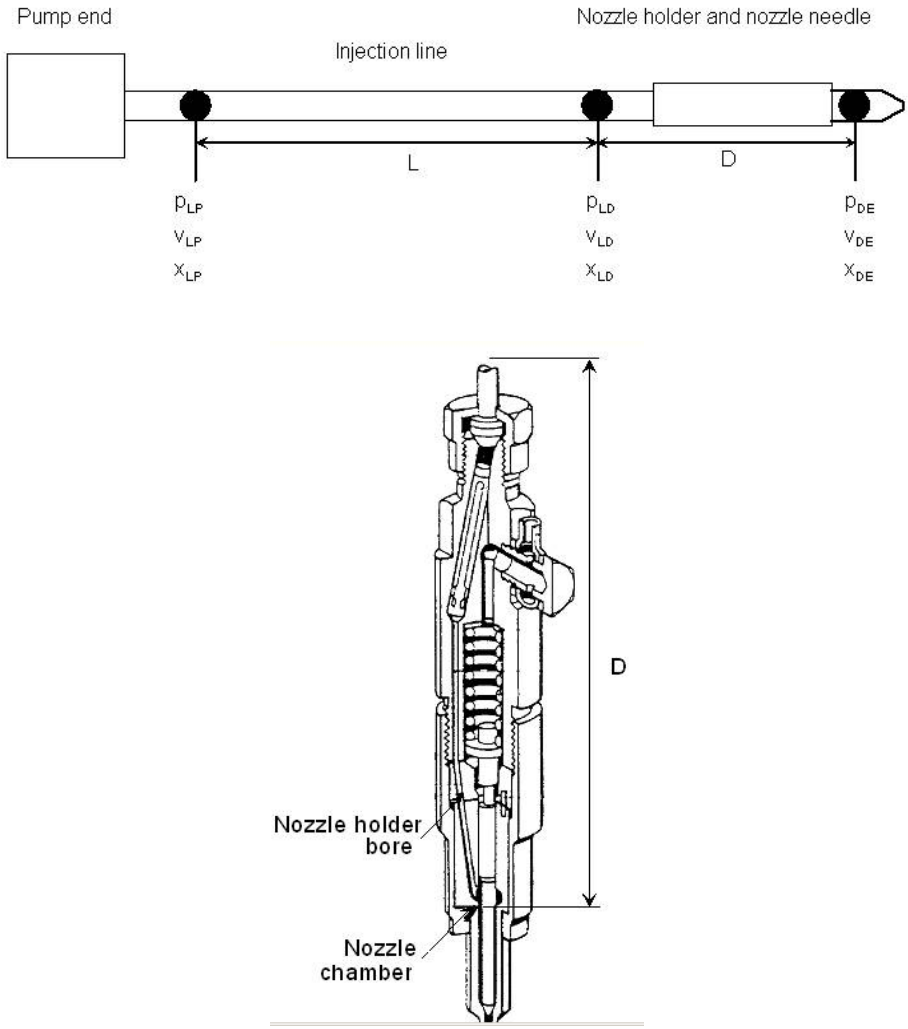

Figure 11.12. Fuel injector sac pressure measurement proposed by AVL

Notes regarding AVL's calculation method for the fuel injector sac pressure:

- The fuel pressure varies along the fuel injection line (300 ~ 350 mm in length). However, the fuel pressure in the nozzle chamber and sac chamber (with a total length of 25 ~ 30 mm) is considered to be uniform in AVL's analysis.
- To increase the computationally determined sac pressure accuracies, a full fuel injection detail analysis, which includes fuel pump, injector line, fuel nozzle, and combustion chamber, was required.

To acquire a fuel injector sac pressure profile for the YANMAR test engine during operation, two AVL high-pressure transducers (SL31D-2000) with a measuring range of 0 to 2000 bar, a microIFEM Combi Module 4C3x charge amplifier, and AVL data acquisition system analysis software of IndiSignal and Concerto were used to acquire data and compute the resulting profile.

Allievi equations, comprehensively described in technical literature, can be used to link the velocity and pressure of the fuel at two separated points along the fuel injection line. As shown in Figure 11.11, if the time-based pressure curves of P_{LP} at the pump end and P_{LD} at the nozzle holder end are known, the fuel velocity curves of V_{LP} and V_{LD} can be determined by using the Allievi equations. The calculated fuel velocity curve of V_{LD} and the measured fuel pressure curve of P_{LD} at the nozzle holder end can then be used to calculate the fuel pressure curve of P_{DE} at the entry into the nozzle chamber by using the Allievi equations again. The fuel pressure in the nozzle chamber and sac chamber is considered to be uniform.

The nozzle chamber fuel pressure curve of P_{DE} is required for the calculation of nozzle needle lift, which is modeled as a mechanical spring/mass/damper system with a degree of freedom. The nozzle needle lift determines the start and end of fuel injection as well as the open nozzle hole area. The fuel injection rate is calculated from this information.

The AVL pressure sensors were installed at the ends of the injection line, one at the fuel pump end and the other at the nozzle holder end, using solder-on adaptors. Two 1-mm diameter holes were drilled into the injection line at the installation locations and aligned with the holes in the adaptors before brazing them to the injection line. The pressure sensors were screwed into the adaptors (tightening torque = 15Nm) creating a 1-mm channel connecting the sensor directly with the fuel flow through the adaptor and the injection line.

The microIFEM Combi Module 4C3x system houses two independent Piezo amplifiers (CG1 and CG2) and two independent MP amplifiers (VG1 and VG2) with different uses. For the current application, strain gauge pressure measurements, that require a precise stable power supply and high gain factor, are desired and the MP amplifiers are suitable for this purpose.

Before connecting both pressure sensors to the VG1 and VG2 channels, the microIFEM was powered on and connected to the serial port on the computer and the IndiSignal application was started. IndiSignal was used to parameterize the amplifier. It displayed all four amplifiers in the microIFEM system and properties required for the relevant amplifiers in use were set (see Table 11.55).

Property	Transducer 1	Transducer 2
Mode	Strain gauge	Strain gauge
Calibration Signal Input Range Transducer Sensitivity Transducer Type Serial Number	 500 bar 0.449 uV/V.bar SL31D-2000 9129	 500 bar 0.447 uV/V.bar SL31D-2000 9130
Bridge supply	4V	4V
Bridge offset:	2350	-201

Table 11.55. Specifications of YANMAR diesel engine (model L100AE-DE)

After adjusting the settings, IndiSignal calculates a Signal Calibration Factors (SCF) for both sensors based on the following equations:

$$A \leq \frac{10^7\,[V]}{S\left[\frac{\mu V}{V \cdot bar}\right] \cdot p_N\,[bar] \cdot U_B\,[V]}$$

This produces a Signal Calibration Factor (SCF) of:

$$SCF\left[\frac{bar}{V}\right] = \frac{10^6}{S\left[\frac{\mu V}{V \cdot bar}\right] \cdot A \cdot U_B\,[V]}$$

Where A = gain calculated from transducer sensitivity S
P_N = pressure input range (i.e. maximum pressure)
U_B = bridge voltage

This factor is used to convert the output signal from the microIFEM (volts) to pressure in whatever pressure unit is specified by the user in IndiSignal (bar in this case).

After adjusting the settings, the sensors were connected to the VG1 and VG2 channels respectively based on the channel calibration in IndiSignal. The clamp-on ferrules were installed close to the amplifier end of the sensor cables to reduce high frequency noise in the signals. Two BNC cables were connected the output from the microIFEM to the DAQ system with two low-pass signal filters installed between the BNC cables and the DAQ system to attenuate low frequency noise in the signals into the DAQ.

Before fuel pressure measurements were taken, the pressure signals were zeroed by disconnecting one end of the injection line, thereby exposing the transducers to the barometric pressure in the laboratory. The data-sampling rate was adjusted to capture a sufficient amount of data to support the AVL computations of fuel injector sac pressure (120 kHz). Data logged include engine speed, torque from the dynamometer controls, pressure pulses from both pressure sensors, and crank angle position using signal from the Hall Effect sensor.

AVL's Concerto application was used to analyze the measured data. In Concerto, a Graphical Formula Editor (CalcGraf) was used to model the fuel injection system by using the "InjectionRate" macro. This function took the time-based pressure profiles measured at the fuel pump end and nozzle holder end as inputs and calculated nozzle needle lift, injection rate, sac fuel velocity, sac pressure and start of injection.

The processing of pressure inputs was done with a detailed knowledge of the dimensions and properties of the injector nozzle. A spare injector nozzle was obtained and dissected to reveal the internal parts, whose dimensions were subsequently measured. To find the fuel injector nozzle internal component details required by the "InjectionRate" macro, a high-precision vernier caliper was used to measure the length dimensions, an optical comparator was used to measure the angular dimensions, and a weight scale was used to measure the mass. Other parameters

required by the macro included engine speed, distance from the sac to the nozzle holder end of the line, calculation range (in crank angle degrees), and calculation resolution (in crank angle degrees). Some of the required dimensions in the fuel injector nozzle are shown in Figures 11.13 and 11.14.

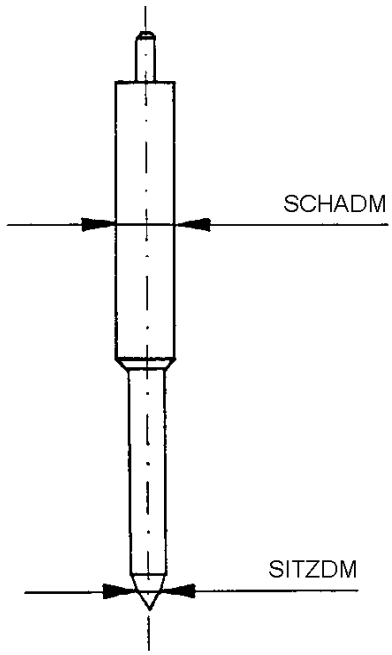

Figure 11.13: Fuel injector nozzle holder and needle dimensions required by CalcGraf

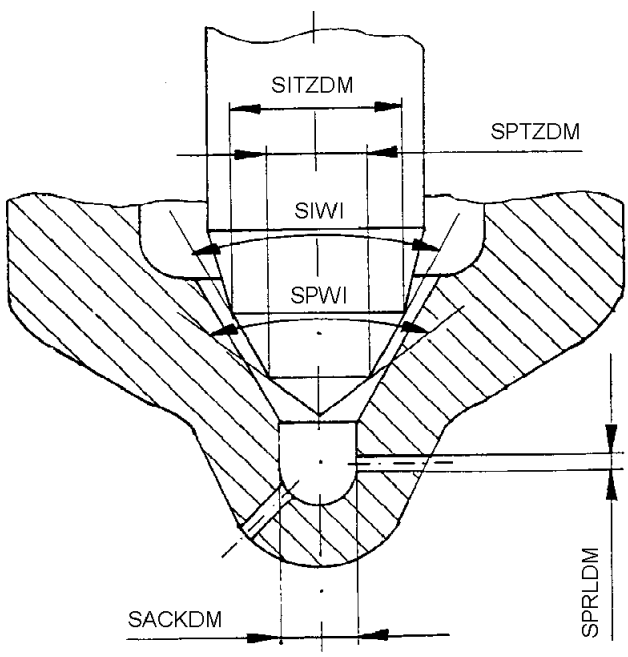

Figure 11.14: Close-up of fuel injector nozzle tip and internal dimensions required by CalcGraf

The amount of engine intake air flow has significant influences on the engine performance and emissions. In GT-Power modeling, users are required to input flow arrays of "discharge

coefficient" versus "valve lift" for both intake and exhaust valves. The discharge coefficient is defined as the ratio of the effective flow area to a reference flow area when the air flow passes through a flow restriction. For an engine cylinder, the reference flow area can be the valve seat area for the intake or exhaust valve.

Due to the friction, surface tension, and other non-ideal flow effects, only part of the reference flow area is used to carry the flow. Therefore, the value of a discharge coefficient is always less than unity. In some references, the discharge coefficient is defined as the ratio of actual mass flow rate to theoretical mass flow rate. The discharge coefficients are typically determined by experiments.

Discharge coefficients of intake and exhaust valves for a direct injection diesel engine were based on literature values (Abdul, Semin, and Bakar, 2007), modified based on the YANMAR engine valve dimensions.

The total injected fuel mass per 4-stroke cycle were determined by a graduated glass cylinder with a metered nozzle.

HC, CO, and CO_2 emissions data were measured by a Horiba MEXA-554JU exhaust analyzer. A Horiba MEXA-720 NO_x analyzer, which can measure the NO_x concentrations and air-to-fuel ratios, has also been utilized.

11.3.3 Emissions estimates and measurements using No. 2 diesel and soy biodiesel

In each emission test, an in-cylinder pressure profile was measured and used for combustion model calibration to assure a correct burn rate profile was predicted and the exhaust emissions prediction was based on a burn rate profile which closely resembled the one measured in the test. The measured in-cylinder pressure profiles for the No. 2 diesel fuel at an engine speed of 2200 and 2600 rpm at engine loads of 2.5, 5.0, 7.5 and 10 Nm are plotted in Figure 11.15 and 11.16.

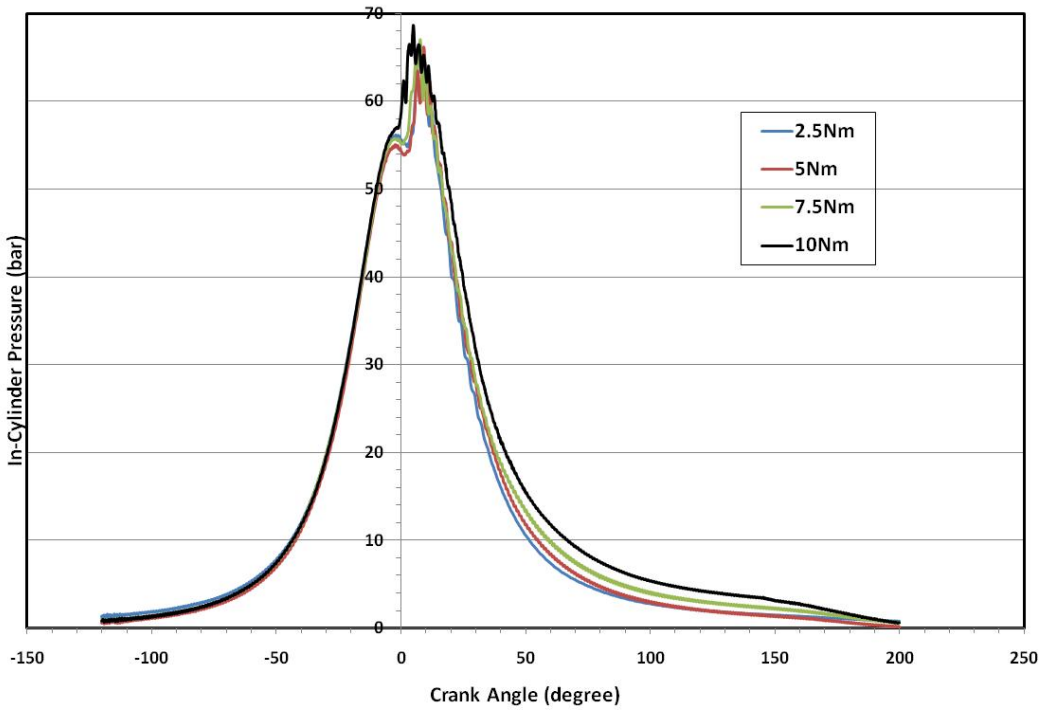

Figure 11.15. Measured in-cylinder pressure profiles at engine speed of 2200 rpm under four different engine loads (No. 2 diesel fuel)

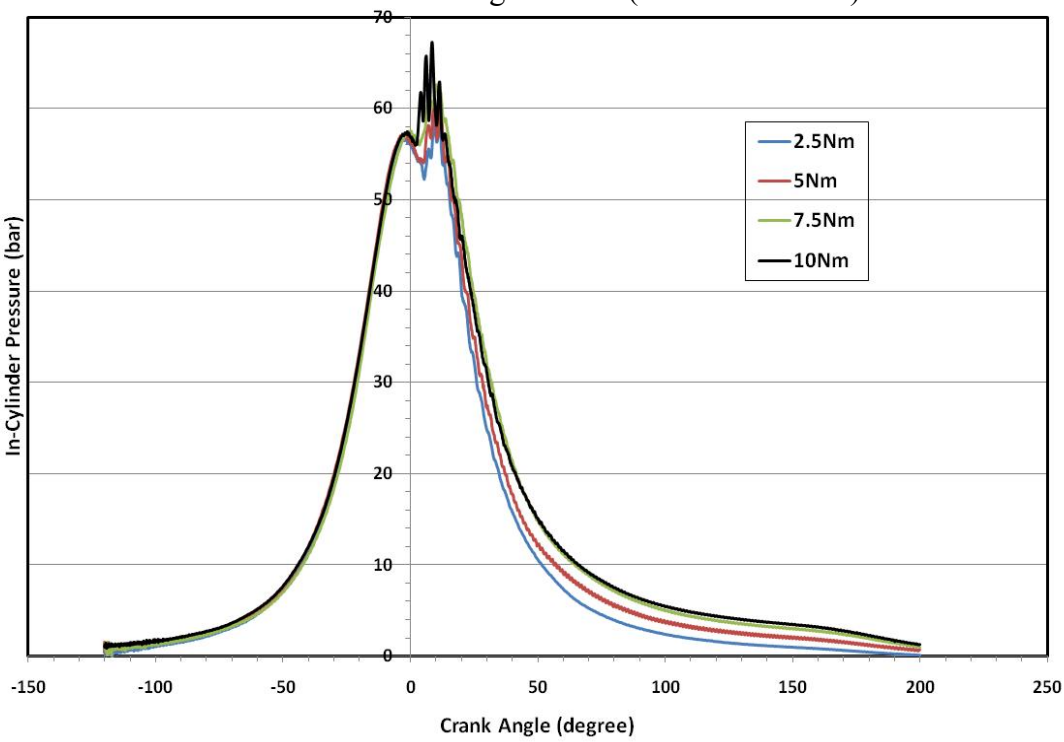

Figure 11.16. Measured in-cylinder pressure profiles at engine speed of 2600 rpm under four different engine loads (No. 2 diesel fuel)

The data show some irregularities/fluctuations especially after the initial pressure peak. Instead of a smooth and steady drop in pressure, oscillations were noticed and these eventually decayed over a couple of crank angle degrees. This trend could be attributed mainly to engine operation, with emphasis on the injector nozzle, as the cylinder pressure profile was smooth as expected (an indication that the combustion process in the cylinder was normal). While the nozzle is supposed to inject fuel once, the profile shows numerous smaller injection events took place rapidly after the first injection, thus resulting in the pressure fluctuations noticed in the profiles. This had an overall effect on the outputs from the CalcGraf calculations, even though the expected basic pressure profile was still evident. These testing results are displayed in Task 3 Appendix, Figures OO-DDD.

Emissions measurements for the No. 2 diesel were taken simultaneously as pressure data for the various engine speed-torque combinations and the data is presented in Table 11.56. A general trend observed in this set of data was the increase in the emissions as engine speed and load (i.e. torque) increased. Also evident is the air-fuel ratio which decreases with increasing load as expected. Finally, the injected mass of fuel per cycle is observed to increase with increasing engine speed and load.

ENGINE SPEED (rpm)	TORQUE (Nm)	NOx (ppm)	CO (%vol)	HC (ppm)	CO_2 (%vol)	A/F	O_2 (%vol)	Lambda	Injected fuel mass (mg/cycle)
2200	2.5	92	0.03	20	2.64	95.7	17.64	6.57	6.327
	5	104	0.04	22	3.66	67.6	16.35	4.62	9.259
	7.5	119	0.07	24	4.88	47.2	14.16	3.22	12.757
	10	150	0.63	29	7.36	28.3	9.83	1.95	19.369

ENGINE SPEED (rpm)	TORQUE (Nm)	NOx (ppm)	CO (%vol)	HC (ppm)	CO_2 (%vol)	A/F	O_2 (%vol)	Lambda	Injected fuel mass (mg/cycle)
2600	2.5	67	0.04	24	2.62	105.2	17.85	7.25	6.476
	5	99	0.05	24	4.16	59.8	15.5	4.23	9.266
	7.5	129	0.11	24	6.1	42.9	13.5	2.93	13.274
	10	146	0.38	25	9.26	28.1	9.78	1.93	19.445

Table 11.56. Emissions data for engine speeds of 2200 rpm and 2600 rpm with torque varied between 2.5 Nm and 10 Nm (No. 2 diesel)

After the No. 2 diesel tests, similar combustion emission tests were run with 100% pure soybean biodiesel (B100). The injection line pressures show slight variation in the pressure profiles, but a similar profile is seen for both fuels. On the other hand, for certain engine speed/load combinations, the emissions data showed a large reduction in hydrocarbons and considerable reduction in other products. Also noteworthy is the low fuel economy of the B100 as seen in the injected mass of fuel per cycle.

For the B100 soybean biodiesel emission tests, the measured in-cylinder pressure profiles, fuel injector pressure profiles, fuel velocities at fuel injector nozzle chamber entry, fuel injector sac pressure profiles, fuel injector nozzle needle lift profiles, and fuel injection rate profiles under engine loads of 2.5/5/7.5/10 Nm are provided in Task 3 Appendix, Figures EEE-MMM for the engine speed of 2200 rpm and Figures NNN-VVV for the engine speed of 2600 rpm. Table 11.57 show the emission test data measured for the B100 soybean biodiesel fuel.

ENGINE SPEED (rpm)	TORQUE (Nm)	NOx (ppm)	CO (%vol)	HC (ppm)	CO_2 (%vol)	A/F	O_2 (%vol)	Lambda	Injected fuel mass (mg/cycle)
2200	2.5	75	0.04	18	2.64	93.7	17.53	6.52	10.00
	5	96	0.04	19	3.66	70.1	16.21	4.85	10.67
	7.5	113	0.07	19	4.98	51.2	14.74	3.63	15.00
	10	128	0.26	21	6.78	34.2	12.06	2.45	22.80

ENGINE SPEED (rpm)	TORQUE (Nm)	NOx (ppm)	CO (%vol)	HC (ppm)	CO_2 (%vol)	A/F	O_2 (%vol)	Lambda	Injected fuel mass (mg/cycle)
2600	2.5	71	0.11	9	3.5	91.3	17.59	6.39	10.23
	5	84	0.12	10	4.02	70.1	16.25	4.84	11.28
	7.5	99	0.16	24	6.06	43.2	13.6	2.96	15.40
	10	122	0.38	25	8.22	32.95	11.2	2.23	23.10

Table 11.57. Emissions data for engine speeds of 2200 rpm and 2600 rpm with torque varied between 2.5 Nm and 10 Nm (B100 Soy Biodiesel)

Before running the GT-Power simulations, data output was examined and some adjustments were made. It was observed that the fuel injection quantities (per cycle) obtained by Concerto's integration of fuel injection profiles were appreciably higher compared to those separately measured by a graduated cylinder, for a single emission test. The differences of fuel injection quantities determined by these two measuring methods are in a range of 17% to 80% for the No. 2 diesel and 22% to 75% for the B100 soybean biodiesel. Since the fuel injector sac pressure profile obtained from Concerto was an input to the GT-Power model, the Concerto calculated values for injected fuel mass were used for simulation purposes.

To assure correct burn rate profiles are predicted in combustion simulations and exhaust emission predictions are based on burn rate profiles which closely resemble those measured in the emission tests, the simulation-predicted cylinder pressure profiles are compared with those measured in the emission tests at various engine speeds and engine loads. Plots comparing the simulation to physical test in-cylinder pressure measurements are provided in Task 3 Appendix, Figures WWW-DDDD. Plots have also been provided showing the cylinder temperature profiles and heat release rate profiles predicted by GT-Power in Figures EEEE-JJJJ.

For the No. 2 diesel fuel, the test-measured and simulation-predicted combustion emission concentrations of NO_x, HC, CO, and CO_2 are summarized and compared in Tables 11.58 and 11.59. In these two tables, the A/F and Lambda stand for air-to-fuel ratio and excess air ratio, respectively.

Engine speed (rpm)	Torque (Nm)	NOx (ppm)	CO (ppm)	HC (ppm)	CO_2 (ppm)	A/F	O_2 (%vol)	Lambda	Injected fuel mass per cycle measured by graduated cylinder (mg)	Injected fuel mass per cycle-integrated from Concerto (mg)	Adjusted injected fuel mass per cycle-integrated from Concerto, used as simulation input (mg)
2200	2.5	92 (81)	300 (5030)	20 (96)	26400 (32985)	95.7	17.64	6.57	6.327	9.548	6.622
	5	104 (132)	400 (4842)	22 (70)	36600 (61610)	67.6	16.35	4.62	9.259	16.698	11.982
	7.5	119 (155)	700 (5747)	24 (51)	48800 (81534)	47.2	14.16	3.22	12.757	19.073	16.119
	10	150 (130)	6300 (7482)	29 (3)	73600 (105972)	28.3	9.83	1.95	19.369	24.158	21.42

Table 11.58. Comparison between test-measured and simulation-predicted emissions for No.2 diesel fuel at engine speed of 2200 rpm

(Note: emissions values included in parentheses are simulation-predicted results.)

Engine speed (rpm)	Torque (Nm)	NOx (ppm)	CO (ppm)	HC (ppm)	CO_2 (ppm)	A/F	O_2 (%vol)	Lambda	Injected fuel mass per cycle measured by graduated cylinder (mg)	Injected fuel mass per cycle-integrated from Concerto (mg)	Adjusted injected fuel mass per cycle-integrated from Concerto, used as simulation input (mg)
2600	2.5	67 (74)	400 (10681)	24 (287)	26200 (32725)	105	17.85	7.25	6.476	10.263	7.774
	5	99 (100)	500 (9951)	24 (192)	41600 (54304)	59.8	15.5	4.23	9.266	16.584	11.528
	7.5	129 (116)	1100 (7840)	24 (46)	61000 (95367)	42.9	13.5	2.93	13.274	21.932	18.936
	10	146 (120)	3800 (10824)	25 (40)	92600 (100302)	28.1	9.78	1.93	19.445	22.807	20.557

Table 11.59. Comparison between test-measured and simulation-predicted emissions for No.2 diesel fuel at engine speed of 2600 rpm

(Note: emissions values included in parentheses are simulation-predicted results.)

Combustion emission simulations and tests were also carried out by using B100 soybean biodiesel fuel. Plots comparing the simulation predicted and test measured in-cylinder pressure readings for B100 soy biodiesel at engine speeds of 2200/2600 rpm and engine loads of 2.5/5.0/7.5/10.0 Nm are provided in Task 3 Appendix, Figures KKKK-RRRR. The predicted and measured in-cylinder pressure profiles agree very well under most of the test conditions, except the case with an engine speed-load combination of 2200 rpm and 10 Nm (shown in Figure RRRR). Figures SSSS-XXXX show the simulation-predicted profiles of cylinder temperature, apparent heat release rate, and NOx concentration, resulted from B100 soybean biodiesel combustion in the YANMAR engine under the described engine speeds and engine loads.

The test-measured and simulation-predicted combustion emission concentrations of NO_x, HC, CO, and CO_2 for B100 Soy Biodiesel are summarized and compared in Tables 11.60 and 11.61. In these two tables, the A/F and Lambda stand for air-to-fuel ratio and excess air ratio, respectively.

Engine speed (rpm)	Torque (Nm)	NOx (ppm)	CO (ppm)	HC (ppm)	CO_2 (ppm)	A/F	O_2 (%vol)	Lambda	Injected fuel mass per cycle measured by graduated cylinder (mg)	Injected fuel mass per cycle-integrated from Concerto (mg)	Adjusted injected fuel mass per cycle-integrated from Concerto, used as simulation input (mg)
2200	2.5	75 (96)	400 (1619)	18 (18)	26400 (39900)	93.7	17.5	6.52	10.00	12.175	8.027
	5	96 (114)	400 (3924)	19 (23)	36600 (66432)	70.1	16.2	4.85	10.67	17.994	14.335
	7.5	113 (68)	700 (841)	19 (2)	49800 (81652)	51.2	14.7	3.63	15.00	20.448	17.059
	10	128 (41)	2600 (16797)	21 (22)	67800 (95287)	34.2	12.1	2.45	22.80	28.305	24.335

Table 11.60. Comparison between test-measured and simulation-predicted emissions for B100 soybean biodiesel fuel at engine speed of 2200 rpm
(Note: emissions values included in parentheses are simulation-predicted results.)

Engine speed (rpm)	Torque (Nm)	NOx (ppm)	CO (ppm)	HC (ppm)	CO_2 (ppm)	A/F	O_2 (%vol)	Lambda	Injected fuel mass per cycle measured by graduated cylinder (mg)	Injected fuel mass per cycle-integrated from Concerto (mg)	Adjusted injected fuel mass per cycle-integrated from Concerto, used as simulation input (mg)
2600	2.5	71 (89)	1100 (4915)	9 (70)	35000 (44966)	91.3	17.6	6.39	10.23	13.779	9.696
	5	84 (92)	1200 (3786)	10 (48)	40200 (65583)	70.1	16.3	4.84	11.28	18.835	13.809
	7.5	99 (42)	1600 (5320)	24 (7)	60600 (99746)	43.2	13.6	2.96	15.40	26.996	21.793
	10	122 (30)	3800 (25523)	25 (40)	82200 (105444)	33	11.2	2.23	23.10	32.068	28.333

Table 11.61. Comparison between test-measured and simulation-predicted emissions for B100 soybean biodiesel fuel at engine speed of 2600 rpm
(Note: emissions values included in parentheses are simulation-predicted results.)

Comparison between the simulation-predicted and test-measured emissions data shows relatively good agreement for the NO_x emissions, but much poorer agreement for CO and hydrocarbon

emissions. These better results for NOx emission estimates, as compared to CO and hydrocarbon emission estimates, may be attributed to the fact that the predictive model in GT-Power, direct-injection jet (DIJet) modeling, was primarily developed for the purpose of predicting burn rate and NO_x emissions. In this simulation approach, the NO_x emissions are predicted using Extended Zeldovich mechanism, while the rest of emissions are primarily calculated using equilibrium chemistry. Based on these results, the engine simulations of biofuel emissions will be interpreted only for NOx emissions.

11.3.4 NOx emissions estimates for biodiesels

As compared to the conventional No. 2 diesel fuel, biodiesel fuels have lower heating values, higher viscosities, higher fuel densities, and contain approximately 10% oxygen. These differences in properties could potentially have an impact on the quantity of fuel injection and the combustion properties and emissions of the fuel.

For diesel engine combustion simulations, many physical and thermodynamic properties of the diesel or biodiesel fuels are required in the GT-Power DIJet models. The required liquid and vapor properties are listed as follows:

- Liquid: heat of vaporization, density, enthalpy of liquid, temperature-dependent kinematic viscosities, temperature-dependent thermal conductivities
- Vapor: lower heating value, critical temperature, critical pressure, enthalpy of vapor, temperature-dependent kinematic viscosities, temperature-dependent thermal conductivities, carbon atoms per molecule, hydrogen atoms per molecule, oxygen atoms per molecule, nitrogen atoms per molecule

For the emerging fuels considered in this work, many of these fuel properties either have never been collected or are not available in published literature. A consolidated table of fuel properties collected from literature and the GT-Power fuel libraries for the No. 2 diesel fuel, soybean fuels, and cottonseed fuels are included in Tables 11.62 and 11.63.

State	Properties	No. 2 Diesel[5,7,15]	No. 2 Diesel (GT-Power Fuel Library)	Soybean Methylester[5,7]	Cottonseed Methylester[7,13]	Cottonseed Oil[4]
Liquid	Heat of Vaporization (kJ/kg)	375	250			
Liquid	Density (kg/m^3)	850	830	885.3 (average)	885	884.2 (at 25°C)
Liquid	Enthalpy of Liquid (kJ/kg)		Calculated			
Liquid	Kinematic Viscosity at 40°C (mm^2/s)	2.6	Temperature Dependent	4.08 (average)	4	33.5
Liquid	Thermal Conductivity of Liquid (W/(mK))		Temperature Dependent			
vapor	Lower Heating Value (kJ/kg)	43357	43250	37042 (average)	37500	36800
vapor	Critical Temperature (K)		569.4	784.62 (calculated)	779.72 (calculated)	780.8 (calculated)
vapor	Critical Pressure (bar)		24.6	12.07 (calculated)	12.15 (calculated)	12.8 (calculated)
vapor	Enthalpy of Vapor (kJ/kg)		Calculated			
vapor	Viscosity of Vapor		Temperature Dependent			
vapor	Thermal Conductivity of Vapor (W/(mK))		Temperature Dependent			
vapor	Number of Carbon Atoms in Each Molecule	12	13.5	19		
vapor	Number of Hydrogen Atoms in Each Molecule	26	23.6	35		
vapor	Number of Oxygen Atoms in Each Molecule	0	0	2		

Table 11.62. Consolidated Fuel Property Data

State	Enthalpy Constant	No. 2 Diesel	Soybean Methylester	Cottonseed Methylester
Liquid	a_1	2050		
Liquid	a_2	0		
Liquid	a_3	0		
vapor	a_1	1634.3		
vapor	a_2	1.8191		
vapor	a_3	0		
vapor	a_4	0		
vapor	a_5	0		

Table 11.63. Enthalpy constants for liquid and vapor fuels from GT-Power fuel library

To estimate properties for which literature data were not available, the computer program "BDProp 1.0", developed by Dr. Wenqiao Yuan of Kansas State University, was used. The pure biodiesel (B100) fuel properties calculated by the BDProp code include critical properties, density, vapor pressure, enthalpy, heat of vaporization, surface tension, viscosity, and molecular chemical structure. Most of these fuel properties calculated by BDProp are only for "liquid" state. The predicted properties of selected biodiesels are included in Table 11.64. The predicted normal boiling temperatures, molecular structures, and molecular weights are included in Table 11.65. Soybean, cottonseed, and algae methyl esters are abbreviated as SME, CME, and AME, respectively. The numerical values appended to the abbrieviations of biodiesel identify associated references listed in this report.

	SME-30	**SME-31**	SME-33	**CME-31**	CME-32	CME-39	AME-40	AME-41	**AME-42**	No. 2 Diesel
Critical Temperature (K)	783.83	**784.67**	781.24	**779.72**	779.62	781.51	768.59	764.36	**773.07**	569.4
Critical Pressure (bar)	12.02	**12.07**	12.04	**12.15**	12.20	12.18	11.87	12.44	**11.84**	24.6
Critical Volume (mm^3/mil)	1084.16	**1081.52**	1079.81	**1070.61**	1066.52	1070.14	1078.78	1033.83	**1086.18**	

Table 11.64. Critical properties of soybean, cottonseed, algae biodiesels (calculated by BDProp) and No. 2 diesel (Gamma Technologies, 2006).

	SME-30	**SME-31**	SME-33
Normal Boiling Temperature (K)	627.074	**627.396**	624.1
Molecular Structure	$C_{18.7946}H_{34.6256}O_2$	$\mathbf{C_{18.77}H_{34.4441}O_2}$	$C_{18.6493}H_{34.7109}O_2$
Molecular Weight (g/mol)	292.161	**291.684**	290.503

	CME-31	CME-32	CME-39
Normal Boiling Temperature (K)	**621.045**	620.436	622.7
Molecular Structure	$\mathbf{C_{18.4732}H_{34.432}O_2}$	$C_{18.3976}H_{34.2917}O_2$	$C_{18.4934}H_{34.3116}O_2$
Molecular Weight (g/mol)	**288.11**	287.063	288.232

	AME-40	AME-41	**AME-42**
Normal Boiling Temperature (K)	627.787	606.011	**619.68**
Molecular Structure	$C_{18.3922}H_{35.5701}O_2$	$C_{17.6236}H_{33.873}O_2$	$\mathbf{C_{18.6514}H_{35.351}O_2}$
Molecular Weight (g/mol)	288.277	277.356	**291.168**

Table 11.65. Normal boiling temperatures, molecular structures, and molecular weights of soybean, cottonseed, algae biodiesels (calculated by BDProp)

The fuel thermal conductivity, which impacts thermal conduction in the fuel spray, required by GT-Power modeling, cannot be calculated by BDProp. The Sastri method (Reid, Prausnitz, and Poling, 1987) was used to estimate thermal conductivities.

Sastri recommends

$$\lambda_L = \lambda_b a^m$$

where

$$m = 1 - \left(\frac{1 - T_r}{1 - T_{br}}\right)^n$$

λ_L is the thermal conductivity (W/m-K) of the liquid, λ_b is the thermal conductivity at the normal boiling point and is determined by group contributions, T_r is the reduced temperature, T_{br} is the reduced temperature at the boiling point. For alcohols and phenols, a = 0.856 and n = 1.23. For other compounds, a = 0.16 and n = 0.2. Sastri reported an average deviation of 8% for 186 points that were tested.

Plots of the predicted temperature-dependent densities, heat of vaporization, dynamic viscosities, thermal conductivities, enthalpies, vapor pressures, and surface tensions are provided in Task 3 Appendix, Figures A-BB. Some of these fuel properties were also available for No. 2 diesel. Where applicable, No. 2 diesel property values have been included on the biodiesel plots for comparison against the biodiesel properties. The fatty acid compositions chosen for calculating these predictions are highlighted in Task 3 Appendix, Tables A-E.

These plots (Figures A-BB) display minimal difference in the predicted fuel property values among the selected biodiesel groups (excluding the algae biodiesels AME-40, AME-41, and AME-42). Therefore, only one biodiesel out of each biodiesel fuel group was analyzed in the GT-Power combustion simulation. The selected biodiesels are SME-31 for the soybean biodiesel group, CME-31 for the cottonseed biodiesel group, and AME-42 for the algae biodiesel group.

During the course of the property estimation, the following difficulties were encountered:

1. Erroneous results of critical pressures and enthalpies were calculated by BDProp when certain biodiesel fatty acid composition profiles, such as those of algae biofuels, were used.
2. Biodiesel enthalpy constants required by the GT-Power cannot be determined by the BDProp-predicted enthalpies.
3. BDProp-predicted biodiesel viscosities at a temperature of 40°C are approximately 35% lower than the measured biodiesel viscosities reported in various publications.

Certain biodiesel fatty acids were not defined in the BDProp code and certain fatty acids, such as C14:1, caused BDProp computational errors. Those fatty acids not represented in the BDProp program were generally uncommon acids and only contributed relatively small percentages of the overall biodiesel fatty acids. These uncommon fatty acids were redistributed to those fatty acids represented within BDProp.

Since the BDProp-predicted biodiesel properties were for liquid phase properties only, temperature-dependent viscosity and thermal conductivity data for the vapor of methyl oleate (C18:1) was used to estimate vapor properties (MacDonald, 2005). As shown in Table 11.66 methyl oleate is a significant component in soybean, cottonseed, and algae biodiesel fuels.

Fatty Acid (Trivial Name)	Fatty Acid (Systematic Name)	Structure	Soybean	Cottonseed	Algae
Lauric	Dodecanoic	C12:0			
Myristic	Tetradecanoic	C14:0	0.2	0.8	1.31
Palmitic	Hexadecanoic	C16:0	10.2	22.9	12.94
Palmitoleic	9-Hexadecenoic	C16:1			
Margaric	Heptadecanoic	C17:0			0.89
Stearic	Octadecanoic	C18:0	4.6	3.1	2.76
Oleic	9-Octadecenoic	C18:1	22.2	18.5	60.84
Linoleic	9,12-Octadecadienoic	C18:2	54.6	54.2	17.28
Linolenic	9,12,15-Octadecatrienoic	C18:3	8.2	0.5	
	10-Nonadecenoic	C19:1			0.36
Arachidic	Eicosanoic	C20:0			0.35
Gadoleic	9-Eicosenoic	C20:1			0.42
Behenic	Docosanoic	C22:0			
Lignoceric	Tetracosanoic	C24:0			
Sum			100	100	97.15

Table 11.66: Fatty acid profiles of soybean, cottonseed, and algae biodiesel fuels

The temperature dependent dynamic viscosities and thermal conductivities of the methyl oleate vapor (or biodiesel vapors) are shown in Figures 11.17 and 11.18.

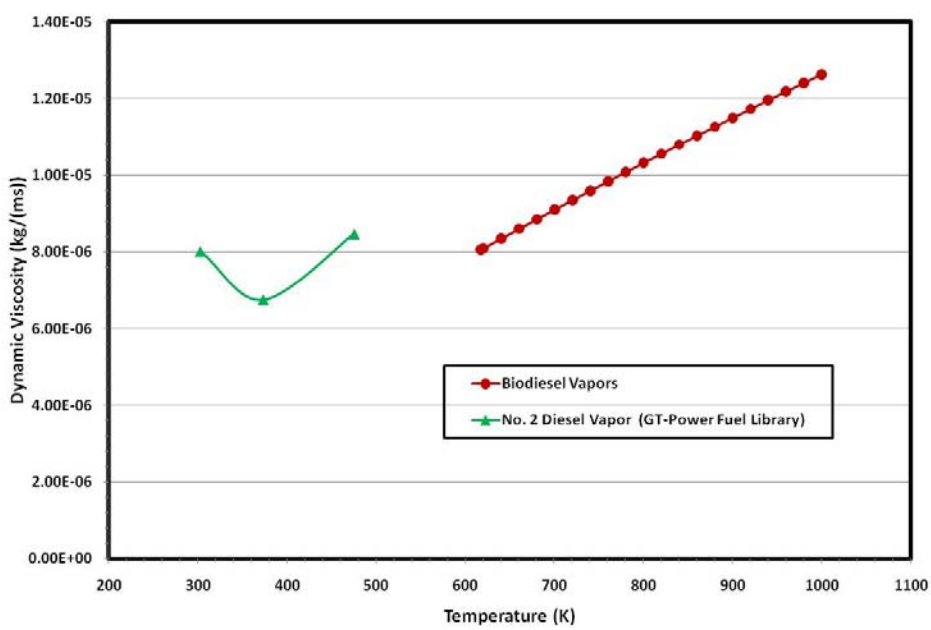

Figure 11.17: Temperature-dependent No. 2 diesel and biodiesel vapor dynamic viscosities

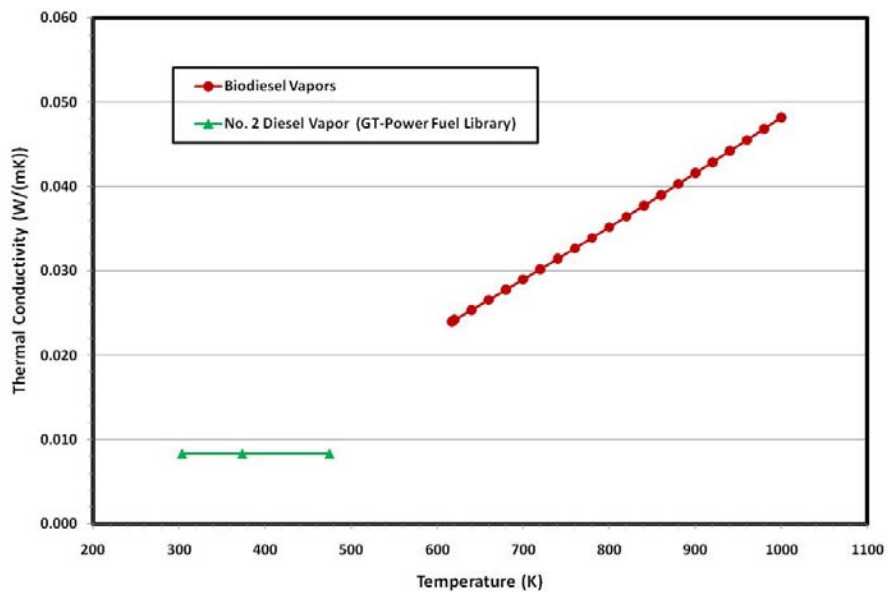

Figure 11.18: Temperature-dependent No. 2 diesel and biodiesel vapor thermal conductivities

Enthalpy constants (liquid and vapor phase) are also required by the GT-Power combustion simulation but cannot be calculated by the BDProp computer program.

The enthalpy constants of a diesel or biodiesel fuel required by the GT-Power are defined by:

- For liquid:

$$h - h_{ref} = a_1(T - T_{ref}) + a_2(T - T_{ref})^2 + a_3(T - T_{ref})^3$$

- For vapor:

$$h - h_{ref} = a_1(T - T_{ref}) + a_2(T - T_{ref})^2 + a_3(T - T_{ref})^3 + a_4(T - T_{ref})^4 + a_5(T - T_{ref})^5$$

These properties were based on data for C14:0, C16:0, C18:0, C18:1, and C18:2 methyl esters; assumed compositions for the biofuels are listed in Table 11.67. The approach taken was to estimate heat capacities, and temperature dependent enthalpies for the fuels based on the compositions in Table 11.67, then to fit these results to the parametric forms required by GT-Power.

Fatty Acid (Trivial Name)	Structure	Soybean	Cottonseed	Algae
Myristic	C14:0	0.2	0.8	1.3484
Palmitic	C16:0	10.2	22.9	13.3196
Stearic	C18:0	4.6	3.1	3.7571
Oleic	C18:1	22.2	18.5	62.6248
Linoleic	C18:2	62.8	54.7	18.9501
Sum		100	100	100

Table 11.67. Adjusted fatty acid profiles of soybean, cottonseed, and algae biodiesel fuels

The enthalpy constants of a diesel or biodiesel fuel required by the GT-Power are defined by:

The Rowlinson-Bondi method (Reid, Prausnitz, and Poling, 1987), can be used to estimate the liquid heat capacity of nonpolar or slightly polar compounds. This method is represented by the following equation:

$$\frac{C_{pL} - C_p^o}{R} = 1.45 + 0.45(1 - T_r)^{-1} + 0.25\omega[17.11 + 25.2(1 - T_r)^{1/3} T_r^{-1} + 1.742(1 - T_r)^{-1}]$$

Where

C_{pL} = heat capacity of liquid at constant pressure (J/mol-K)
C_p^o = heat capacity of liquid at a reference state (J/mol-K)
R = Gas constant (8.314 J/mol-K)
T_r = reduced temperature
ω= Pitzer acentric factor

The Pitzer acentric factor can be calculated using the following correlations:

$$\omega = \frac{\alpha}{\beta}$$

$$\alpha = -\ln(P_c) - 5.97214 + 6.09648\theta^{-1} + 1.28862\ln(\theta) - 0.169347\theta^6$$

$$\beta = 15.2518 - 15.6875\theta^{-1} - 13.4721\ln(\theta) + 0.43577\theta^6$$

$$\theta = \frac{T_b}{T_c}$$

Where

P_c = critical pressure (atmospheres)
T_b = normal boiling point (K)
T_c = critical temperature (K)

The published normal boiling points (McCormick et al, 2006) and BDProp-calculated critical pressures and critical temperatures of the common pure methyl esters found in biodiesel fuels are included in Table 11.68.

Compositions	Normal Boiling Point (K)	Critical Pressure (bar)	Critical Temperature (K)
C14:0	568	14.0246	730.433
C16:0	611	12.5785	754.031
C18:0	625	11.3499	774.134
C18:1	622	11.5675	772.283
C18:2	639	12.1736	795.269

Table 11.68. Published normal boiling points [51] and calculated critical-point properties of common pure methyl esters found in biodiesel fuels

Chueh-Swanson method (Reid, Prausnitz, and Poling, 1987), is a group contribution approach for estimating the liquid heat capacity at a room temperature of 293 K. The group contribution method assumes that various groups in a molecule contribute a definite value to the total molar heat capacity that is independent of other groups present. Group contributions related to the biodiesel fuels are shown in Table 11.69. The chemical structures of common biodiesel fatty acids (Canakci and Sanli, 2008) are shown in Table 11.70.

Group	Value (J/mol-K)
$-CH_3$	36.8
$-CH_2-$	30.4
=CH-	21.3
-COO-	60.7

Table 11.69. Group contributions for molar liquid heat capacity at 293 K for Chueh-Swanson method [47]

Fatty Acid	Molecular Formula	Chemical Structure
Myristic (14:0)	$C_{14}H_{28}O_2$	$CH_3(CH_2)_{12}COOH$
Palmitic (16:0)	$C_{16}H_{32}O_2$	$CH_3(CH_2)_{14}COOH$
Stearic (18:0)	$C_{18}H_{36}O_2$	$CH_3(CH_2)_{16}COOH$
Oleic (18:1)	$C_{18}H_{34}O_2$	$CH_3(CH_2)_7CH{=}CH(CH_2)_7COOH$
Linoleic (18:2)	$C_{18}H_{32}O_2$	$CH_3(CH_2)_4CH{=}CHCH_2CH{=}CH(CH_2)_7COOH$

Table 11.70. Chemical structures of common biodiesel fatty acids [49]

Based on these methods, the liquid enthalpy as a function of temperature was based on a mass average of the composition of the biofuels.

$$h - h_{ref} = \int_{Tref}^{T} C_p dT$$

Where

h = enthalpy (J/kg)
h_{ref} = enthalpy at reference temperature
T_{ref} = reference temperature

The calculated liquid heat capacities and liquid enthalpies of biodiesels are provided in Task 3 Appendix, Figures CC-HH.

The vapor phase heat capacities were estimated using the Lee-Kesler method [47]. This method is expressed by the following equation:

$$C_p - C_p^o = \Delta C_p = (\Delta C_p)^{(0)} + \omega(\Delta C_p)^{(1)}$$

Where

C_p = heat capacity of vapor at constant pressure (J/mol-K)
C_p^o = heat capacity of vapor at a reference state (J/mol-K)
$(\Delta C_p)^{(0)}$ = simple fluid contribution as a function of reduced temperature and reduced pressure
$(\Delta C_p)^{(1)}$ = deviation function as a function of reduced temperature and reduced pressure
ω = Pitzer acentric factor

The Joback method [47] uses group contributions to relate C_p^o to temperature. This method is represented by the following equation:

$$C_p^o = \left(\sum_j n_j \Delta_a - 37.93\right) + \left(\sum_j n_j \Delta_b + 0.210\right)T + \left(\sum_j n_j \Delta_c - 3.91x10^{-4}\right)T^2 + \left(\sum_j n_j \Delta_d + 2.06x10^{-7}\right)T^3$$

Where

n_j = number of groups of the "jth" type
Δ_a, Δ_b, Δ_c, Δ_d = group contributions
T = temperature (K)

The group contributions related to the biodiesel fuels are shown in Table 11.71.

Group	Δ_a (J/mol-K)	Δ_b (J/mol-K)	Δ_C (J/mol-K)	Δ_d (J/mol-K)
CH_3	1.95E+01	-8.08E-03	1.53E-04	-9.67E-08
CH_2	-9.09E-01	9.50E-02	-5.44E-05	1.19E-08
CH	-8	1.05E-01	-9.63E-05	3.56E-08
COO	2.45E+01	4.02E-02	4.02E-05	-4.52E-08

Table 11.71. Joback Group Contributions for Ideal-Gas Properties

Similar to the calculation of the liquid enthalpy, the biodiesel vapor heat capacity can also be integrated with respect to the temperature to get the vapor enthalpy. The calculated vapor heat capacities and enthalpies of biodiesels are provided in Task 3 Appendix, Figures II-NN.

The parameters required by GT-Power were calculated using these estimates of liquid and vapor enthalpies, as a function of temperature. The results are shown in Table 11.72.

State	Enthalpy Constant	No. 2 Diesel (GT-Power Fuel Library)	Soybean Methylester (SME-31)	Cottonseed Methylester (CME-31)	Algae Methylester (AME-42)
Liquid	a_1	2050	2126.9	2113.9	2113
Liquid	a_2	0	-0.814	-0.8437	-0.8018
Liquid	a_3	0	0	0	0
Vapor	a_1	1634.3	1366.6	1356.7	1585.2
Vapor	a_2	1.8191	0.0684	-0.0123	1.1977
Vapor	a_3	0	0	0	0
Vapor	a_4	0	0	0	0
Vapor	a5	0	0	0	0

Table 11.72. Enthalpy constants for liquid and vapor fuels required for GT-Power combustion simulations

A summary of the fuel properties used in the simulations is provided in Table 11.73.

State	Properties	No. 2 Diesel (GT-Power Fuel Library)	Soybean Methylester (SME-31)	Cottonseed Methylester (CME-31)	Algae Methylester (AME-42)
Liquid	Heat of Vaporization at 25°C (kJ/kg)	250	356.24	354.53	351.63
Liquid	Density at 25°C (kg/m^3)	830	881.38	880.09	860.84
Liquid	Enthalpy of Liquid (kJ/kg)	GT-Power Fuel Library	Shown in Table 34	Shown in Table 34	Shown in Table 34
Liquid	Kinematic Viscosity of Liquid (mm^2/s)	GT-Power Fuel Library	Shown in Figure 25	Shown in Figure 25	Shown in Figure 25
Liquid	Thermal Conductivity of Liquid (W/(mK))	GT-Power Fuel Library	Shown in Figure 29	Shown in Figure 29	Shown in Figure 29
Vapor	Lower Heating Value (kJ/kg)	43250	37042	37500	37620*
Vapor	Critical Temperature (K)	569.4	784.67	779.72	773.07
Vapor	Critical Pressure (bar)	24.6	12.07	12.15	11.84
Vapor	Enthalpy of Vapor (kJ/kg)	GT-Power Fuel Library	Shown in Table 34	Shown in Table 34	Shown in Table 34
Vapor	Kinematic Viscosity of Vapor (mm^2/s)	GT-Power Fuel Library	Shown in Figure 42	Shown in Figure 42	Shown in Figure 42
Vapor	Thermal Conductivity of Vapor (W/(mK))	GT-Power Fuel Library	Shown in Figure 43	Shown in Figure 43	Shown in Figure 43
Vapor	Number of Carbon Atoms in Each Molecule	13.5	18.77	18.4732	18.6514
Vapor	Number of Hydrogen Atoms in Each Molecule	23.6	34.4441	34.432	35.351
Vapor	Number of Oxygen Atoms in Each Molecule	0	2	2	2

Table 11.73. Diesel and biodiesel fuel properties required for GT-Power combustion simulations

GT-Power combustion simulations of the soybean, cottonseed, and algae methylester biodiesel fuels were performed using the fuel properties listed in the Tables 11.72 and 11.73 to predict the biodiesel combustion emissions. An engine speed of 2200 RPM and an injected fuel mass per

cycle of 9.7 mg, which were the testing parameters measured in the No. 2 diesel emission test reported previously, were used in these simulation analyses.

The fuel injector sac pressure profile was determined through multiple iterations such that the predicted engine torque matched the engine torque measured in physical testing. In the biodiesel combustion simulations, it was assumed that the fuel injector sac pressure profiles of the described biodiesel fuels are the same as that of the No. 2 diesel. The predicted engine torques and emission concentrations of the diesel and biodiesel fuels are included in Table 11.74.

Fuel	Engine Torque (N-m)	NOx (ppm)
No. 2 Diesel	4.47	153
Soybean Methylester	3.29	164
Cottonseed Methylester	3.42	177
Algae Methylester	3.49	183

Table 11.74. Predicted engine torques and combustion emissions

Based on the predicted emission concentrations shown in the Table 11.74 emission changes for 100% biodiesels (B100), as compared to the No. 2 diesel emissions, are included in Table 11.75.

Fuel	NOx (ppm)
Soybean Methylester	+7.2%
Cottonseed Methylester	+15.7%
Algae Methylester	+19.6%
Average	**+14.2%**

Table 11.75. Percent changes in B100 biodiesel (100% biodiesel) emissions as compared to No. 2 diesel emissions

A number of studies have examined the emission impacts of biodiesel in 4-stroke direct injection diesel engines and 2-stroke indirect injection engines. These studies have been reviewed by the U.S. Environmental Protection Agency (EPA) [50] with statistical analysis. Figure 11.19, taken

from the EPA and the U.S. National Renewable Energy Laboratory (NREL) (McCormick et al, 2006), shows the overall trends with biodiesel blending level for four regulated pollutants of NO_x, PM, CO, and HC. Referring to Figure 11.19, for a B100 biodiesel, the reported percent changes in pollutant emissions are approximately +10% for NO_x, -48.5% for CO, and -67% for HC.

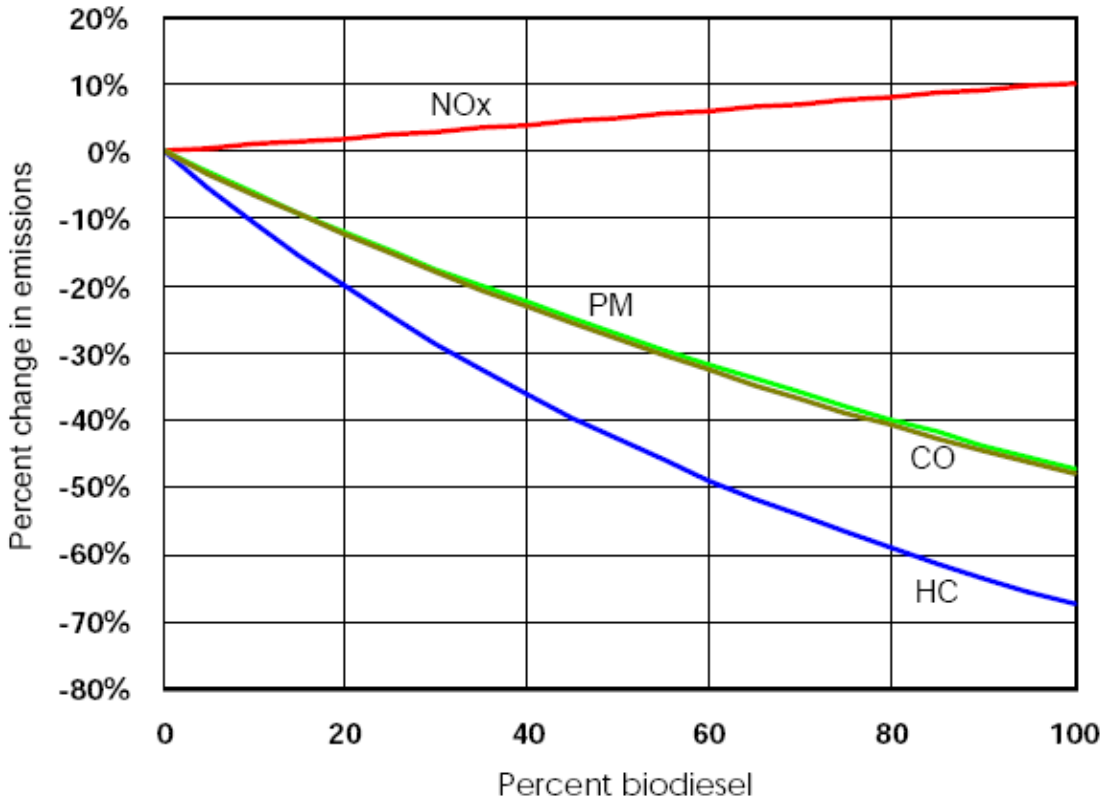

Figure 11.19: Trends in percentage change in pollutant emissions with biodiesel content as estimated from published engine dynamometer data in the EPA study (EPA, 2002; McCormick et al, 2006)

11.3.5 Summary of predictive emission modeling

Overall, these results suggest that the emissions assumed for the biodiesel in the air quality modeling are reasonable, based on engine simulations, however, there may be significant variability in NOx emissions associated with alternative biodiesel feedstock sources. For engine simulations to provide additional insights, multiple difficulties will need to be overcome.

1. Fuel injection sac pressure profiles are critical to estimating emissions, but few measurements for this parameter exist.
2. Fuel property data are not readily available for emerging biodiesels, and fuel properties can have a significant impact of emission characteristics.

11.3 References

Abdul, Semin, and Bakar, 2007: Abdul, R., Semin, I., and Bakar, A.R., 2007. Valve Flow Discharge Coefficient Investigation for Intake and Exhaust Port of Four Stroke Diesel Engines. Journal of Engineering and Applied Science, Vol. 2 (12), pp. 1807-1811.

Austin Energy, 2008a: Planning for Austin's Future Energy Resources, City of Austin, 2008. Retrieved from http://www.austinenergy.com/About%20Us/Newsroom/Reports/taskForce/docFactSheet.pdf on December 30, 2009.

Austin Energy, 2008b: Austin Energy. Resources Guide, Planning for Austin's Future Energy Resources, City of Austin, 2008. Retrieved from http://www.austinsmartenergy.com/downloads/AustinEnergyResourceGuide.pdf on December 30, 2009.

Canakci and Sanli, 2008: Canakci, M. and Sanli, H., 2008. Biodiesel Production from Various Feedstocks and Their Effects on the Fuel Properties. Journal of Industrial Microbiology and Biotechnology, Vol. 35, pgs. 431-441.

Carter, 2009: Carter, W., April 30, 2009. Development of an Improved Chemical Speciation Database for Processing Emissions of Volatile Organic Compounds for Air Quality Models. Retrieved from http://www.engr.ucr.edu/~carter/emitdb/ on December 30, 2009.

Cooper and Arbrandt, 2004: Cooper C. and Arbrandt M., 2004. Annual Average vs Monthly Average Values for Selected Inputs to MOBILE6 – Effect on an Annual Emissions Inventory. Presented at the 97th Annual Meeting and Exhibition of the Air & Waste Management Association, Indianapolis, Indiana.

DOE, 2006: US Department of Energy, October 30 - November 1, 2006. Workshop on Basic Research Needs for Clean and Efficient Combustion of 21st Century Transportation Fuels. Office of Basic Energy Sciences: US Department of Energy

DOE, 2007: US Department of Energy, 2007. Energy Independence and Security Act of 2007. Federal Energy Management Program.

DOT, 2002: US Department of Transportation, 2002. Selected Measures For Identifying Peer States, Highway Statistics. Federal Highway Administration: US Department of Transportation. Retrieved from http://www.fhwa.dot.gov/policy/ohim/hs02/ps1.html on December 30, 2009.

EPA, 2002: US Environmental Protection Agency, 2002. A Comprehensive Analysis of Biodiesel Impacts on Exhaust Emissions, EPA420-P-02-001. Retrieved from http://www.biodiesel.org/resources/reportsdatabase/reports/gen/20021001_gen-323.pdf on December 30, 2009.

EPA, 2006: US Environmental Protection Agency, 2006. Inventory of U.S. Greenhouse Gas Emissions and Sinks: 1990–2004. Retrieved from http://www.epa.gov/climatechange/emissions/downloads06/06_Complete_Report.pdf on December 30, 2009.

EPA, 2008: US Environmental Protection Agency, 2008. Preliminary 2008 Ozone Season Data. Clean Air Markets Division: US Environmental Protection Agency.

EPA, 2009: US Environmental Protection Agency, 2009. Ground Level Ozone. Retrieved from http://www.epa.gov/air/ozonepollution on December 29, 2009.

Gamma Technologies, 2006: Gamma Technologies, 2006. Fuel Library of GT-Power (Version 6.2): A GT-SUITE Application for Engine Performance, Acoustics, and Control Simulation. Gamma Technologies.

Jacobson, 2007: Jacobson, M.Z., 2007. Effects of Ethanol (E85) versus Gasoline Vehicles on Cancer and Mortality in the United States. Environmental Science & Technology, Vol. 41 (11), pgs. 4150-4157.

Kintner-Meyer, Schneider, and Pratt, 2007: Kintner-Meyer M, Schneider, K., and Pratt, R., 2007. Impact Assessment of Plug-in Hybrid Vehicles on Electric Utilities and Regional US Power Grids. Part I: Technical Analysis. Pacific Northwest National Laboratory. Retrieved from http://energytech.pnl.gov/publications/pdf/PHEV_Feasibility_Analysis_Part1.pdf on December 30, 2009.

Knipping and Duvall, 2007a: Knipping, E., and Duvall, M., 2007. Environmental Assessment of Plug-In Electric Hybrid Vehicles Vol 1 Nationwide Greenhouse Gas Emissions. Electric Power Research Institute. Retrieved from http://my.epri.com/portal/server.pt?open=512&objID=243&PageID=223132&cached=true&mode=2 on December 30, 2009.

Knipping and Duvall, 2007b: Knipping, E., and Duvall, M., 2007. Environmental Assessment of Plug-In Electric Hybrid Vehicles Vol 2 United States Air Quality Analysis Based on AEO-2006 Assumptions for 2030. Electric Power Research Institute. Retrieved from http://my.epri.com/portal/server.pt?open=512&objID=243&PageID=223132&cached=true&mode=2 on December 30, 2009.

Lavigne and Powers, 2007: Lavigne, A., and Powers, S.E., 2007. Evaluating Fuel Ethanol Feedstocks from Energy Policy Perspectives: a Comparative Energy Assessment of Corn and Corn Stover. Energy Policy, Vol. 35, pgs. 5918-5930.

Lindhjem and Pollack, 2003: Lindhjem, C., and Pollack, A., 2003. Impact of Biodiesel Fuels on Air Quality and Human Health: Task 1 Report. National Renewable Energy Laboratory (NREL). Retrieved from http://www.nrel.gov/vehiclesandfuels/npbf/pdfs/33794.pdf on December 30, 2009.

MacDonald, 2005: MacDonald, T., 2005. Alcohol Fuel Flexibility-Progress and Prospects. Presented at Fifteenth International Symposium on Alcohol Fuels, San Diego, CA, Sept. 26-28, 2005.

McCormick et al, 2006: McCormick, R.L., Williams, A., Ireland, J., Brimhall, M., and Hayes, R.R., 2006. Effects of Biodiesel Blends on Vehicle Emissions, Milestone Report, NREL/MP-540-40554. Retrieved from http://www.nrel.gov/vehiclesandfuels/npbf/pdfs/40554.pdf on December 30, 2009.

McGaughey et al, 2004: McGaughey, G. R., N. R. Desai, D. T. Allen, R. L. Seila, W. A. Lonneman, M. P. Fraser, R. A. Harley, J. M. Ivy, and J. H. Price, 2004. Analysis of Motor Vehicle Emissions in a Houston Tunnel during the Texas Air Quality Study 2000. Atmospheric Environment, Vol. 38, pgs. 3363-3372.

Niemeier et al, 2006: Niemeier U., Granier C., Kornblueh L., Walters S., Brasseur G., 2006. Global Impact of Road Traffic on Atmospheric Chemical Composition and on Ozone Climate Forcing. Journal of Geophysical Research, Vol. 111, D09301, DOI 10.1029/2005JD006407.

Reid, Prausnitz, and Poling, 1987: Reid, R. C., Prausnitz, J. M., and Poling, B. E., 1987. The Properties of Gases & Liquids, 4th Edition, McCraw-Hill, New York, NY.

Sawyer, et al, 2000: Sawyer R.F., Harley, R.A., Cadle S.H., Norbeck J.M., Slott R., and Bravo, H.A., 2000. Mobile Sources Critical Review: 1998 NARSTO Assessment. Atmospheric Environment, Vol. 34, pgs. 2161–2181.

Seinfeld and Pandis, 1998: Seinfeld, J.H. and Pandis, S. N., 1998. Atmospheric Chemistry and Physics. New York: Wiley Interscience.

Sharp, 1999: Sharp C., 1999. Characterization of Biodiesel Exhaust Emissions for EPA 211. Southwest Research Institute. Retrieved from http://www.biodiesel.org/resources/reportsdatabase/reports/gen/19980101_gen-156.pdf on December 30, 2009.

Sheehan et al, 1998: Sheehan J, et al., 1998. Life Cycle Inventory of Biodiesel and Petroleum Diesel for Use in an Urban Bus, National Renewable Energy Laboratory, NREL/SR-580-24089. Retrieved from http://www.nrel.gov/docs/legosti/fy98/24089.pdf on August 2007.

Song et al, 2008: Song J., Webb A., Parmenter B., Allen D. and McDonald Buller, 2008. The Impacts of Urbanization on Emissions and Air Quality: Comparison of Four Visions of Austin, Texas. Environmental Science & Technology, Vol. 42, pgs. 7294–7300.

Takenaka et al, 2005: Takenaka, N., Kadowaki, T., Kawabata, Y., Lim, I. C., and Sim, C. M., 2005. Visualization of Cavitation Phenomena in a Diesel Engine Fuel Injection Nozzle

by Neutron Radiography. Nuclear Instruments and Methods in Physics Research, Section A 542, pp. 129-133.

Webb et al., 2008: Webb, A., Song, J., Allen, D., McDonald-Buller, E., Zhou, B., Gadda, S., Lemp, J., Tirumalachetty, S., Kockelman, K., and Parmenter, B., 2008, Predicting The Relative Impacts Of Urban Development Policies And On-Road Vehicle Technologies On Air Quality In The United States: Modeling And Analysis Of A Case Study In Austin, Texas, EPA STAR Grant, RD83183901, Final Report, December 18, 2008.

Chapter 11: Appendix

Figures developed during Engine Simulations

Figures A-BB: Predicted biodiesel temperature-dependent densities, heat of vaporization, dynamic viscosities, thermal conductivities, enthalpies, vapor pressures, and surface tensions

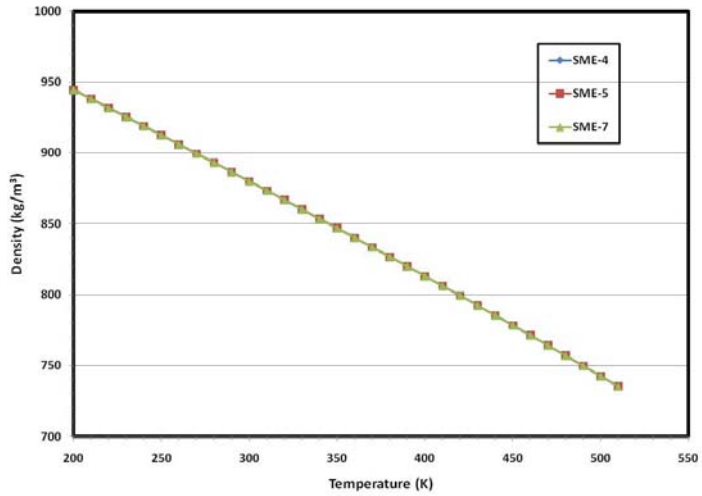

Figure A. Densities of **soybean** methyl ester biodiesel liquids

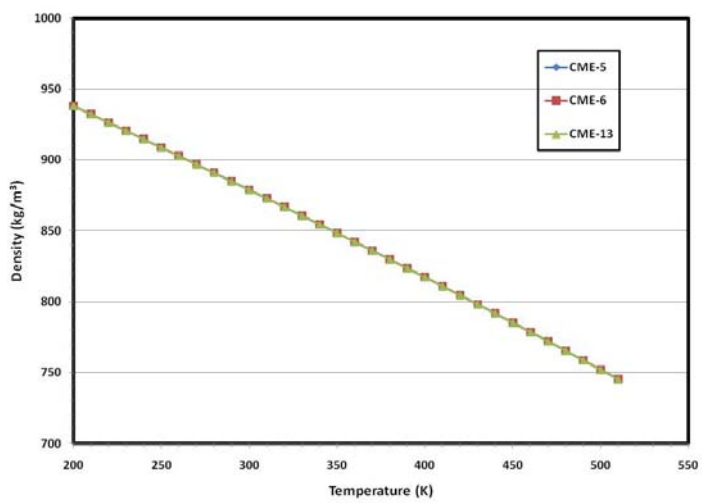

Figure B. Densities of **cottonseed** methyl ester biodiesel liquids

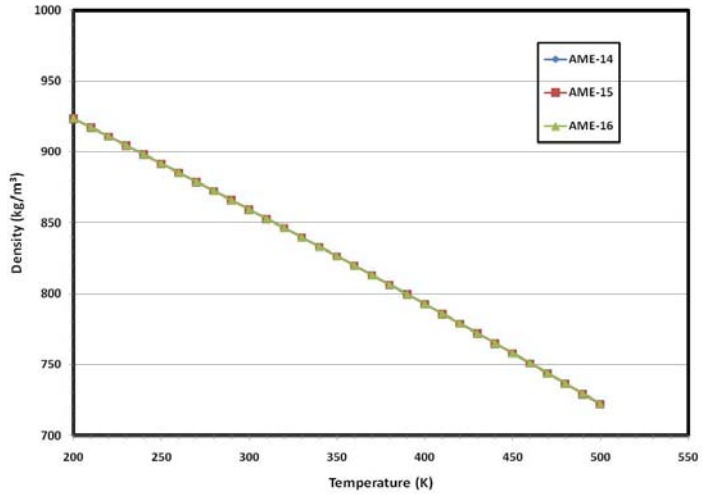

Figure C. Densities of **algae** methyl ester biodiesel liquids

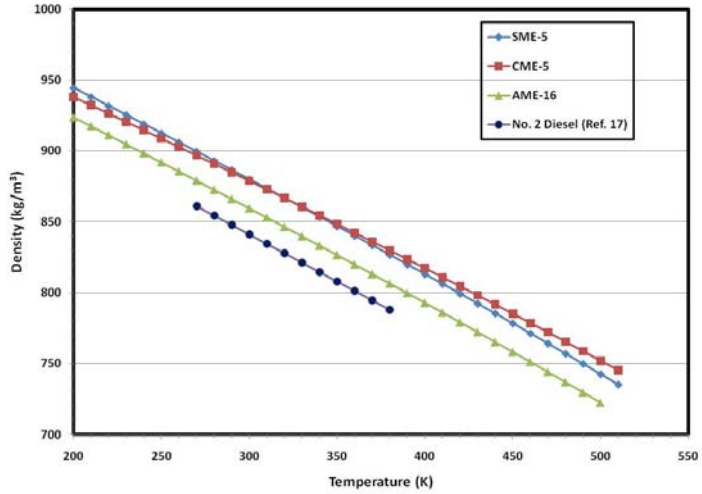

Figure D. Densities of **selected methyl ester biodiesel and No. 2 diesel liquids**

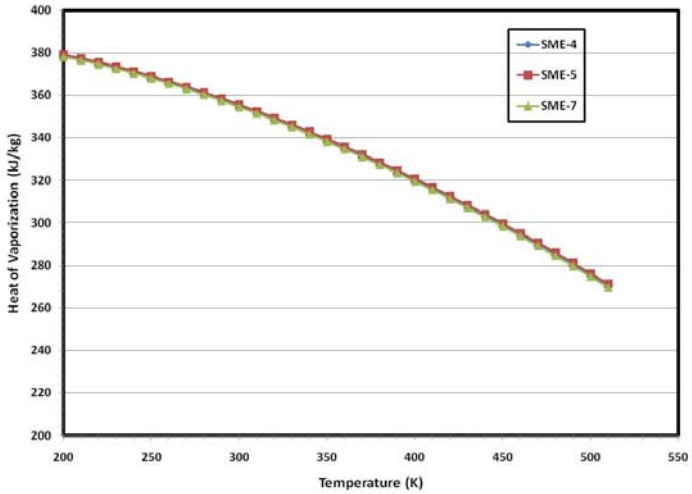

Figure E. Heat of vaporization of **soybean** methyl ester biodiesel liquids

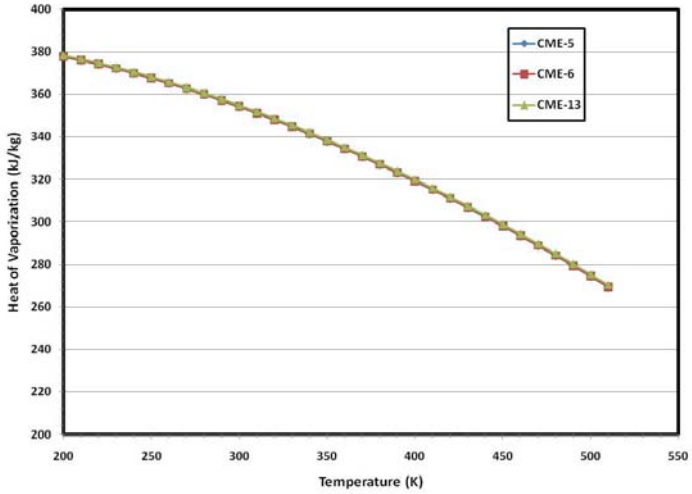

Figure F. Heat of vaporization of **cottonseed** methyl ester biodiesel liquids

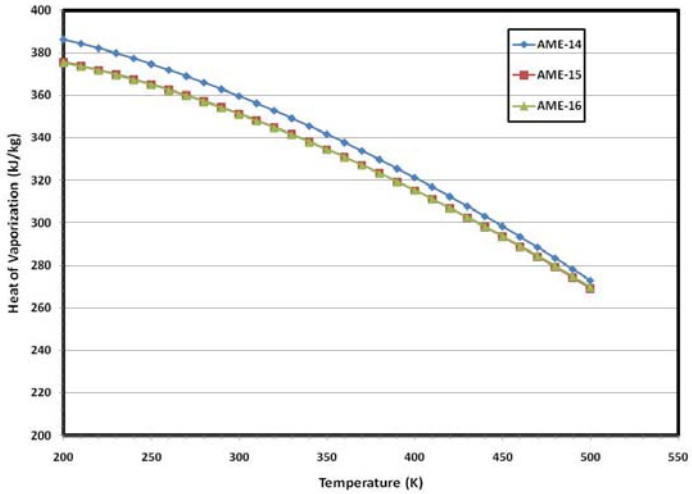

Figure G. Heat of vaporization of **algae** methyl ester biodiesel liquids

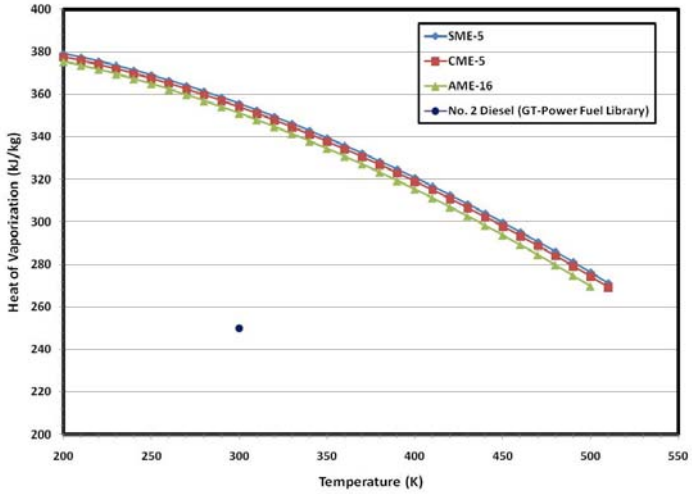

Figure H. Heat of Vaporization of **selected methyl ester biodiesel and No. 2 diesel liquids**

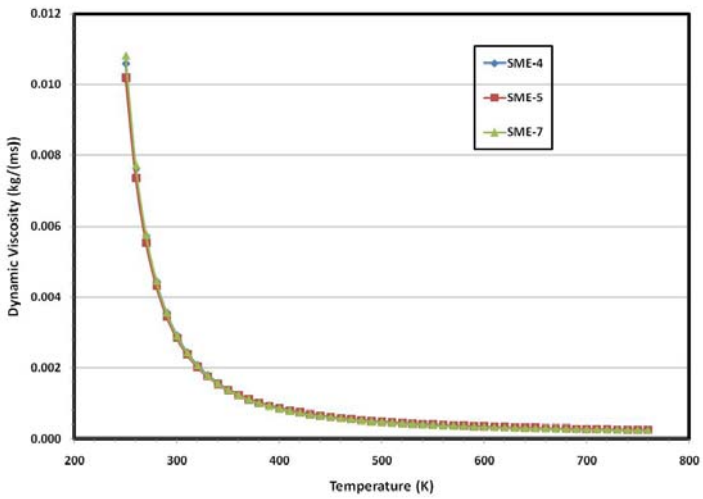

Figure I. Dynamic viscosities of soybean methyl ester biodiesel liquids

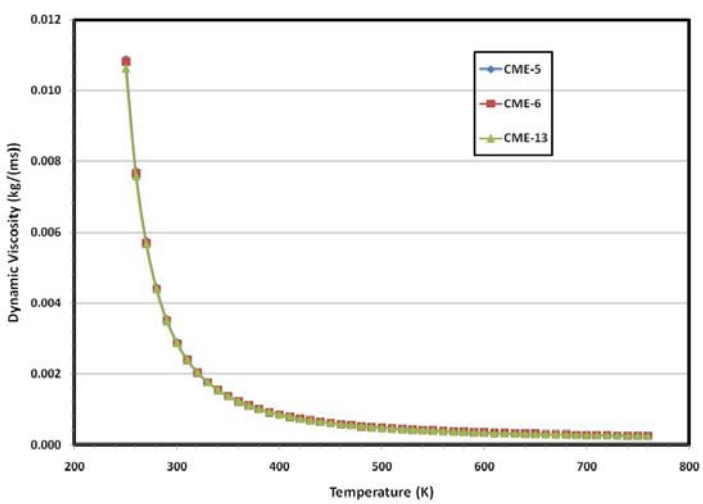

Figure J. Dynamic viscosities of **cottonseed** methyl ester biodiesel liquids

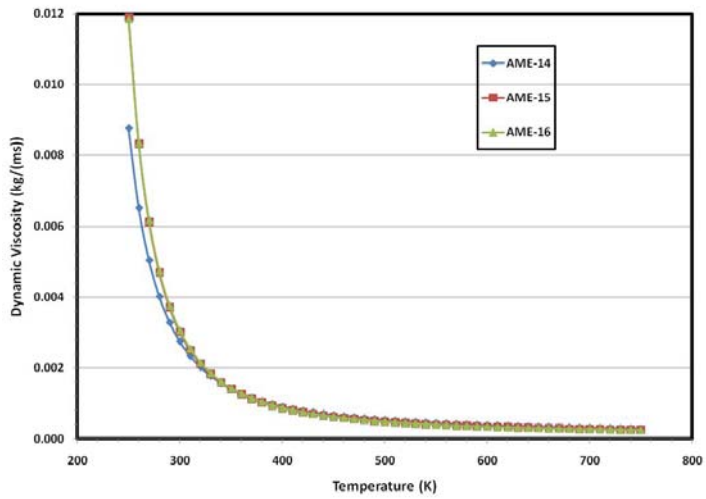

Figure K. Dynamic viscosities of **algae** methyl ester biodiesel liquids

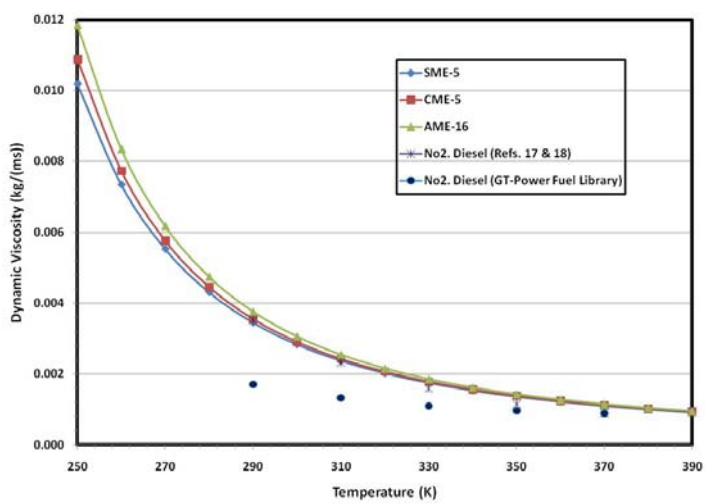

Figure L. Dynamic viscosities of **selected methyl ester biodiesel and No. 2 diesel liquids**

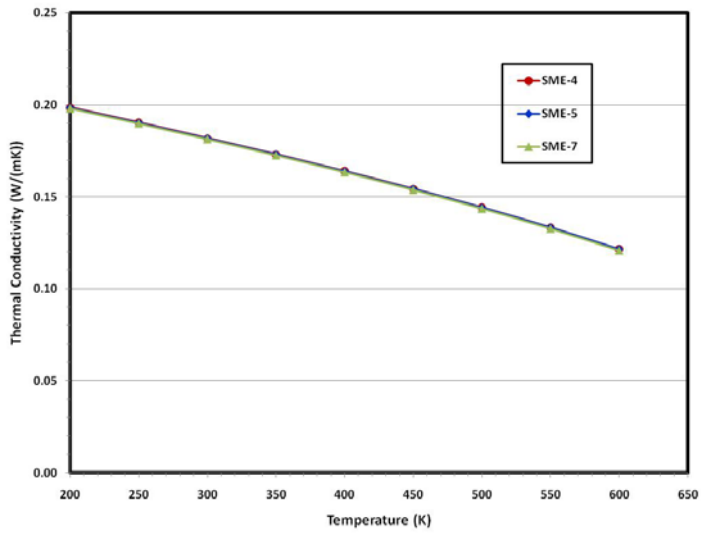

Figure M. Thermal conductivities of **soybean** methyl ester biodiesel liquids

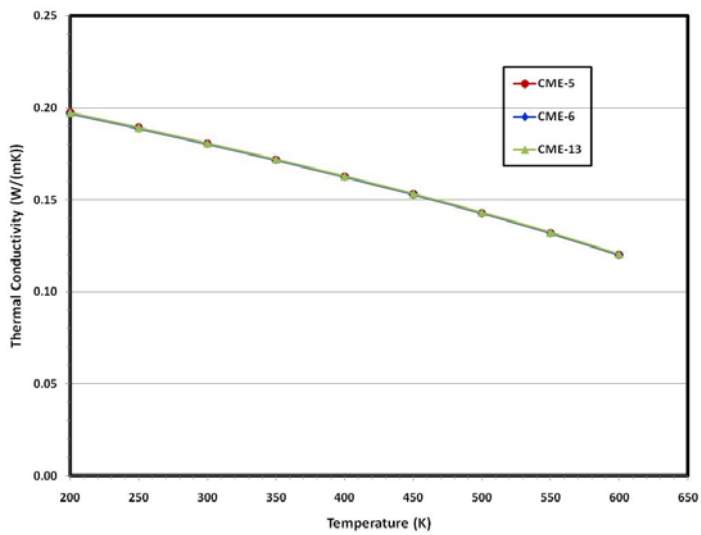

Figure N. Thermal conductivities of **cottonseed** methyl ester biodiesel liquids

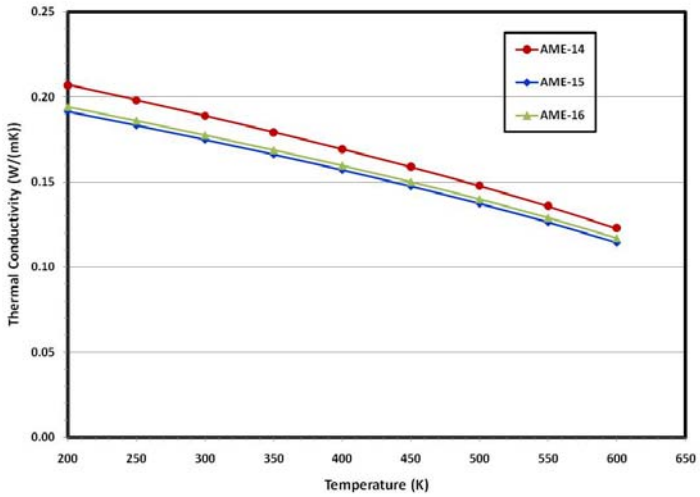

Figure O. Thermal conductivities of **algae** methyl ester biodiesel liquids

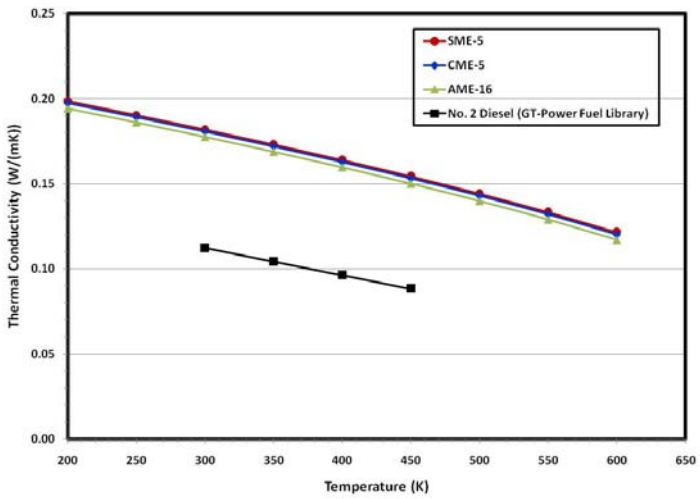

Figure P. Thermal conductivities of **selected methyl ester biodiesel and No. 2 diesel liquids**

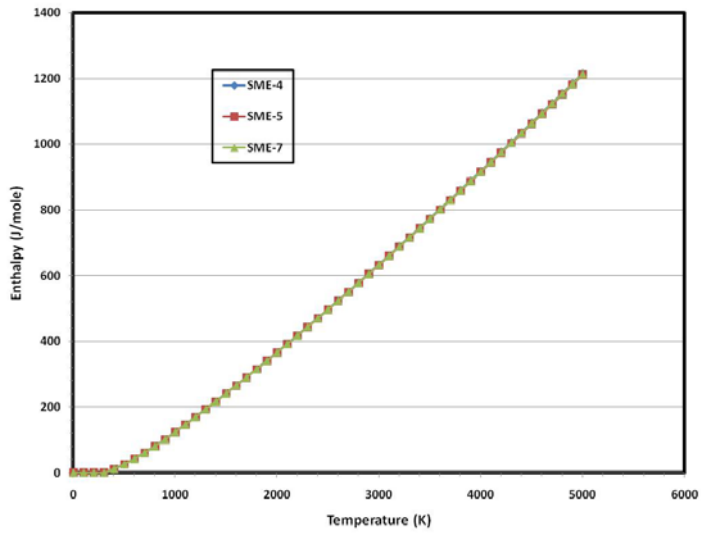

Figure Q. Enthalpies of **soybean** methyl ester biodiesel liquids

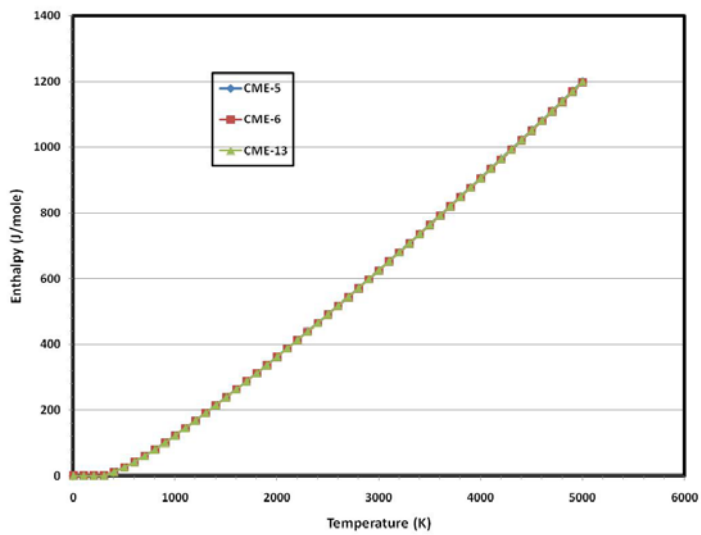

Figure R. Enthalpies of **cottonseed** methyl ester biodiesel liquids

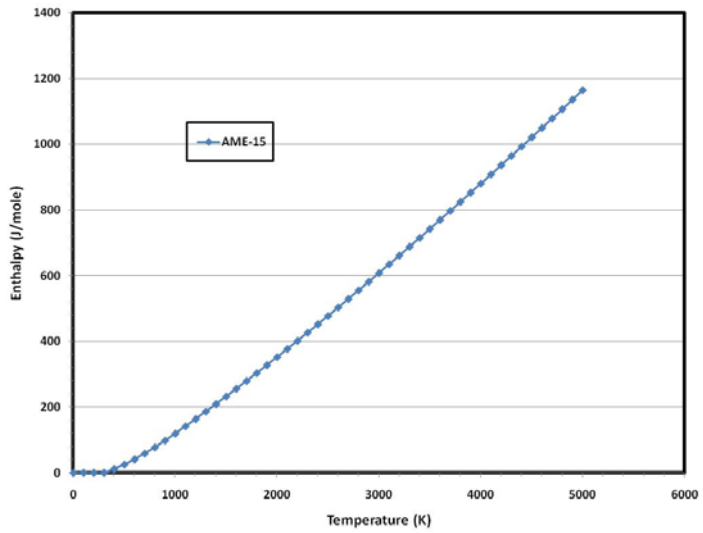

Figure S. Enthalpies of **algae** methyl ester biodiesel liquid

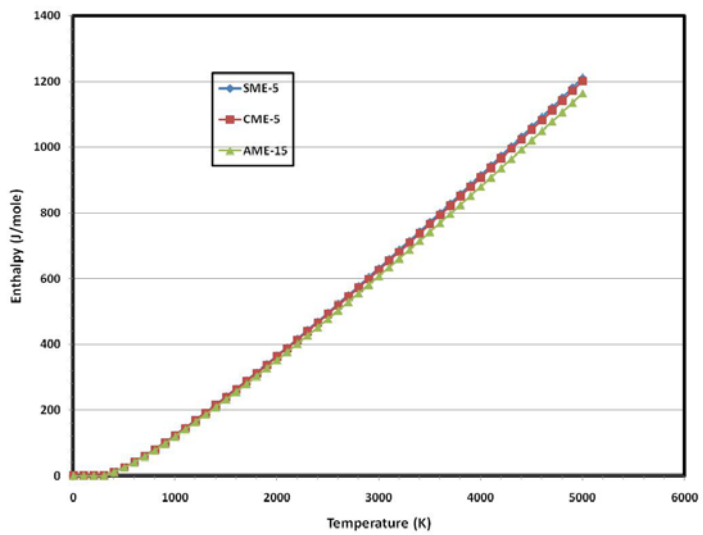

Figure T. Enthalpies of **selected methyl ester biodiesel liquids**

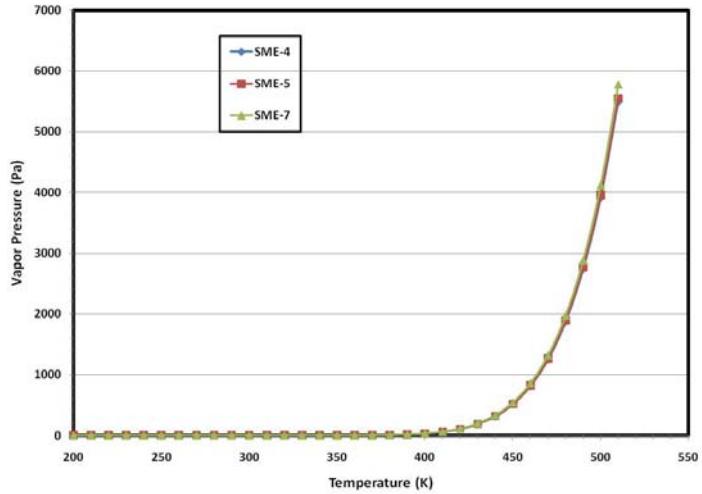

Figure U. Vapor pressures of **soybean** methyl ester biodiesels

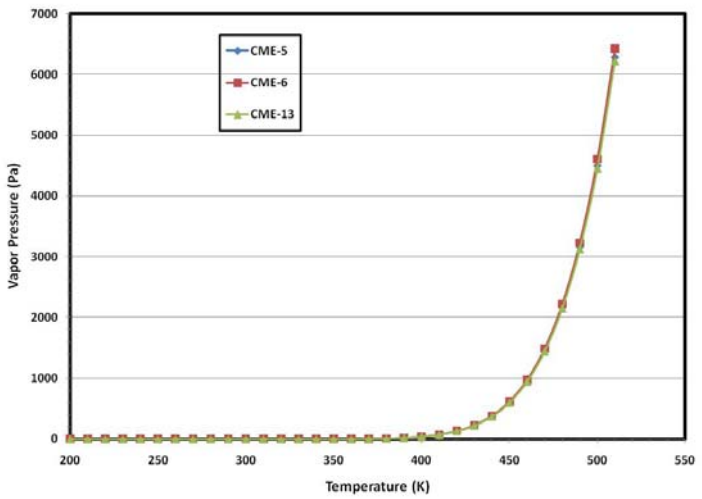

Figure V. Vapor pressures of **cottonseed** methyl ester biodiesels

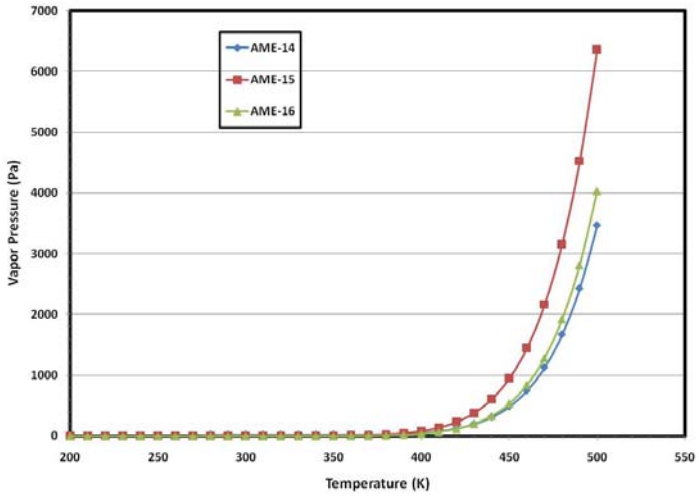

Figure W. Vapor pressures of **algae** methyl ester biodiesels

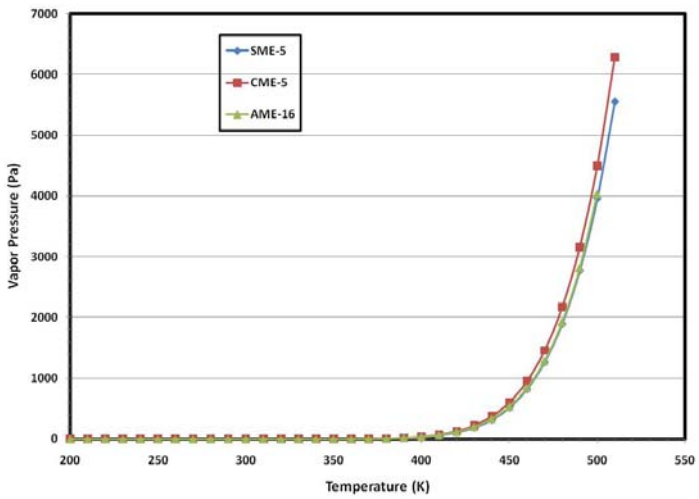

Figure X. Vapor pressures of **selected methyl ester biodiesels**

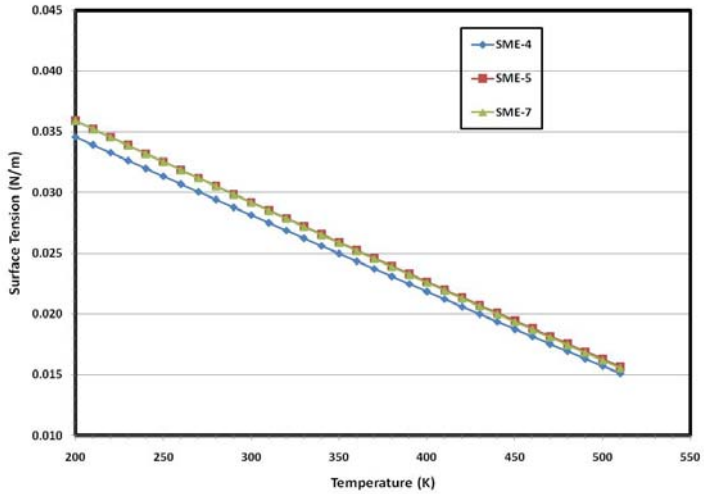

Figure Y. Surface tensions of **soybean** methyl ester biodiesel liquids

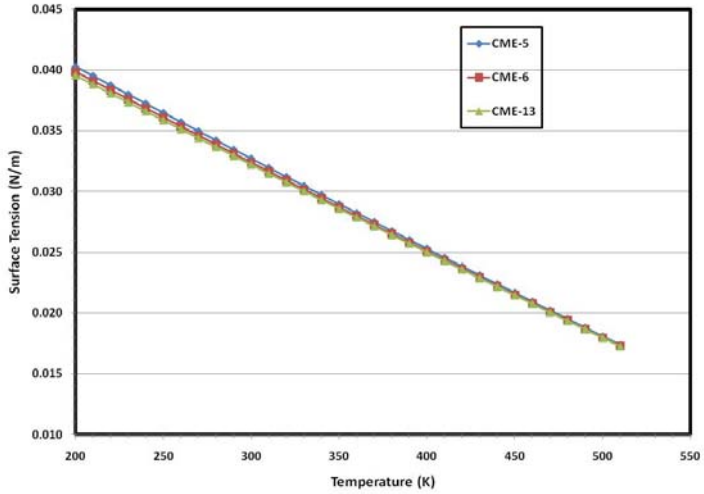

Figure Z. Surface tensions of **cottonseed** methyl ester biodiesel liquids

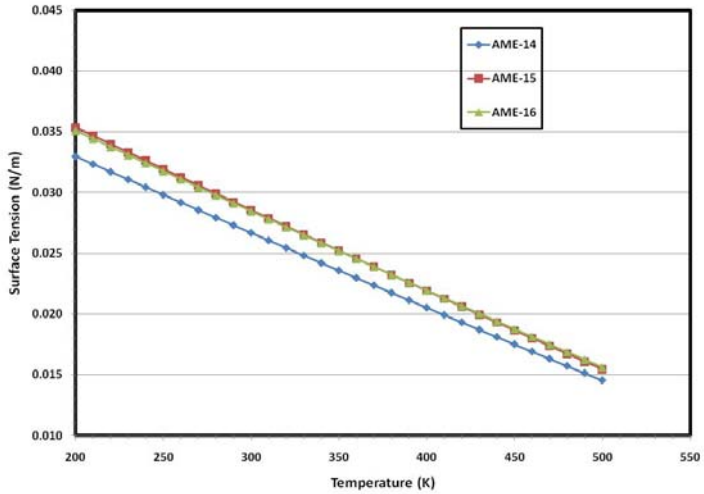

Figure AA. Surface tensions of **algae** methyl ester biodiesel liquids

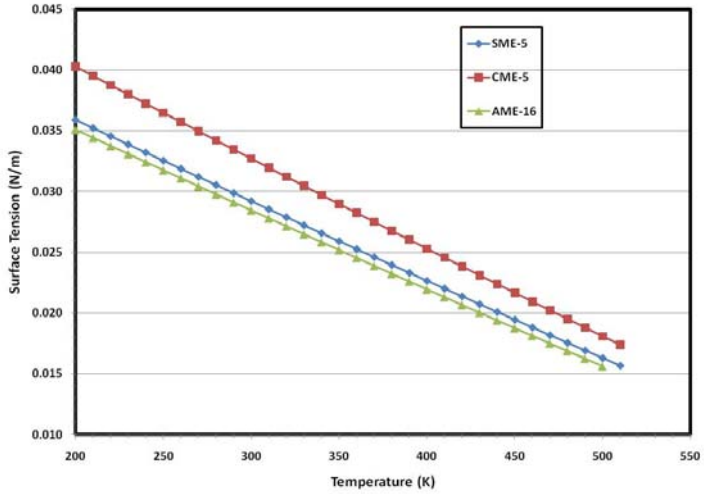

Figure BB. Surface tensions of **selected methyl ester biodiesel liquids**

Figures CC-HH: Calculated liquid heat capacities and liquid enthalpies of biodiesels

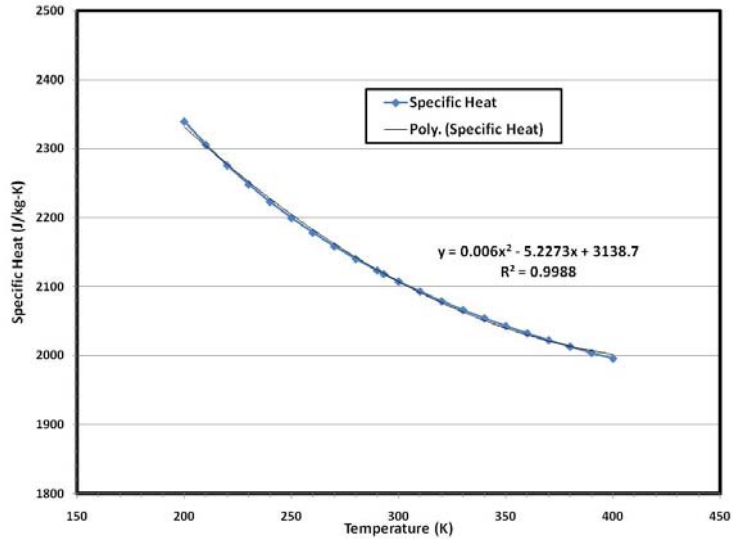

Figure CC. Liquid heat capacity of soybean methyl ester biodiesel (SME-31)

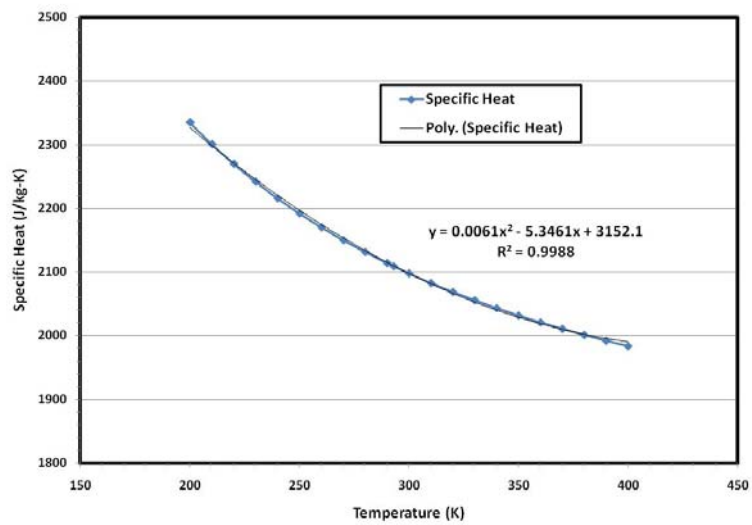

Figure DD. Liquid heat capacity of cottonseed methyl ester biodiesel (CME-31)

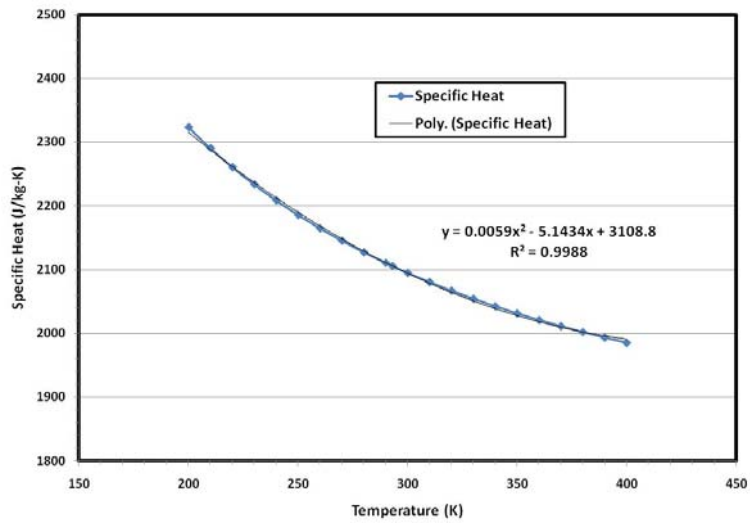

Figure EE. Liquid heat capacity of algae methyl ester biodiesel (AME-42)

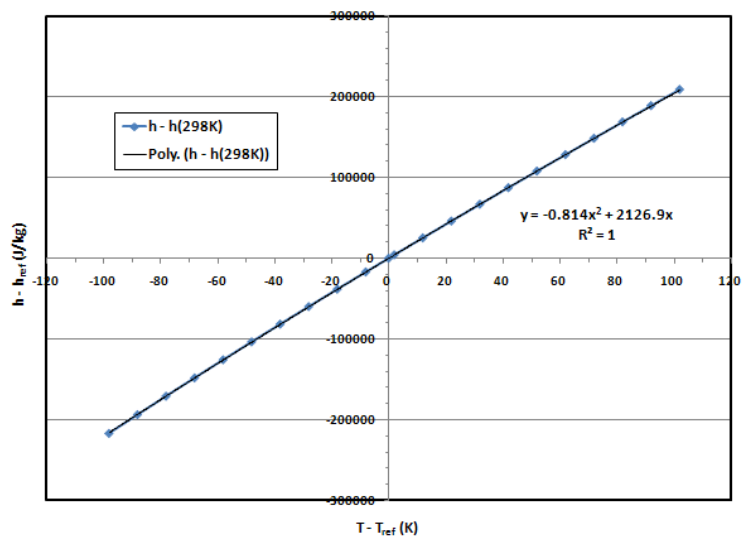

Figure FF. Liquid enthalpy of soybean methyl ester biodiesel (SME-31)

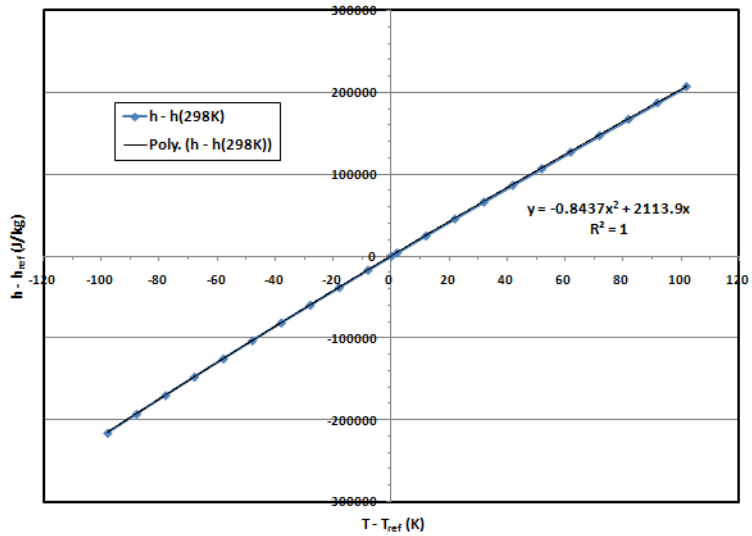

Figure GG. Liquid enthalpy of cottonseed methyl ester biodiesel (CME-31)

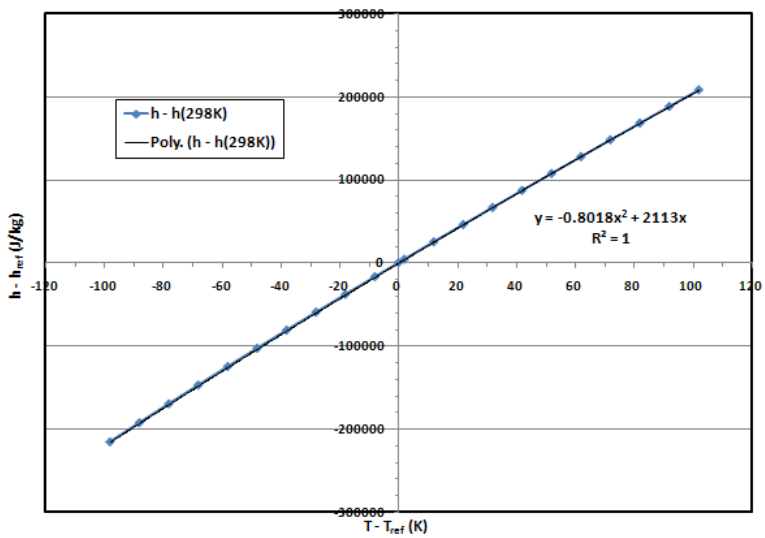

Figure HH. Liquid enthalpy of algae methyl ester biodiesel (AME-42)

Figures II - NN: Calculated vapor heat capacities and enthalpies of biodiesels

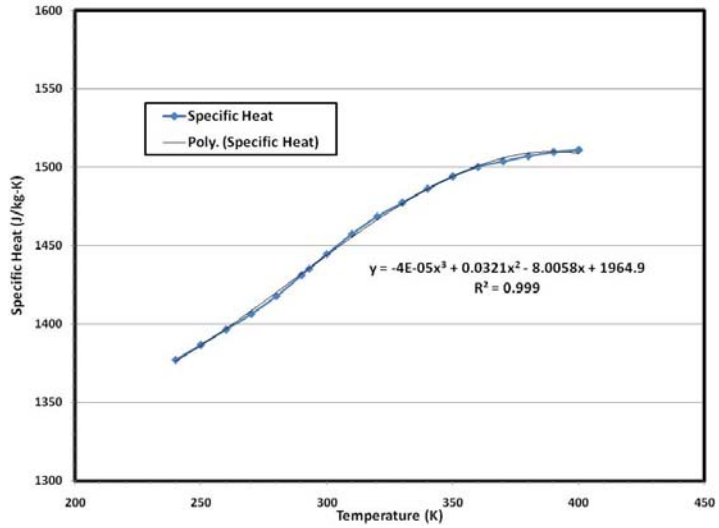

Figure II. Vapor heat capacity of soybean methyl ester biodiesel (SME-31)

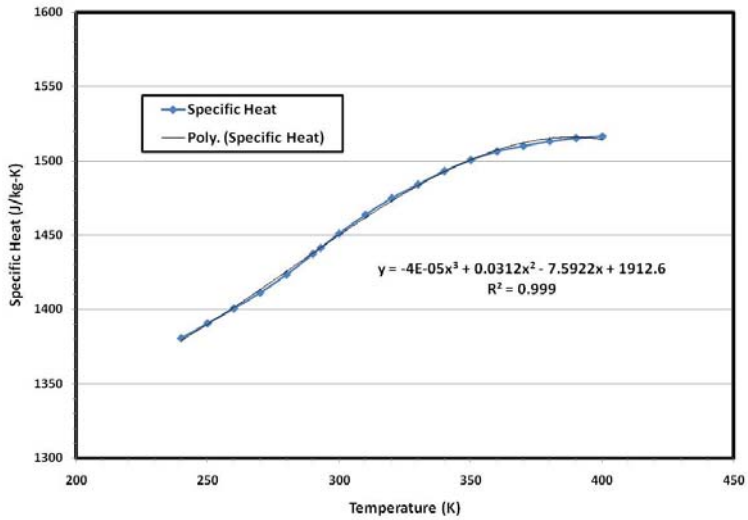

Figure JJ. Vapor heat capacity of cottonseed methyl ester biodiesel (CME-31)

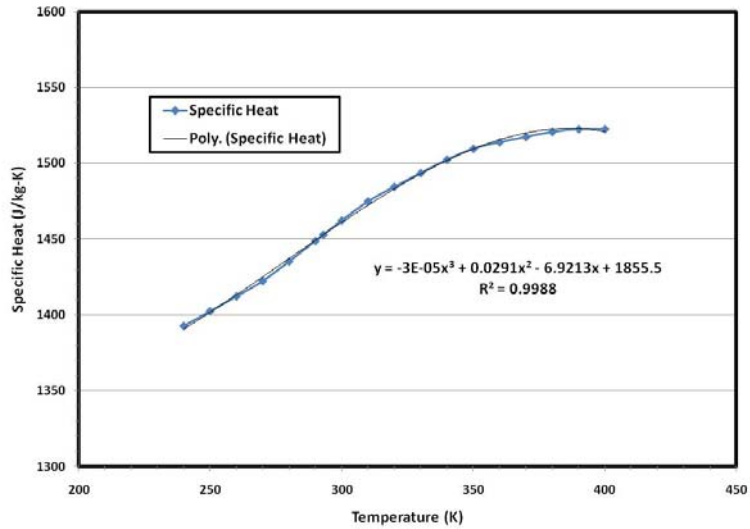

Figure KK. Vapor heat capacity of algae methyl ester biodiesel (AME-42)

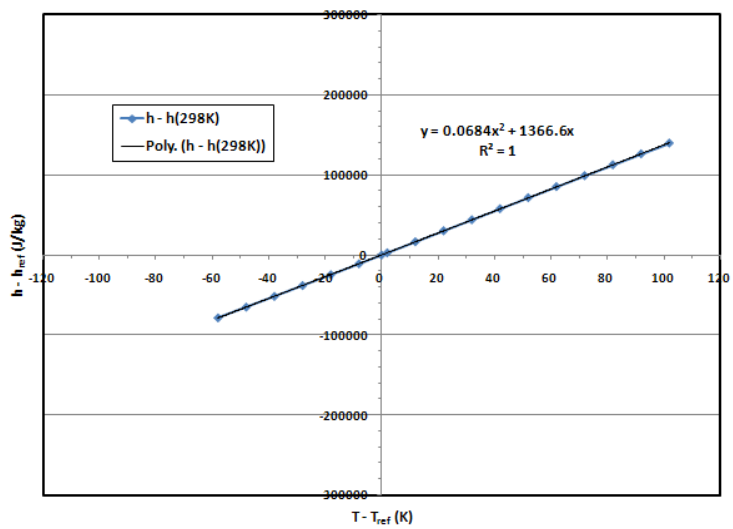

Figure LL. Vapor enthalpy of soybean methyl ester biodiesel (SME-31)

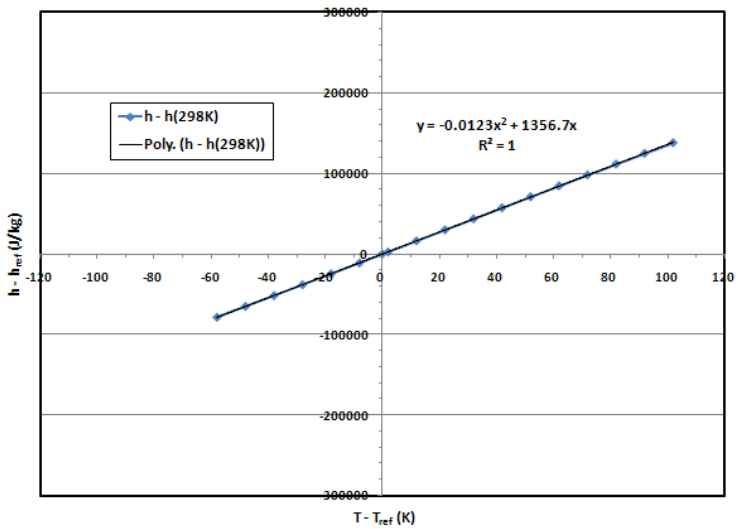

Figure MM. Vapor enthalpy of cottonseed methyl ester biodiesel (CME-31)

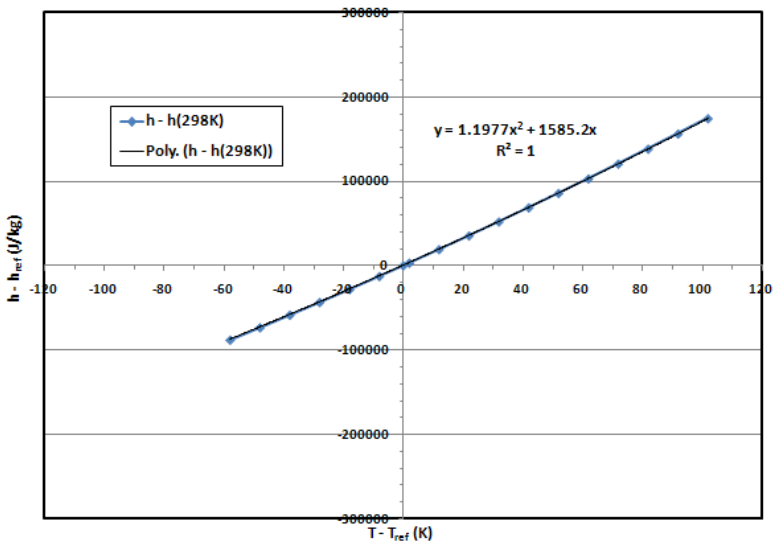

Figure NN. Vapor enthalpy of algae methyl ester biodiesel (AME-42)

Figures OO - VV: CalcGraf Results (No.2 Diesel, 2200 RPM)

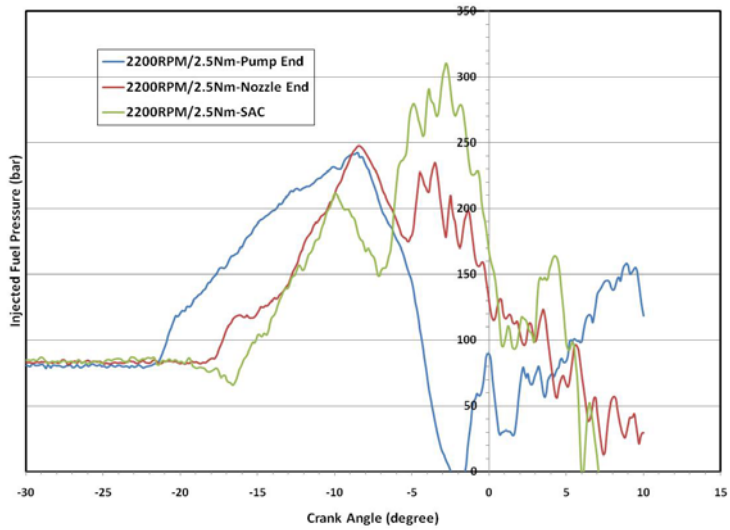

Figure OO. Measured fuel injector pressure profiles at engine speed of 2200 rpm and engine load of 2.5 Nm (No. 2 diesel fuel)

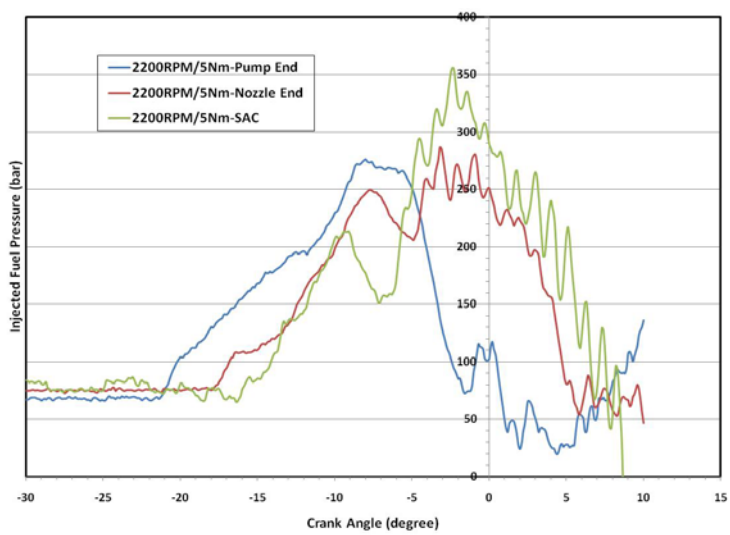

Figure PP. Measured fuel injector pressure profiles at engine speed of 2200 rpm and engine load of 5 Nm (No. 2 diesel fuel)

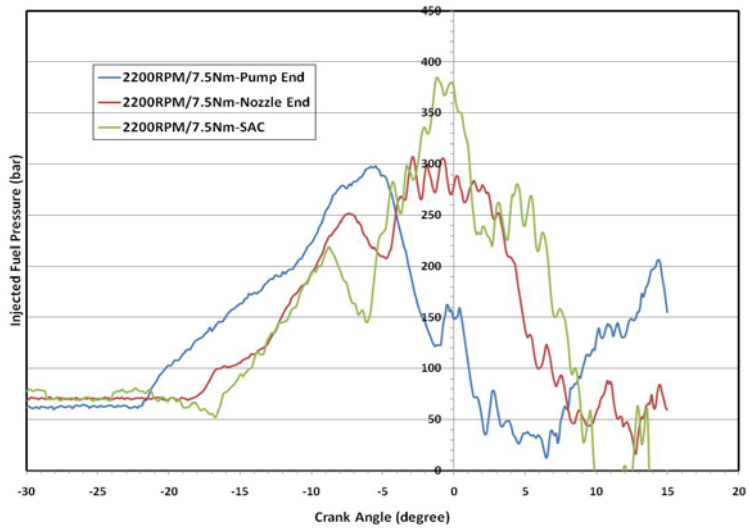

Figure QQ. Measured fuel injector pressure profiles at engine speed of 2200 rpm and engine load of 7.5 Nm (No. 2 diesel fuel)

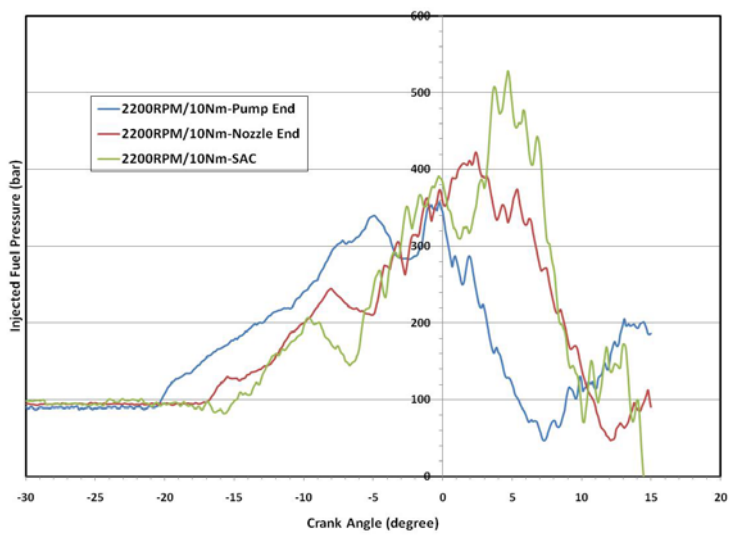

Figure RR. Measured fuel injector pressure profiles at engine speed of 2200 rpm and engine load of 10 Nm (No. 2 diesel fuel)

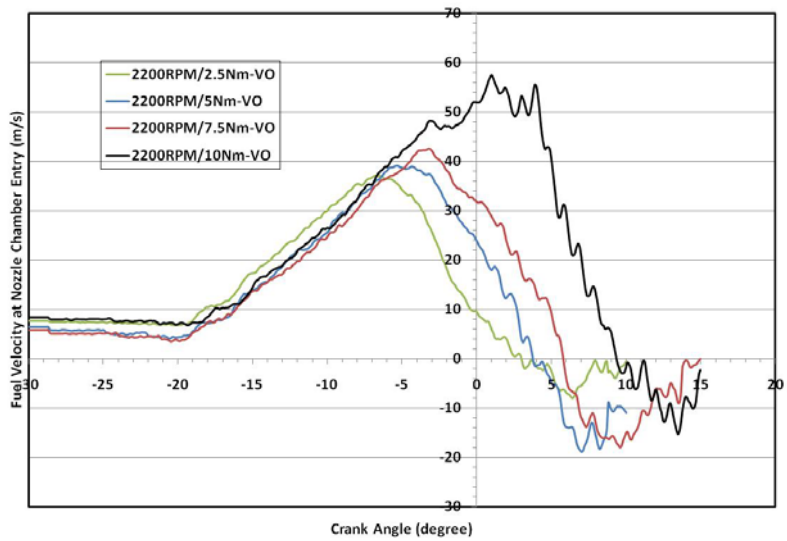

Figure SS. Computationally-determined fuel velocities at fuel injector nozzle chamber entry at engine speed of 2200 rpm and engine loads of 2.5/5/7.5/10 Nm (No. 2 diesel fuel)

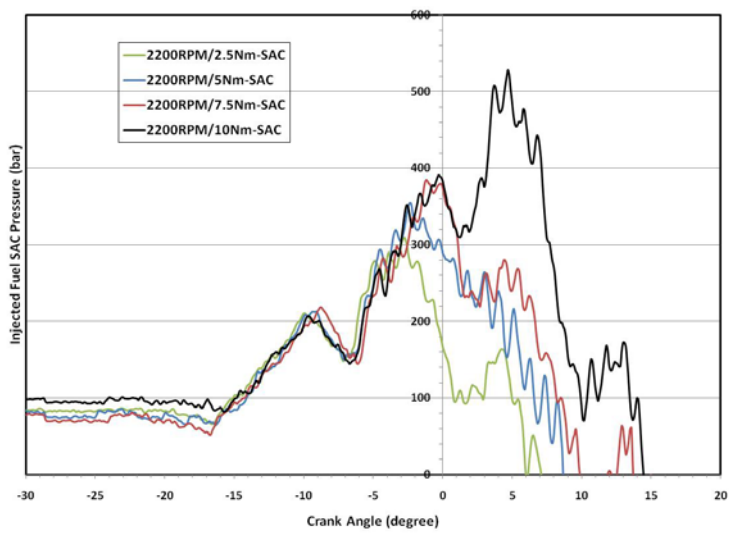

Figure TT. Computationally-determined fuel injector sac pressure profiles at engine speed of 2200 rpm and engine loads of 2.5/5/7.5/10 Nm (No. 2 diesel fuel)

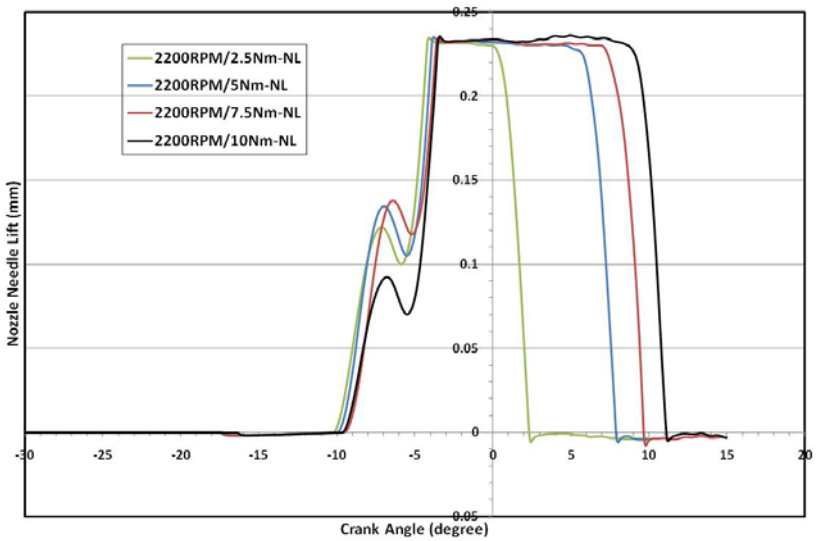

Figure UU. Measured fuel injector nozzle needle lift profiles at engine speed of 2200 rpm and engine loads of 2.5/5/7.5/10 Nm (No. 2 diesel fuel)

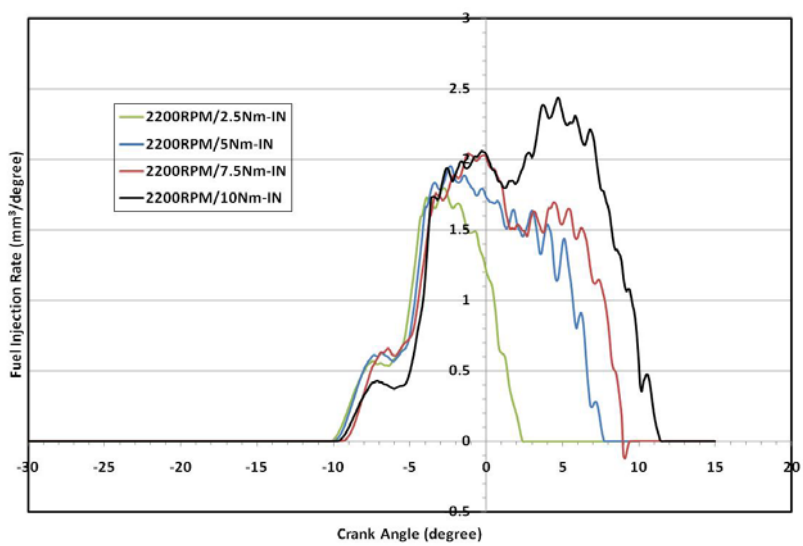

Figure VV. Measured fuel injection rate profiles at engine speed of 2200 rpm and engine loads of 2.5/5/7.5/10 Nm (No. 2 diesel fuel)

Figures WW - DDD: CalcGraf Results (No.2 Diesel, 2600 RPM)

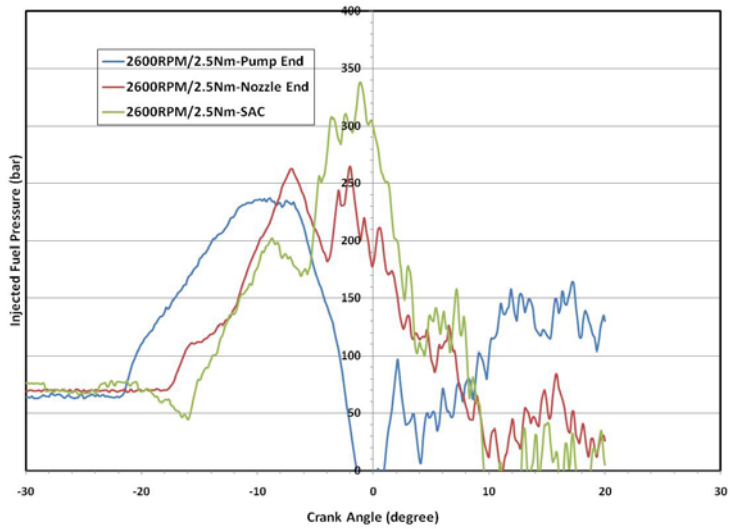

Figure WW. Measured fuel injector pressure profiles at engine speed of 2600 rpm and engine load of 2.5 Nm (No. 2 diesel fuel)

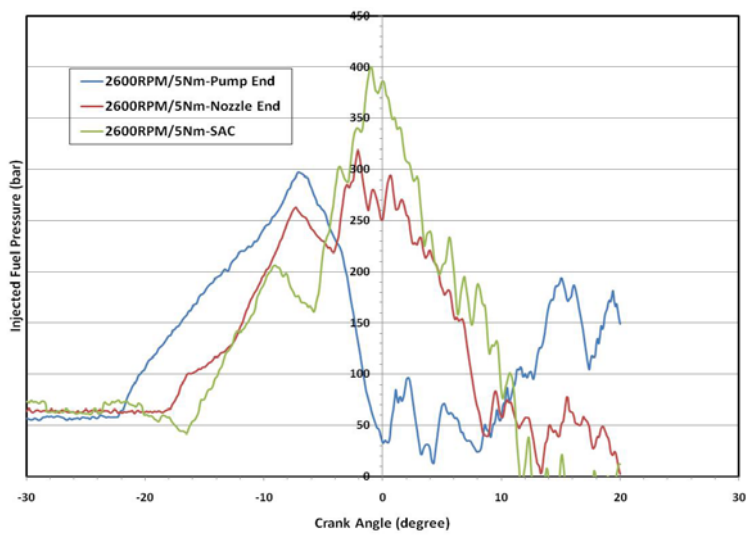

Figure XX. Measured fuel injector pressure profiles at engine speed of 2600 rpm and engine load of 5 Nm (No. 2 diesel fuel)

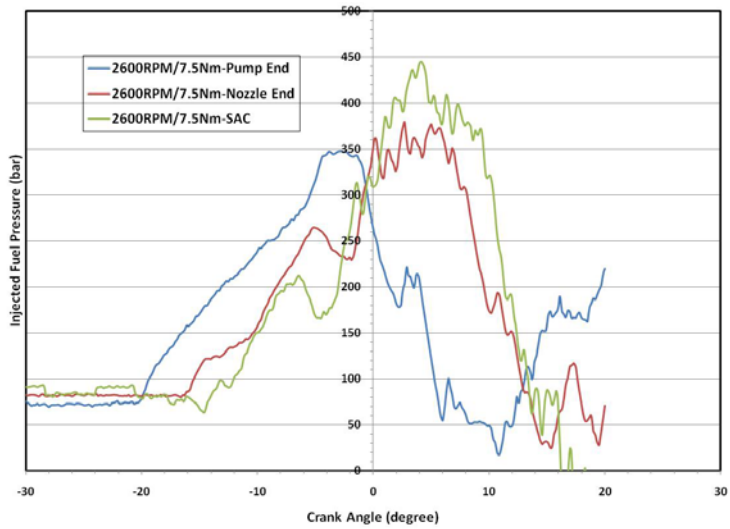

Figure YY. Measured fuel injector pressure profiles at engine speed of 2600 rpm and engine load of 7.5 Nm (No. 2 diesel fuel)

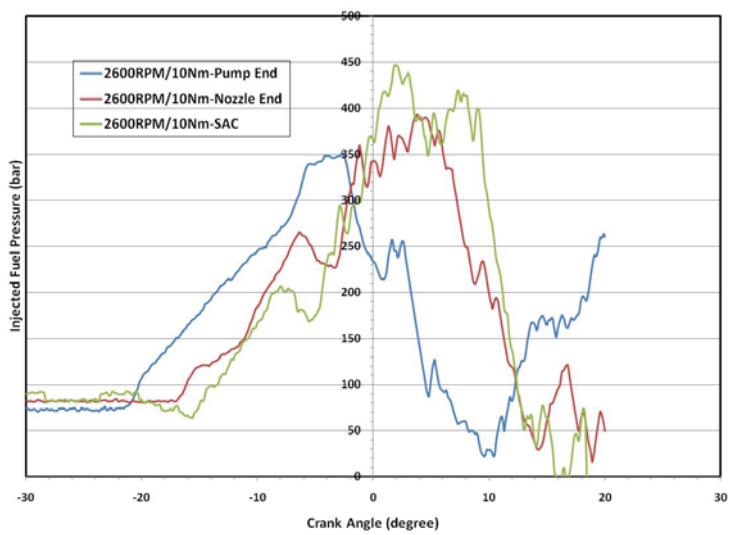

Figure ZZ. Measured fuel injector pressure profiles at engine speed of 2600 rpm and engine load of 10 Nm (No. 2 diesel fuel)

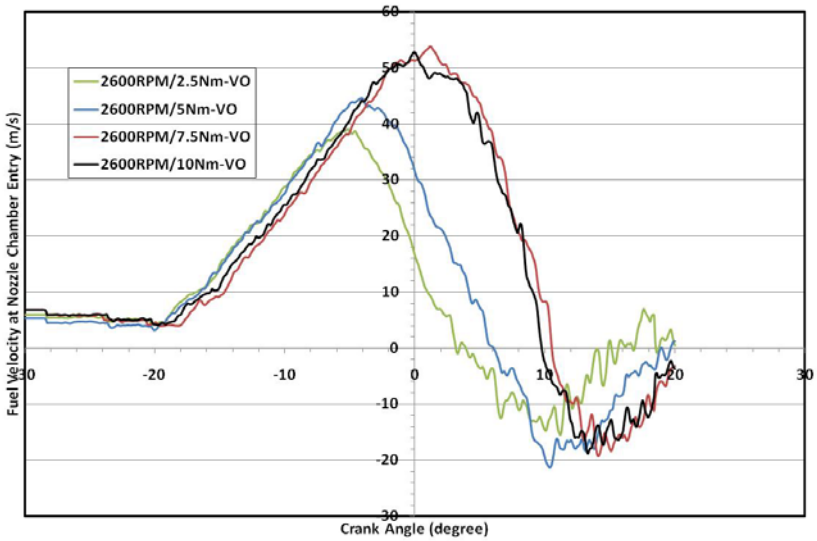

Figure AAA. Computationally-determined fuel velocities at fuel injector nozzle chamber entry at engine speed of 2600 rpm and engine loads of 2.5/5/7.5/10 Nm (No. 2 diesel fuel)

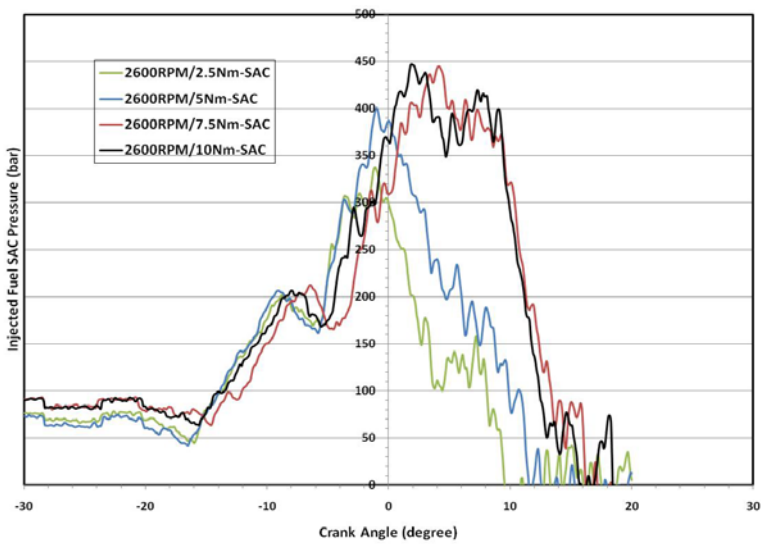

Figure BBB. Computationally-determined fuel injector sac pressure profiles at engine speed of 2600 rpm and engine loads of 2.5/5/7.5/10 Nm (No. 2 diesel fuel)

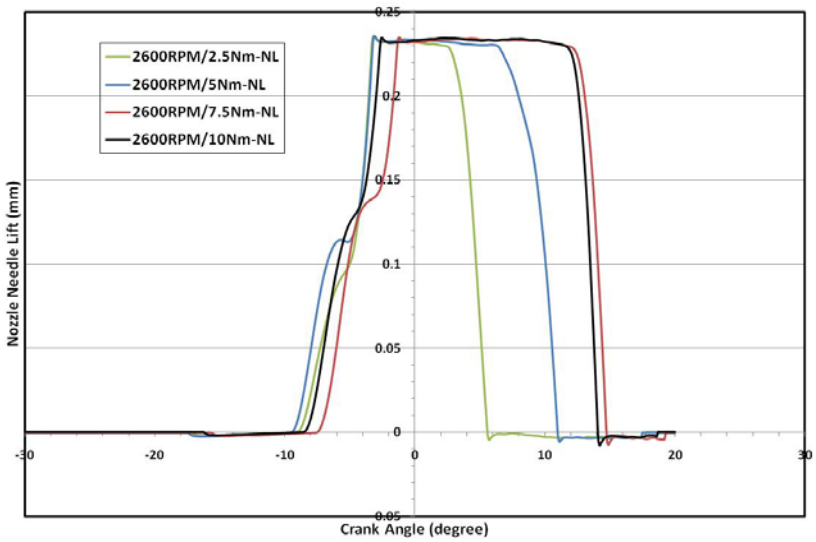

Figure CCC. Measured fuel injector nozzle needle lift profiles at engine speed of 2600 rpm and engine loads of 2.5/5/7.5/10 Nm (No. 2 diesel fuel)

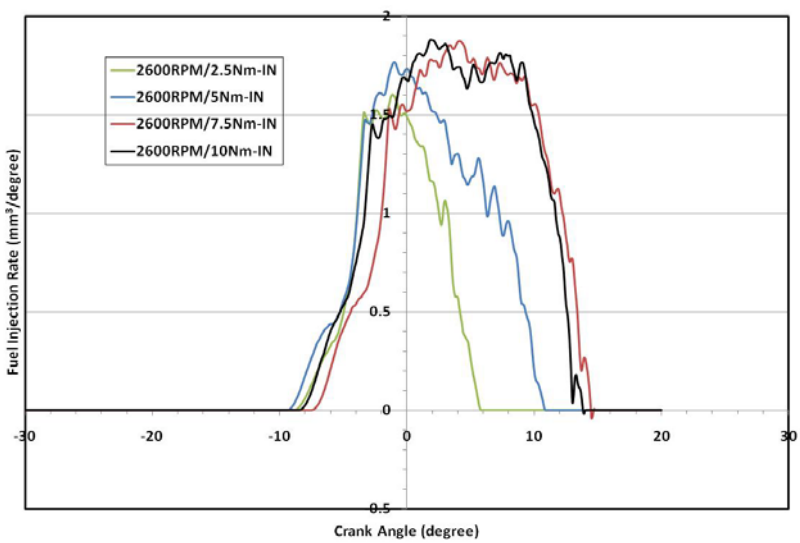

Figure DDD. Measured fuel injection rate profiles at engine speed of 2600 rpm and engine loads of 2.5/5/7.5/10 Nm (No. 2 diesel fuel)

Figures EEE - MMM: CalcGraf Results (Soy Biodiesel, 2200 RPM)

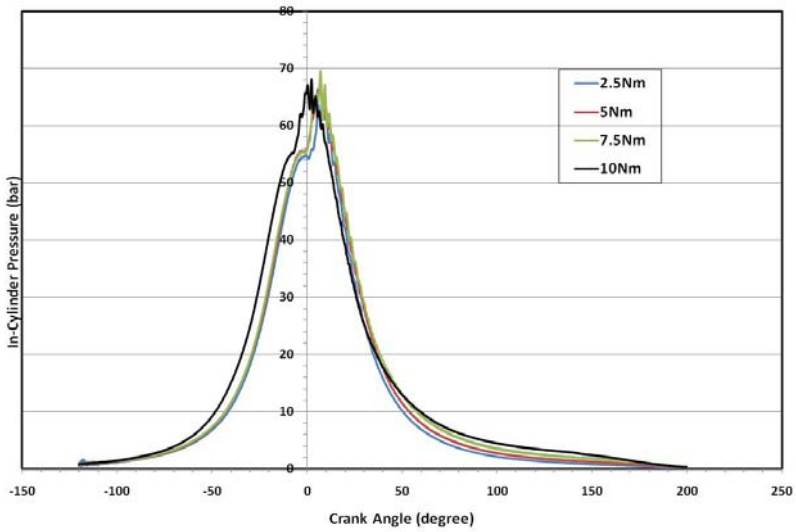

Figure EEE. Measured in-cylinder pressure profiles at engine speed of 2200 rpm under four different engine loads (B100 soybean biodiesel fuel)

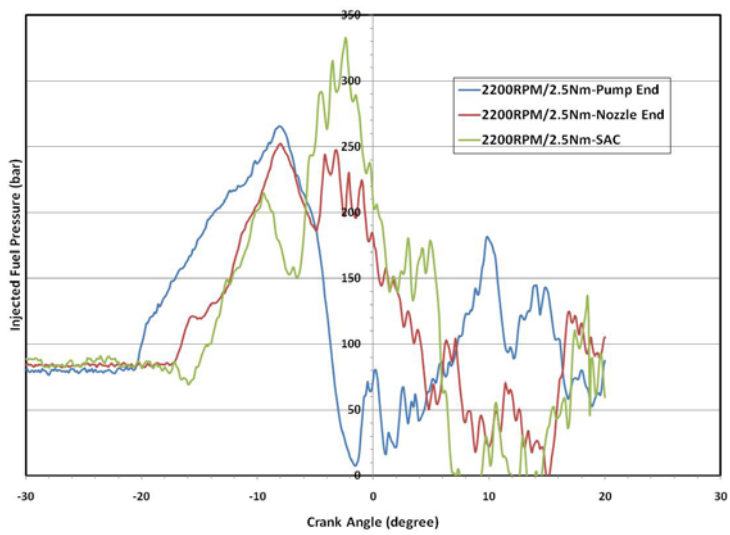

Figure FFF. Measured fuel injector pressure profiles at engine speed of 2200 rpm and engine load of 2.5 Nm (B100 soybean biodiesel fuel)

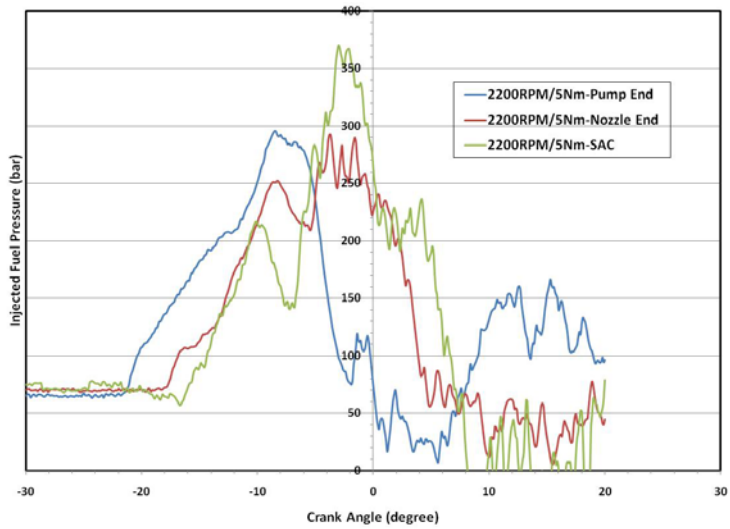

Figure GGG. Measured fuel injector pressure profiles at engine speed of 2200 rpm and engine load of 5 Nm (B100 soybean biodiesel fuel)

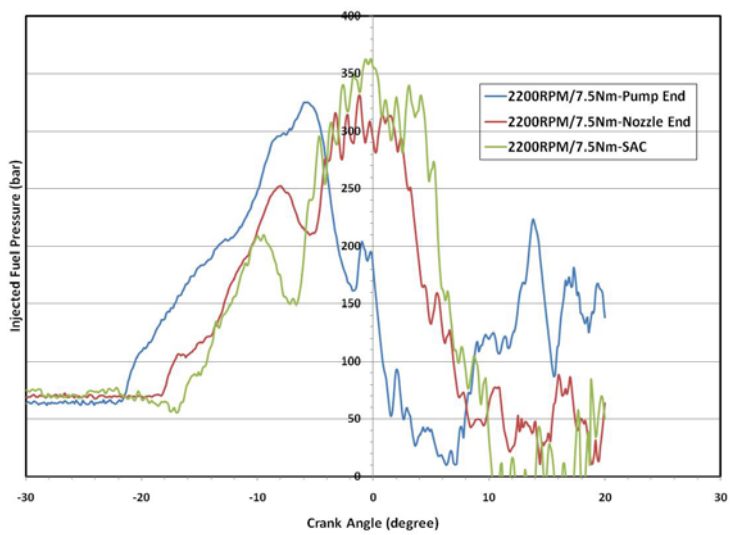

Figure HHH. Measured fuel injector pressure profiles at engine speed of 2200 rpm and engine load of 7.5 Nm (B100 soybean biodiesel fuel)

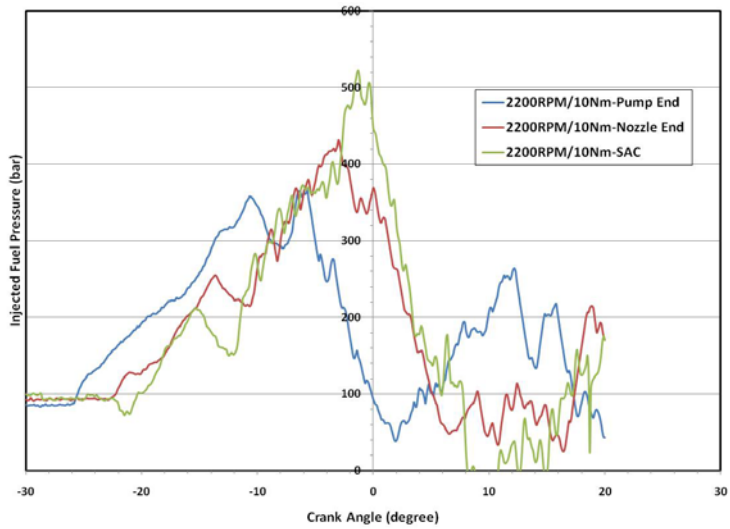

Figure III. Measured fuel injector pressure profiles at engine speed of 2200 rpm and engine load of 10 Nm (B100 soybean biodiesel fuel)

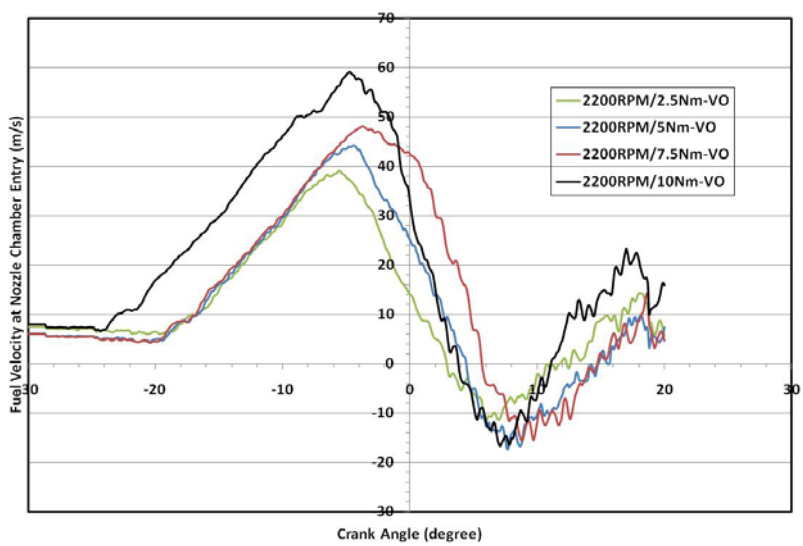

Figure JJJ. Computationally-determined fuel velocities at fuel injector nozzle chamber entry at engine speed of 2200 rpm and engine loads of 2.5/5/7.5/10 Nm (B100 soybean biodiesel fuel)

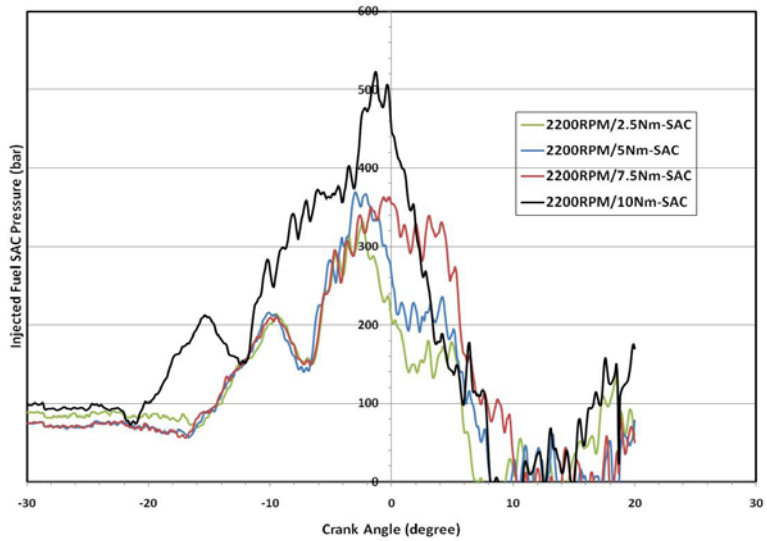

Figure KKK. Computationally-determined fuel injector sac pressure profiles at engine speed of 2200 rpm and engine loads of 2.5/5/7.5/10 Nm (B100 soybean biodiesel fuel)

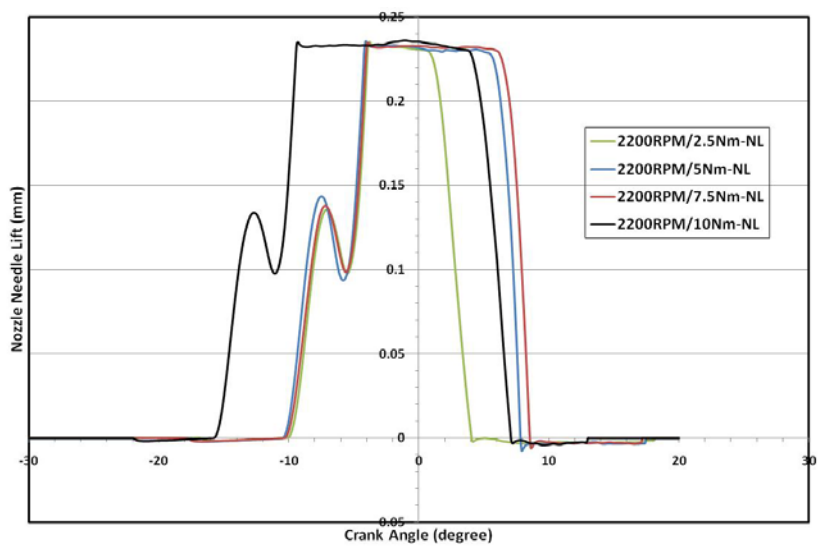

Figure LLL. Measured fuel injector nozzle needle lift profiles at engine speed of 2200 rpm and engine loads of 2.5/5/7.5/10 Nm (B100 soybean biodiesel fuel)

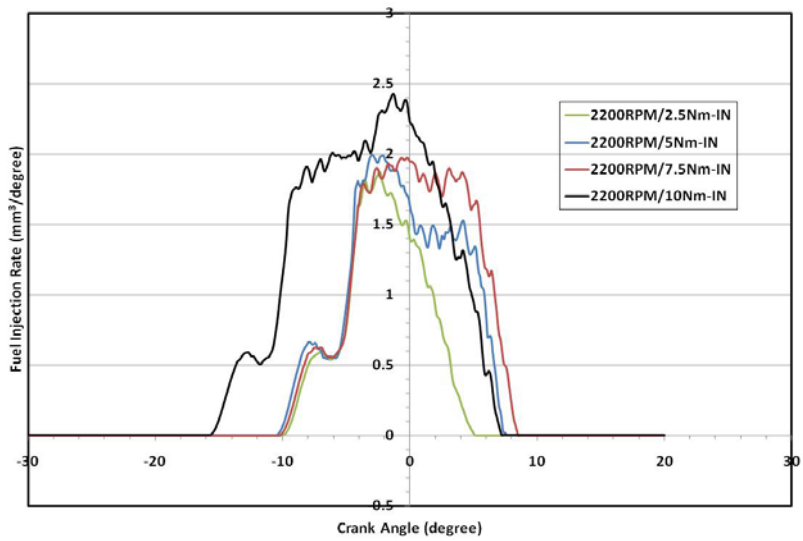

Figure MMM. Measured fuel injection rate profiles at engine speed of 2200 rpm and engine loads of 2.5/5/7.5/10 Nm (B100 soybean biodiesel fuel)

Figures NNN - VVV: CalcGraf Results (Soy Biodiesel, 2600 RPM)

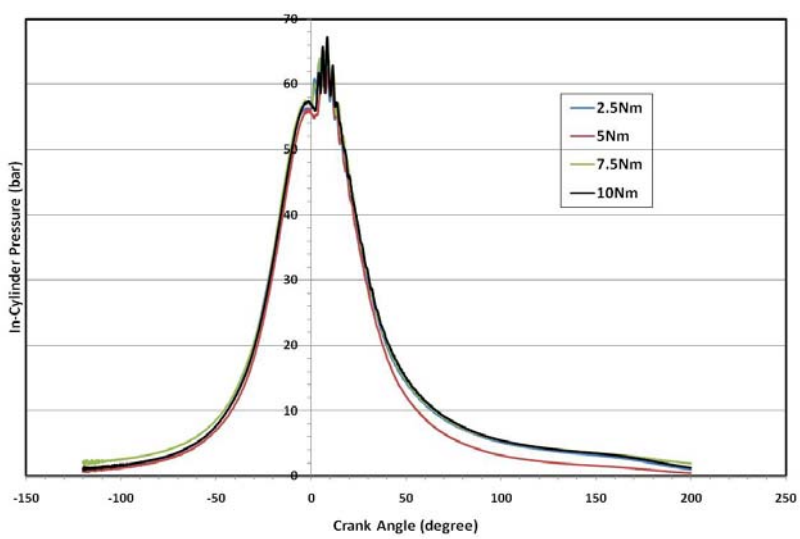

Figure NNN. Measured in-cylinder pressure profiles at engine speed of 2600 rpm under four different engine loads (B100 soybean biodiesel fuel)

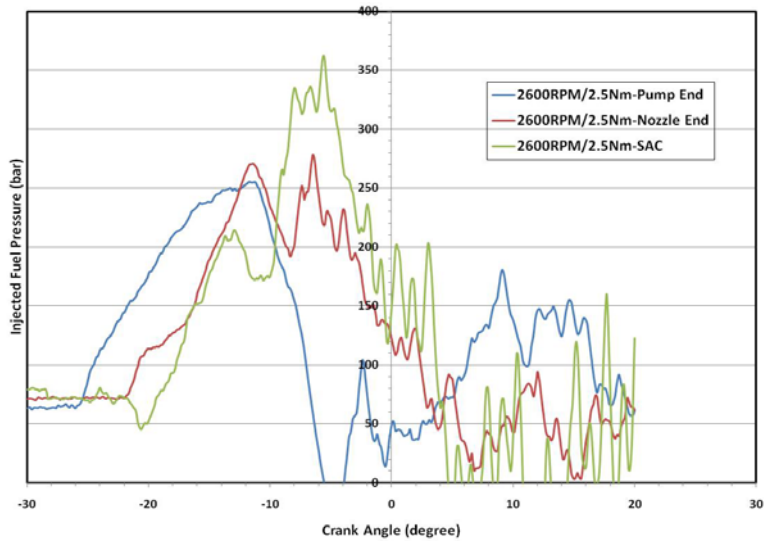

Figure OOO. Measured fuel injector pressure profiles at engine speed of 2600 rpm and engine load of 2.5 Nm (B100 soybean biodiesel fuel)

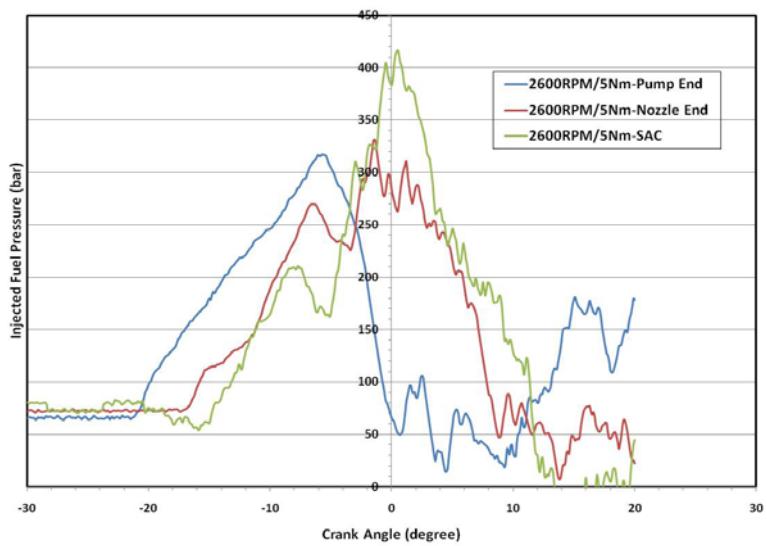

Figure PPP. Measured fuel injector pressure profiles at engine speed of 2600 rpm and engine load of 5 Nm (B100 soybean biodiesel fuel)

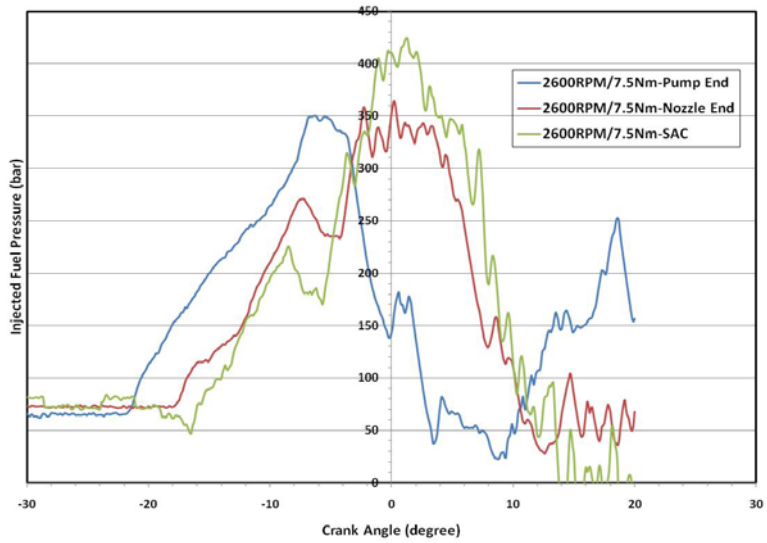

Figure QQQ. Measured fuel injector pressure profiles at engine speed of 2600 rpm and engine load of 7.5 Nm (B100 soybean biodiesel fuel)

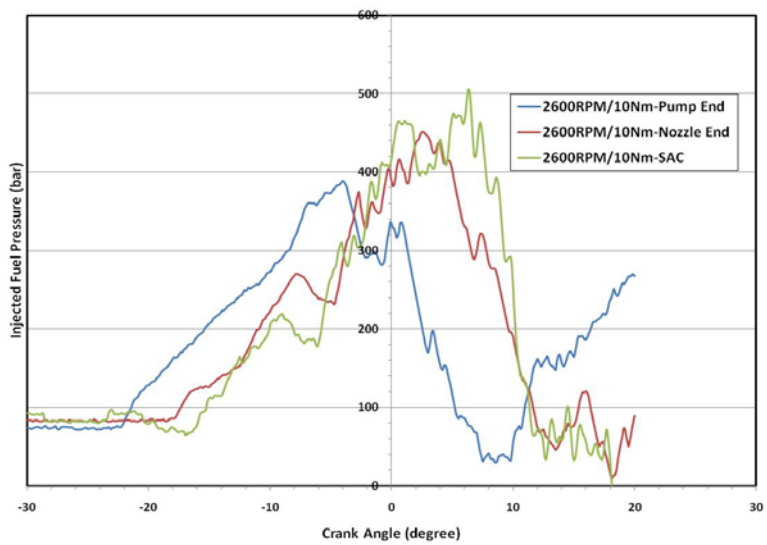

Figure RRR. Measured fuel injector pressure profiles at engine speed of 2600 rpm and engine load of 10 Nm (B100 soybean biodiesel fuel)

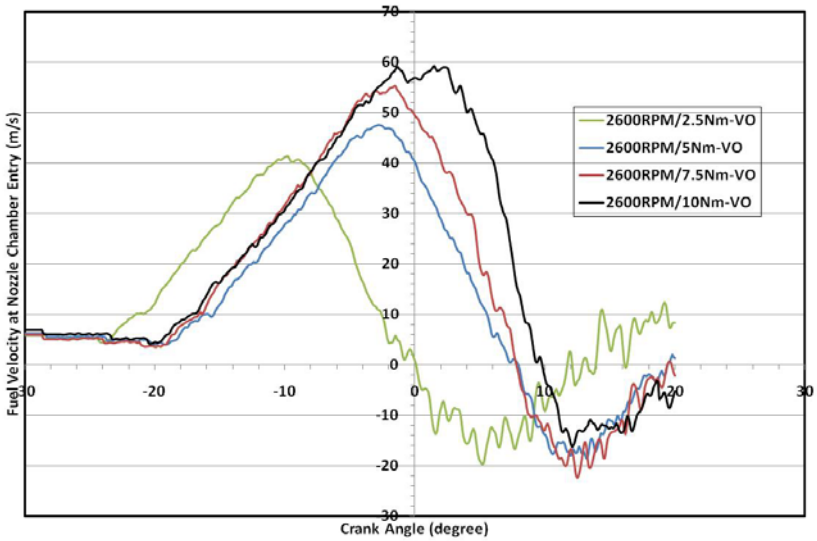

Figure SSS. Computationally-determined fuel velocities at fuel injector nozzle chamber entry at engine speed of 2600 rpm and engine loads of 2.5/5/7.5/10 Nm (B100 soybean biodiesel fuel)

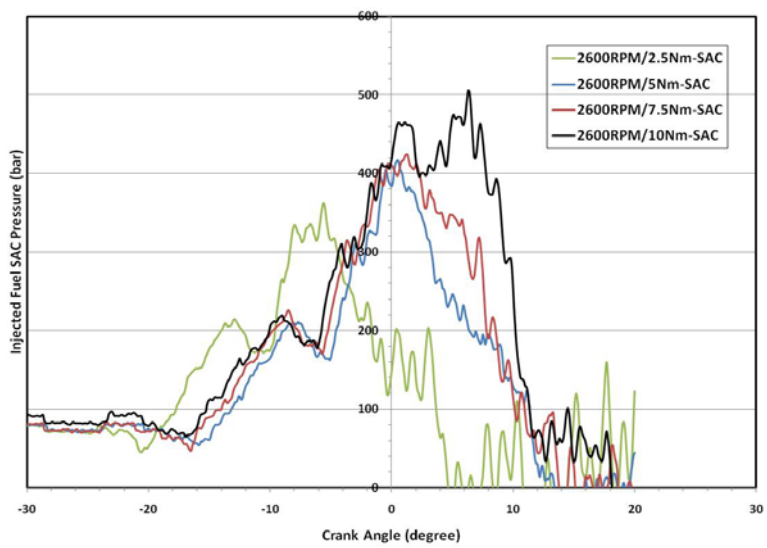

Figure TTT. Computationally-determined fuel injector sac pressure profiles at engine speed of 2600 rpm and engine loads of 2.5/5/7.5/10 Nm (B100 soybean biodiesel fuel)

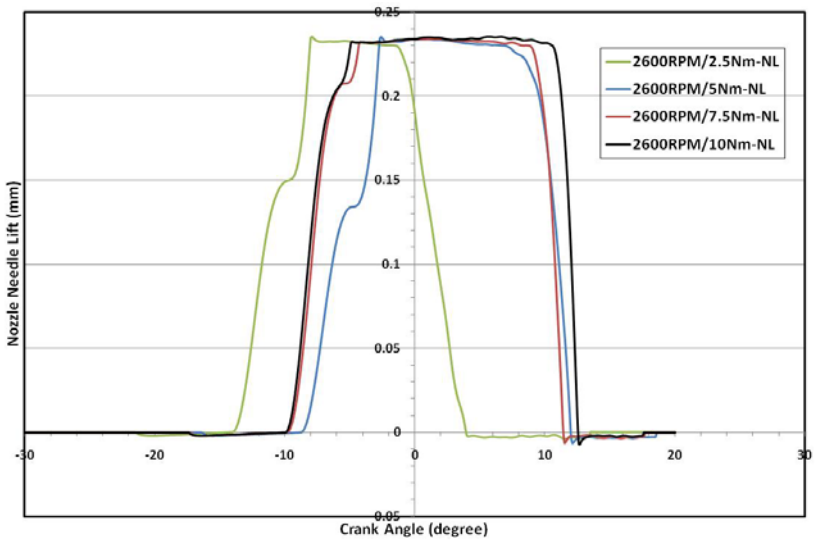

Figure UUU. Measured fuel injector nozzle needle lift profiles at engine speed of 2600 rpm and engine loads of 2.5/5/7.5/10 Nm (B100 soybean biodiesel fuel)

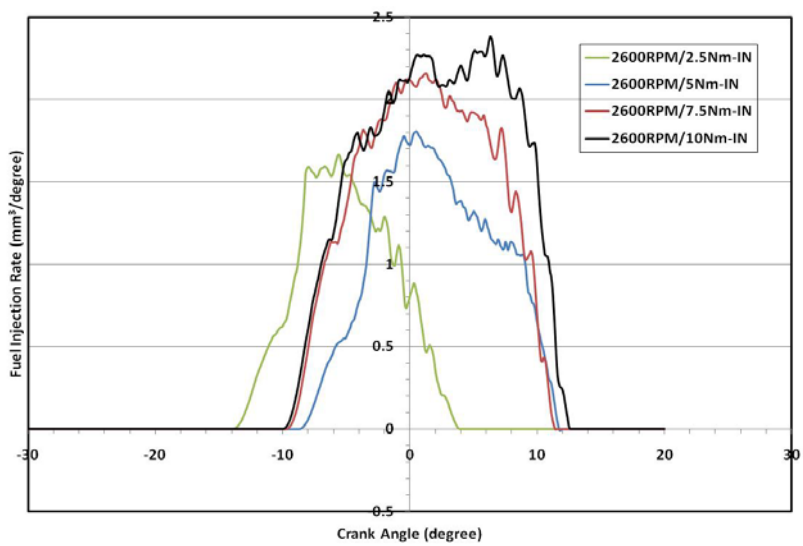

Figure VVV. Measured fuel injection rate profiles at engine speed of 2600 rpm and engine loads of 2.5/5/7.5/10 Nm (B100 soybean biodiesel fuel)

Figures WWW - ZZZ: In-Cylinder Pressure Comparison Plots (No. 2 Diesel 2200RPM)

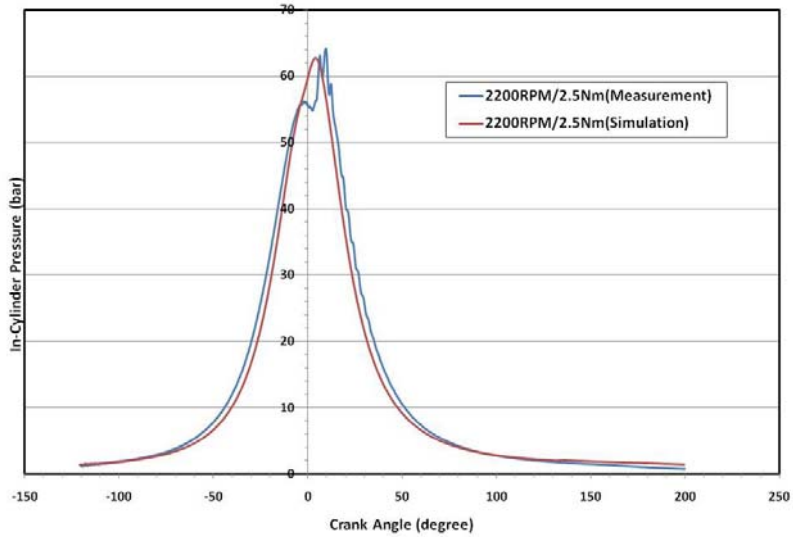

Figure WWW. Predicted and measured in-cylinder pressure profiles at engine speed of 2200 rpm and engine load of 2.5 Nm (No. 2 diesel fuel)

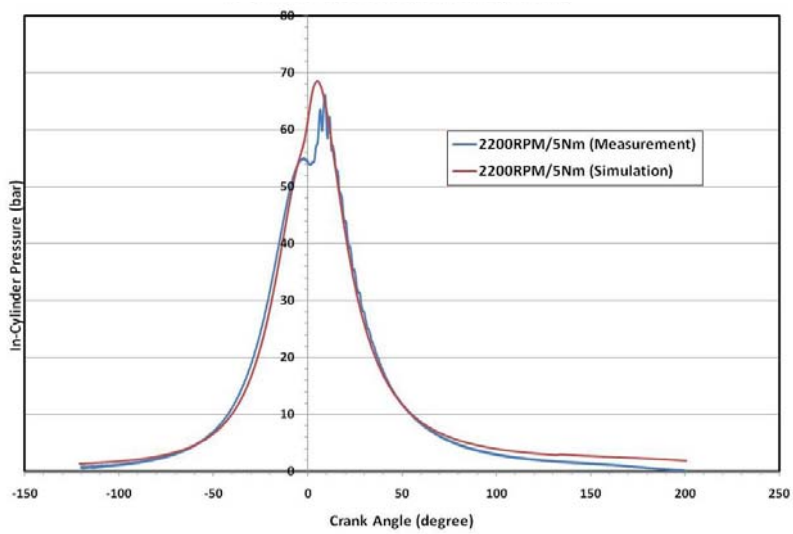

Figure XXX. Predicted and measured in-cylinder pressure profiles at engine speed of 2200 rpm and engine load of 5 Nm (No. 2 diesel fuel)

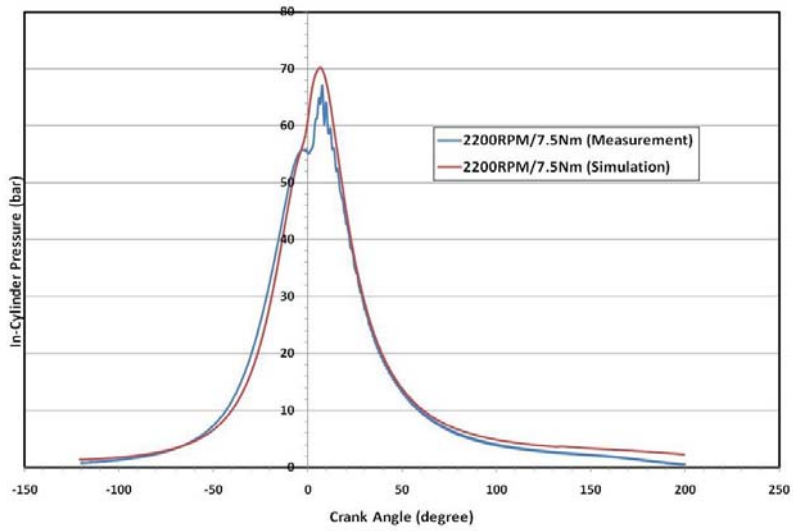

Figure YYY. Predicted and measured in-cylinder pressure profiles at engine speed of 2200 rpm and engine load of 7.5 Nm (No. 2 diesel fuel)

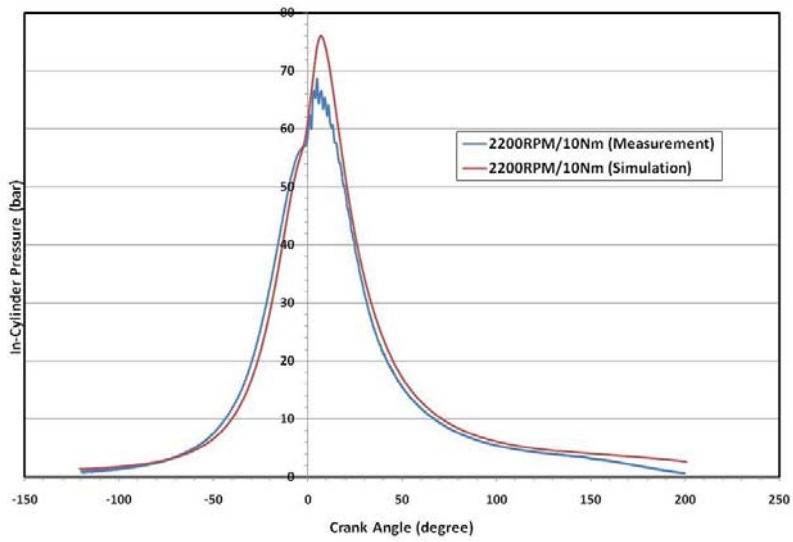

Figure ZZZ. Predicted and measured in-cylinder pressure profiles at engine speed of 2200 rpm and engine load of 10 Nm (No. 2 diesel fuel)

Figures AAAA - DDDD: In-Cylinder Pressure Comparison Plots (No. 2 Diesel 2600RPM)

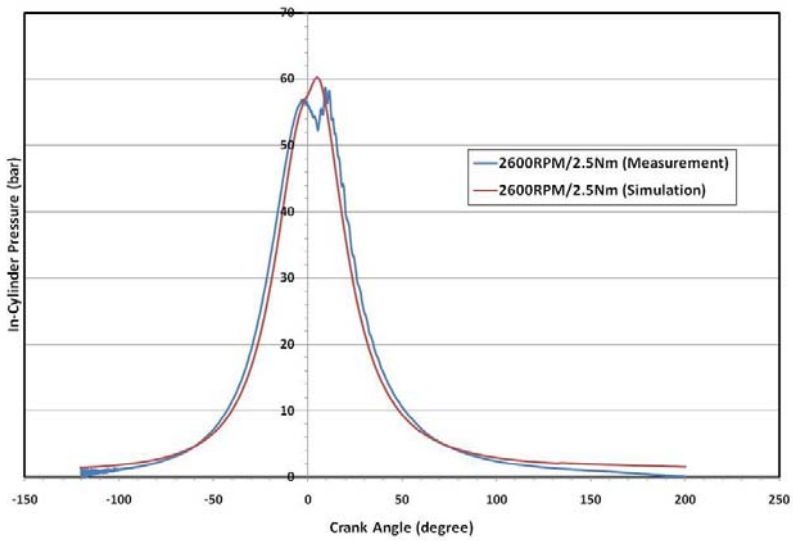

Figure AAAA. Predicted and measured in-cylinder pressure profiles at engine speed of 2600 rpm and engine load of 2.5 Nm (No. 2 diesel fuel)

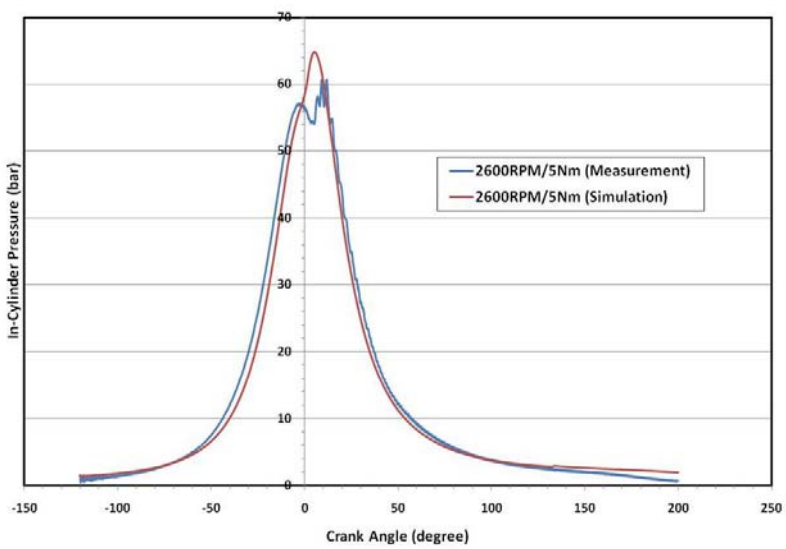

Figure BBBB. Predicted and measured in-cylinder pressure profiles at engine speed of 2600 rpm and engine load of 5 Nm (No. 2 diesel fuel)

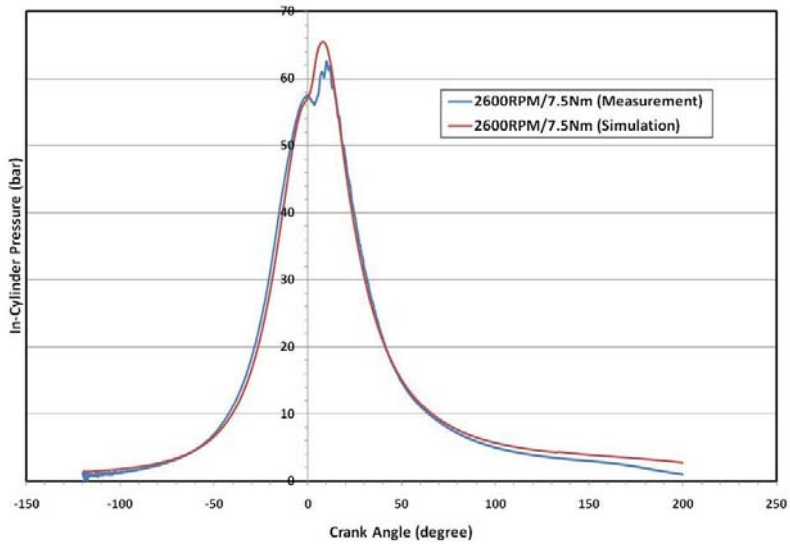

Figure CCCC. Predicted and measured in-cylinder pressure profiles at engine speed of 2600 rpm and engine load of 7.5 Nm (No. 2 diesel fuel)

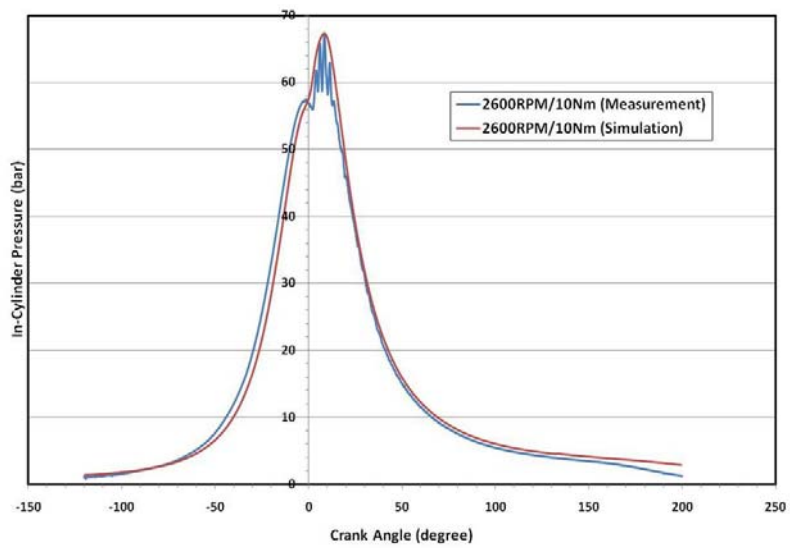

Figure DDDD. Predicted and measured in-cylinder pressure profiles at engine speed of 2600 rpm and engine load of 10 Nm (No. 2 diesel fuel)

Figures EEEE - JJJJ: GT-Power Predicted Values (No.2 Diesel, 2200 & 2600 RPM)

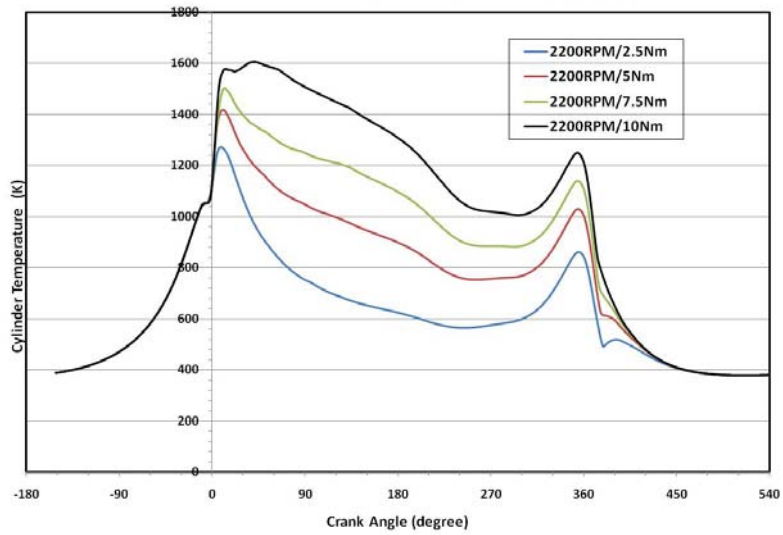

Figure EEEE. Simulation-predicted cylinder temperature at engine speed of 2200 rpm and engine loads of 2.5/5/7.5/10 Nm (No. 2 diesel fuel)

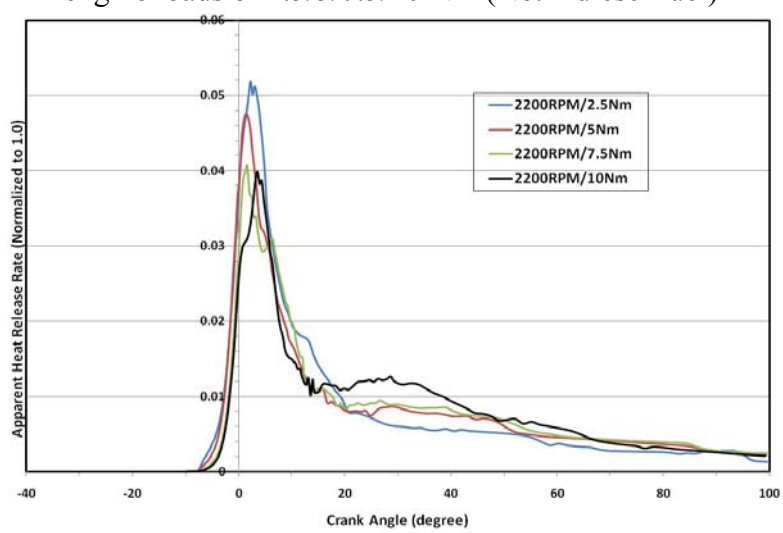

Figure FFFF. Simulation-predicted apparent heat release rate at engine speed of 2200 rpm and engine loads of 2.5/5/7.5/10 Nm (No. 2 diesel fuel)

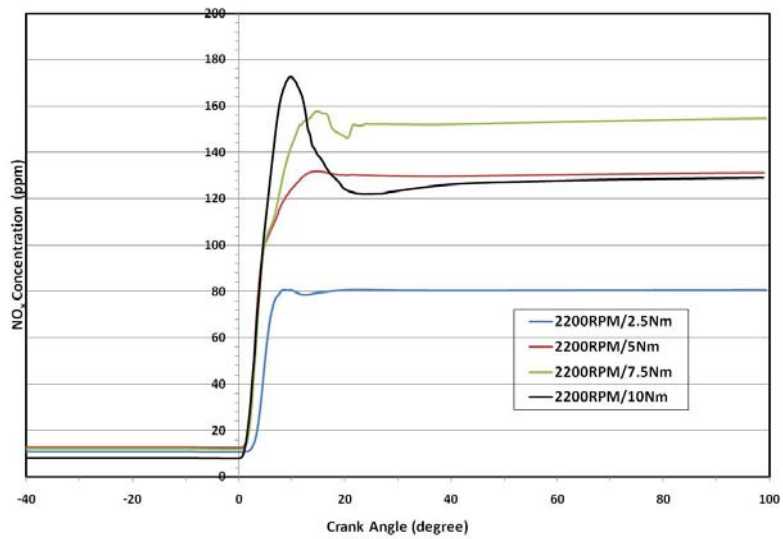

Figure GGGG. Simulation-predicted NO_x concentration at engine speed of 2200 rpm and engine loads of 2.5/5/7.5/10 Nm (No. 2 diesel fuel)

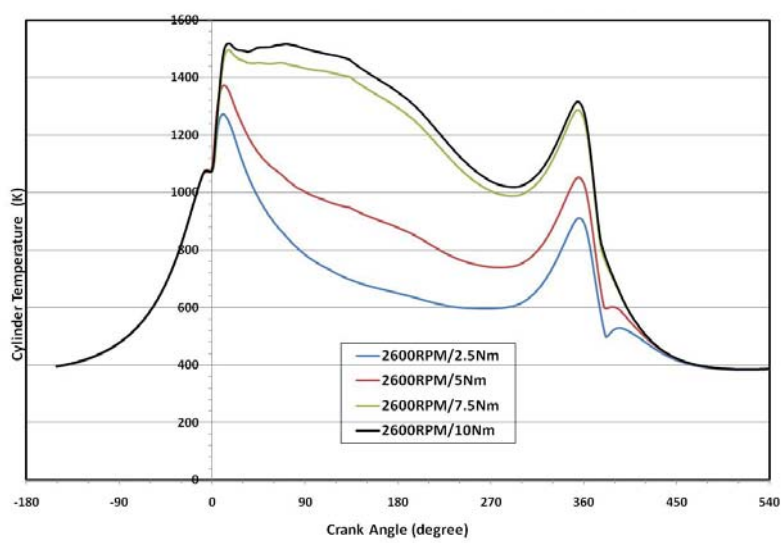

Figure HHHH. Simulation-predicted cylinder temperature at engine speed of 2600 rpm and engine loads of 2.5/5/7.5/10 Nm (No. 2 diesel fuel)

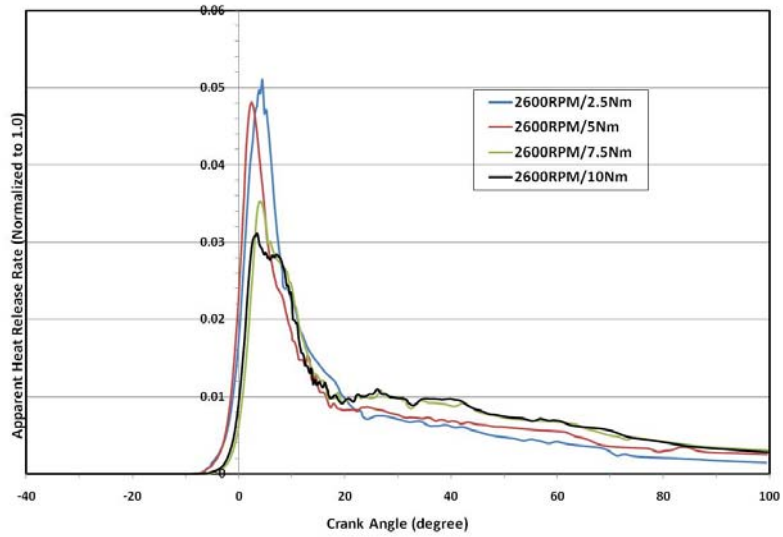

Figure IIII. Simulation-predicted apparent heat release rate at engine speed of 2600 rpm and engine loads of 2.5/5/7.5/10 Nm (No. 2 diesel fuel)

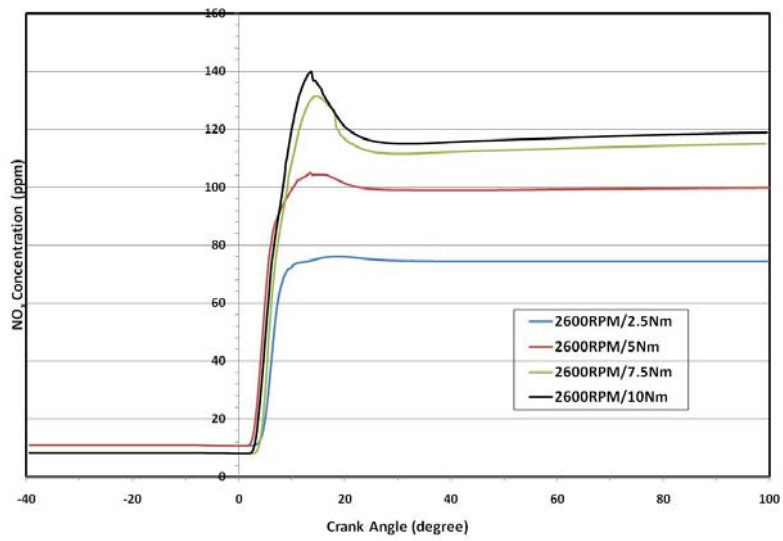

Figure JJJJ. Simulation-predicted NO_x concentration at engine speed of 2600 rpm and engine loads of 2.5/5/7.5/10 Nm (No. 2 diesel fuel)

Figures KKKK - RRRR: In-Cylinder Pressure Comparison Plots (Soy Biodiesel)

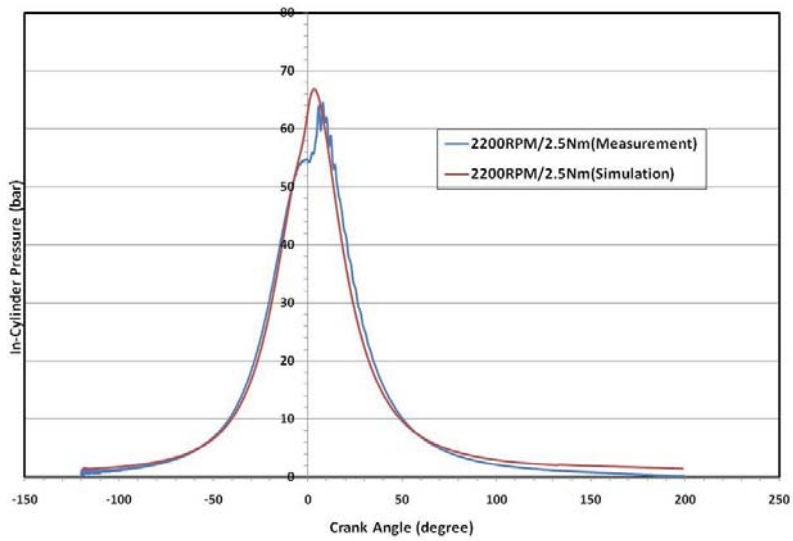

Figure KKKK. Predicted and measured in-cylinder pressure profiles at engine speed of 2200 rpm and engine load of 2.5 Nm (B100 soybean biodiesel fuel)

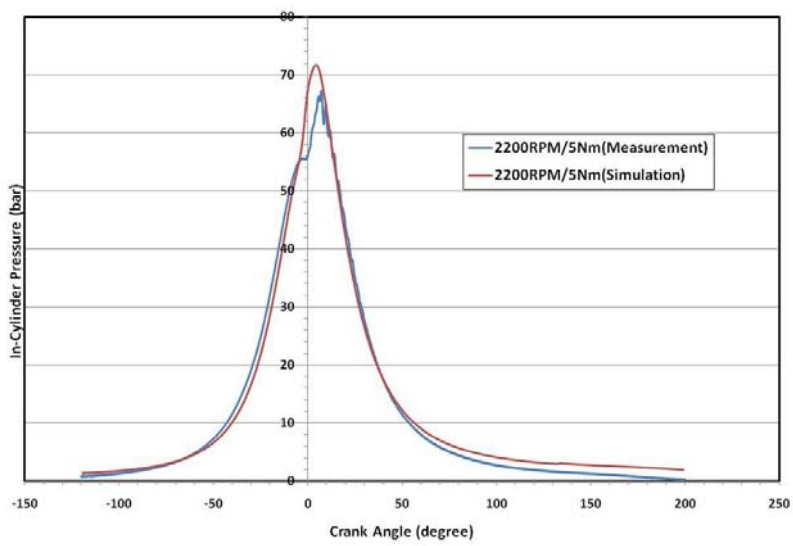

Figure LLLL. Predicted and measured in-cylinder pressure profiles at engine speed of 2200 rpm and engine load of 5 Nm (B100 soybean biodiesel fuel)

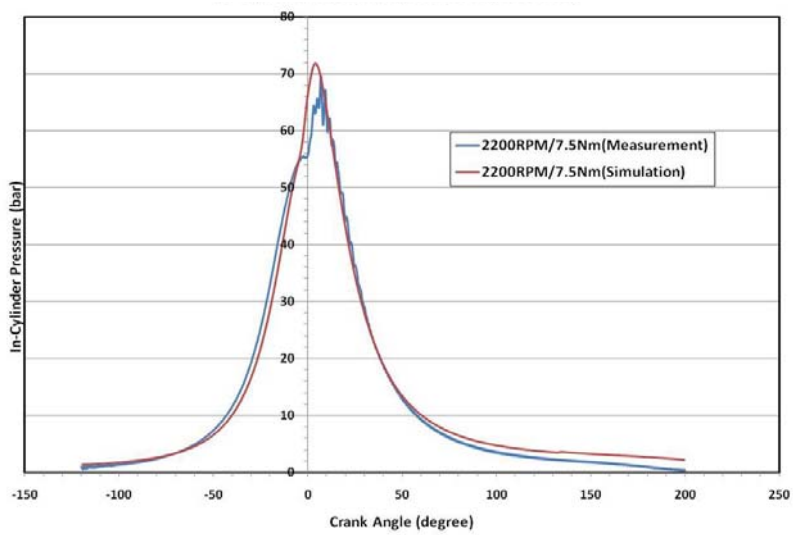

Figure MMMM. Predicted and measured in-cylinder pressure profiles at engine speed of 2200 rpm and engine load of 7.5 Nm (B100 soybean biodiesel fuel)

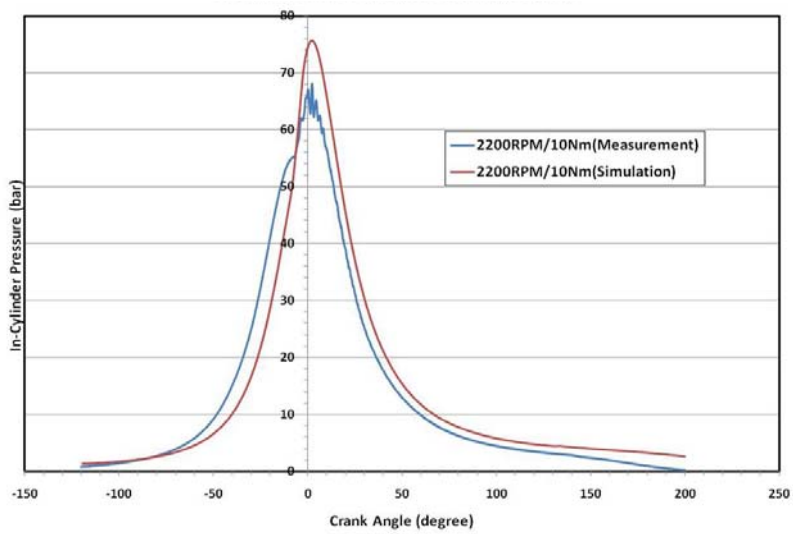

Figure NNNN. Predicted and measured in-cylinder pressure profiles at engine speed of 2200 rpm and engine load of 10 Nm (B100 soybean biodiesel fuel)

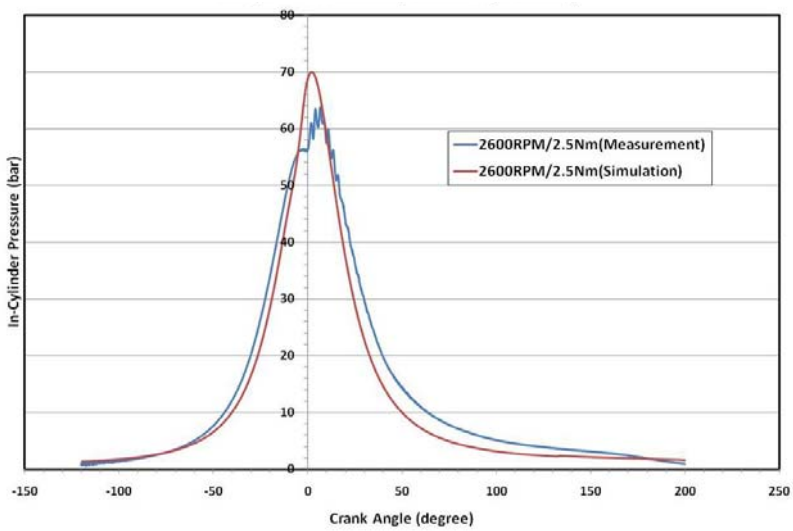

Figure OOOO. Predicted and measured in-cylinder pressure profiles at engine speed of 2600 rpm and engine load of 2.5 Nm (B100 soybean biodiesel fuel)

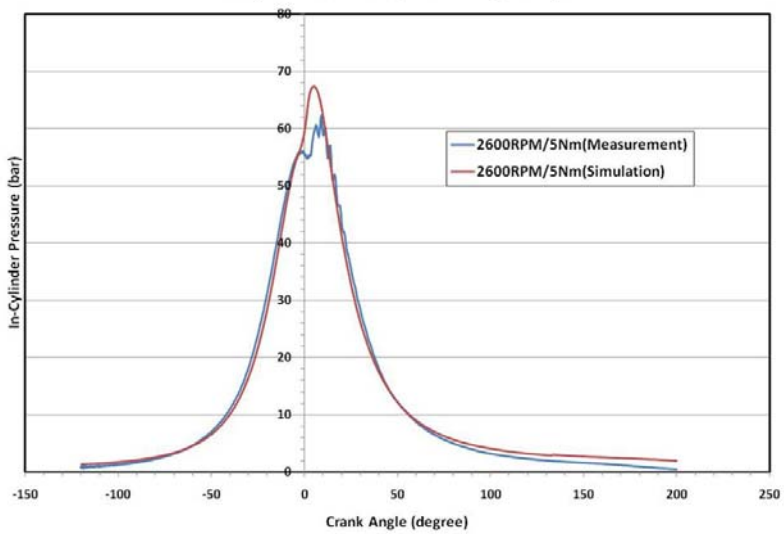

Figure PPPP. Predicted and measured in-cylinder pressure profiles at engine speed of 2600 rpm and engine load of 5 Nm (B100 soybean biodiesel fuel)

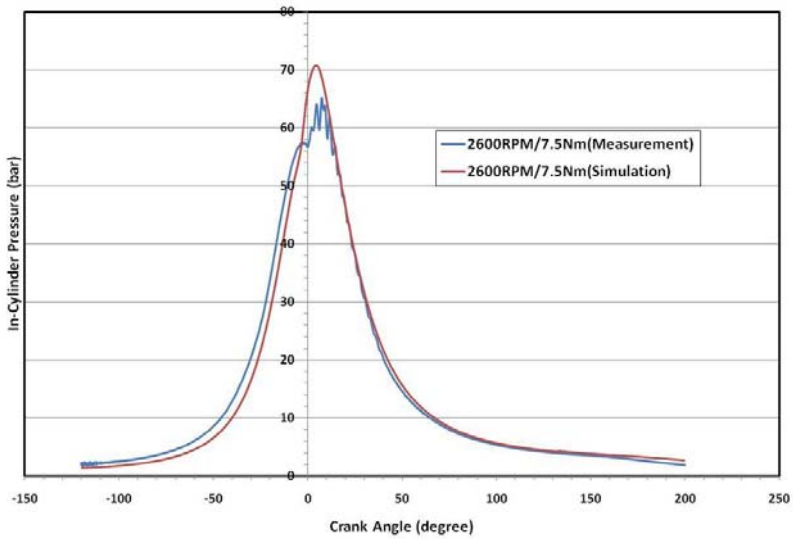

Figure QQQQ. Predicted and measured in-cylinder pressure profiles at engine speed of 2600 rpm and engine load of 7.5 Nm (B100 soybean biodiesel fuel)

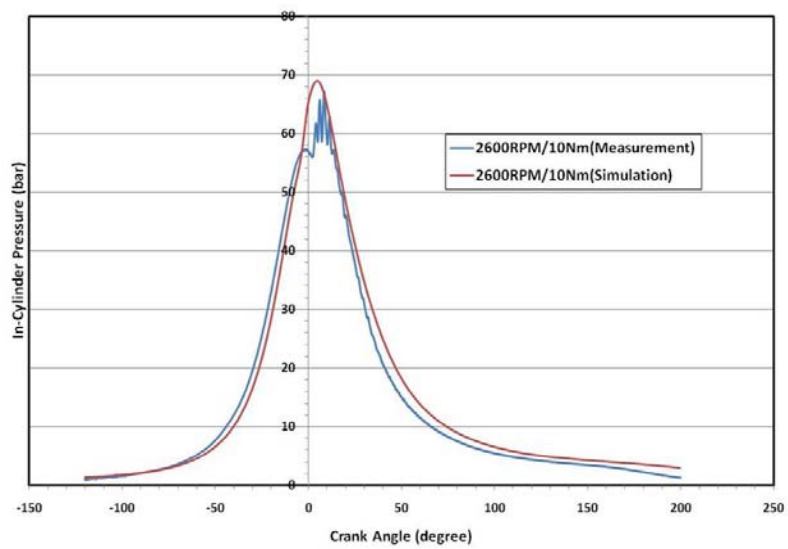

Figure RRRR. Predicted and measured in-cylinder pressure profiles at engine speed of 2600 rpm and engine load of 10 Nm (B100 soybean biodiesel fuel)

Figures SSSS - XXXX: GT-Power Predicted Values (Soy Biodiesel, 2200 & 2600 RPM)

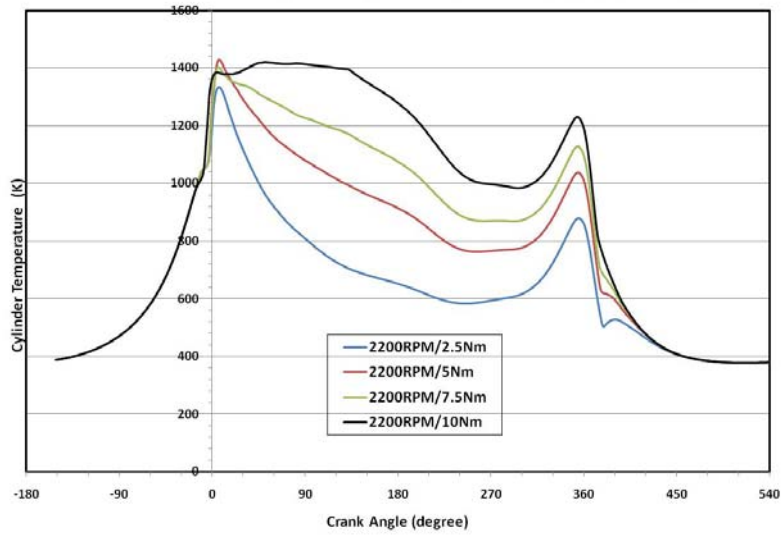

Figure SSSS. Simulation-predicted cylinder temperature at engine speed of 2200 rpm and engine loads of 2.5/5/7.5/10 Nm (B100 soybean biodiesel fuel)

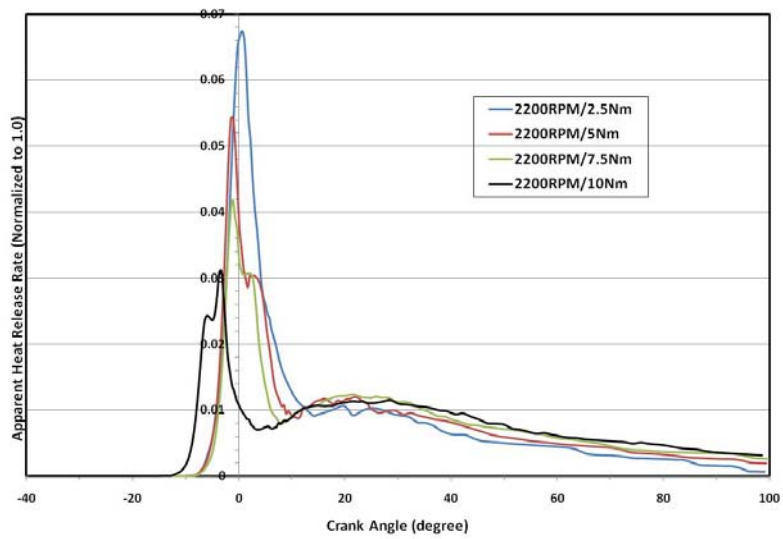

Figure TTTT. Simulation-predicted apparent heat release rate at engine speed of 2200 rpm and engine loads of 2.5/5/7.5/10 Nm (B100 soybean biodiesel fuel)

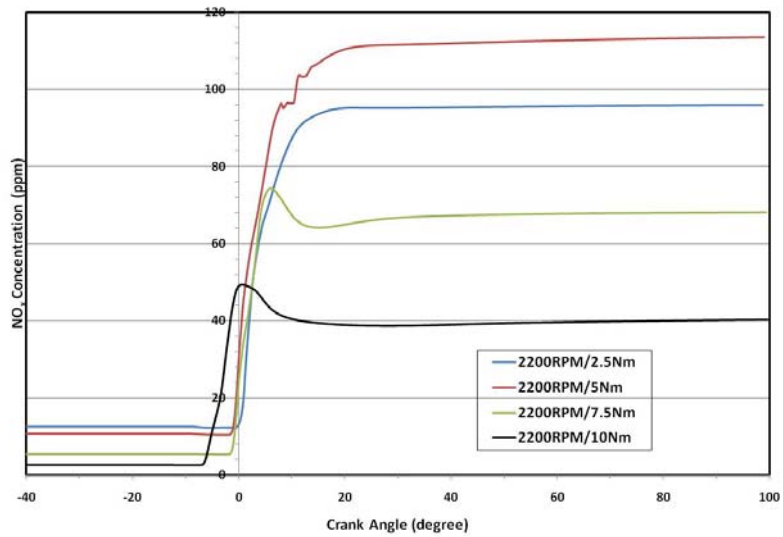

Figure UUUU. Simulation-predicted NO_x concentration at engine speed of 2200 rpm and engine loads of 2.5/5/7.5/10 Nm (B100 soybean biodiesel fuel)

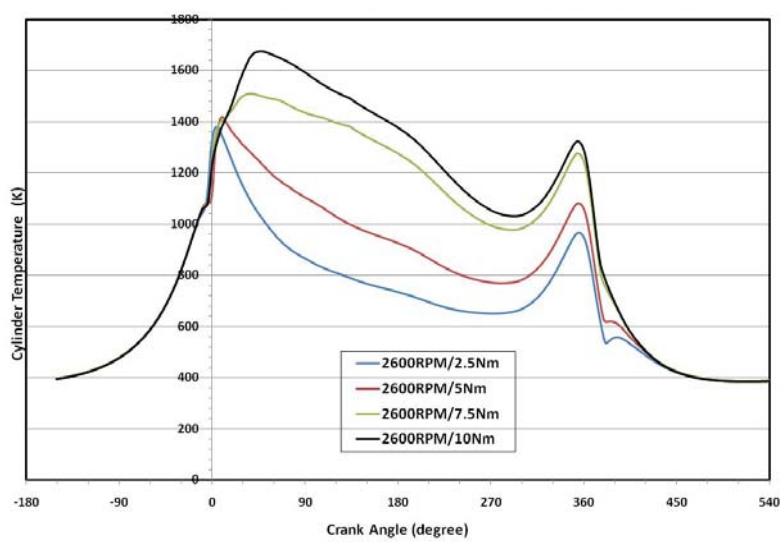

Figure VVVV. Simulation-predicted cylinder temperature at engine speed of 2600 rpm and engine loads of 2.5/5/7.5/10 Nm (B100 soybean biodiesel fuel)

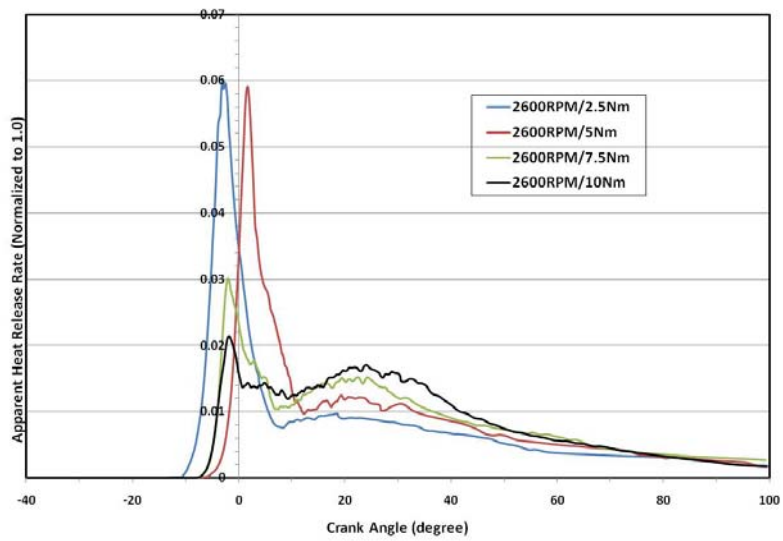

Figure WWWW. Simulation-predicted apparent heat release rate at engine speed of 2600 rpm and engine loads of 2.5/5/7.5/10 Nm (B100 soybean biodiesel fuel)

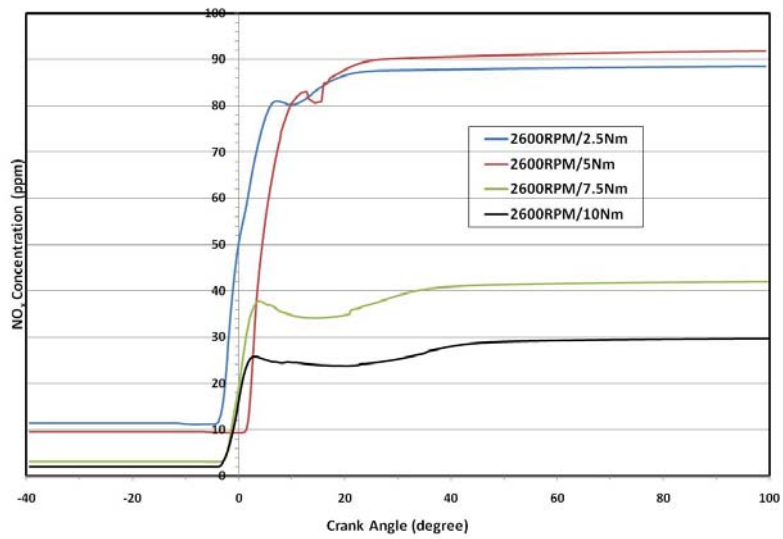

Figure XXXX. Simulation-predicted NO_x concentration at engine speed of 2600 rpm and engine loads of 2.5/5/7.5/10 Nm (B100 soybean biodiesel fuel)

Fatty Acid	Carbon Number	Carbon Atoms	Double Bonds	Soybean Methylester (Typical)*	**Soybean Methylester[30]**	Soybean Oil[31]	**Soybean Methyl-ester[31]**	Soybean Oil[32]	**Soybean Methylester[33]**	Soybean Biodiesel[34]
Myristic	C14:0	14	0			0.1	**0.2**			
Palmitic	C16:0	16	0	12	**10.81**	10.3	**10.2**	11.75	**16.3**	2.3-11
Palmitoleic	C16:1	16	1		**0.11**					
Stearic	C18:0	18	0	5	**4.54**	4.7	**4.6**	3.15	**6**	2.4-6

Oleic	C18:1	18	1	25	**24.96**	22.5	**22.2**	23.26	**24.3**	22-30.8
Linoleic	C18:2	18	2	52	**50.66**	54.1	**54.6**	55.53	**53.4**	49-53
Linolenic	C18:3	18	3	6	**7.27**	8.3	**8.2**	6.31		2-10.5
Arachidic	C20:0	20	0		**0.37**					
Gadoleic	C20:1	20	1		**0.32**					
Behenic	C22:0	22	0		**0.42**					
Lignoceric	C24:0	24	0		**0.12**					
Sum					**99.58**	100	**100**	100	**100**	

* National Biodiesel Board

Table A. Fatty acid profiles of soybean oil and soybean methylester
(by mass fraction of each component ester)

Fatty Acid	Carbon Number	Carbon Atoms	Double Bonds	Cottonseed Oil[27]	**Cottonseed Oil[31]**	**Cottonseed Oil[32]**	Cottonseed Biodiesel[34]	**Cottonseed Oil[39]**
Myristic	C14:0	14	0		**0.8**		0.8-1.5	**0.7**
Palmitic	C16:0	16	0	28	**22.9**	**28.33**	22-24	**21.79**
Palmitoleic	C16:1	16	1					**0.56**
Stearic	C18:0	18	0	1	**3.1**	**0.89**	2.6-5	**2.48**
Oleic	C18:1	18	1	13	**18.5**	**13.27**	19	**12.02**
Linoleic	C18:2	18	2	58	**54.2**	**57.51**	50-52.5	**61.62**
Linolenic	C18:3	18	3		**0.5**			
Arachidic	C20:0	20	0					**0.36**
Other								**0.47**
Sum				100	**100**	**100**		**100**

Table B. Fatty acid profiles of cottonseed oil and cottonseed biodiesel
(by mass fraction of each component ester)

Fatty Acid Identity	Mol. Wt.	Area (%)
14:0	242	**1.6**
14:1	240	**0.4**
15:0	256	**0.4**
iso-15:0	256	**1.0**
16:0	270	**15.0**
16:1	268	**3.5**
16:2	266	**2.5**
17:0	284	**3.3**
iso-17:0	284	**8.4**
17:1	282	**1.0**
18:0	298	**11.0**
18:1	296	**36.0**
18:2	294	**7.4**
19:0	312	**0.3**
iso-19:0	312	**0.5**
19:1	310	**0.1**
20:0	326	**2.1**
20:1	324	**2.5**
Sum		**97.0**

Table C. Fatty acid methyl esters of triglycerides of nitrogen starved green algal neochloris oleoabundans (**Yuan et al, 2004**)

Fatty Acid Methyl Esters	%
Methyl Miristate (14:0)	**9.8**
Methyl Palmitate (16:0)	**32**
Methyl Palmitoleate (16:1)	**3.3**
Methyl Stearate (18:0)	**1.5**
Methyl Oleate (18:1)	**14.2**
Methyl Linoleate (18:2)	**21.4**
Methyl Eicosanoate (20:0)	**0.3**
Methyl Arachidonate (20:4)	**1.6**
Methyl Eicosapentaenoate (20:5)	**2.6**
Methyl Tetracosanoate (24:0)	**0.6**
Others*	**18.3**
Sum	**105.6**

Other fatty acids identified: 15:0, 17:0, 14:1, 16:1, 16:2, 16:3, 18:3, 18:4, 20:2, 22:5

Table D. Most abundant species of macroalgae biodiesel identified by using

supercritical CO_2 (**Yuan, et al., 2005**)

Fatty Acid Methyl Esters	Molecular Formula	Relative Molecular Mass	Relative Content (%)
Methyl Tetradecanoate (14:0)	$C_{15}H_{30}O_2$	242	**1.31**
Hexadecanoic Acid Methyl Ester (16:0)	$C_{17}H_{34}O_2$	270	**12.94**
Heptadecanoic Acid Methyl Ester (17:0)	$C_{18}H_{36}O_2$	284	**0.89**
Octadecanoic Acid Methyl Ester (18:0)	$C_{19}H_{38}O_2$	298	**2.76**
9-Octadecenoic Acid Methyl Ester (18:1)	$C_{19}H_{36}O_2$	296	**60.84**
9,12-Octadecadienoic Acid Methyl Ester (18:2)	$C_{19}H_{34}O_2$	294	**17.28**
10-Nonadecenoic Acid Methyl Ester (19:1)	$C_{20}H_{38}O_2$	310	**0.36**
Eicosanoic Acid Nethyl Ester (20:0)	$C_{21}H_{42}O_2$	326	**0.35**
11-Eicosenioc Acid Methyl Ester (20:1)	$C_{21}H_{40}O_2$	324	**0.42**
Sum			**97.15**

Table E. Fatty acid methyl esters in microalga biodiesel (GT-Power, 2006)